Surface Modification Studies on Lithium-rich Layered Oxides

by

Chulgi Nathan Hong

A thesis

presented to the University of Waterloo

in fulfillment of the

thesis requirement for the degree of

Master of Science

in

Chemistry

Waterloo, Ontario, Canada, 2020

Author’s Declaration

I hereby declare that I am the sole author of this thesis. This is a true copy of the thesis, including any required final revisions, as accepted by my examiners.

I understand that my thesis may be made electronically available to the public.

Abstract

The importance of developing energy-dense lithium-ion batteries has gained much attention due to the rapid advancement in portable electronic devices to electric vehicles. In order to fulfill the energy requirement of those applications, much of the attention has gone to developing high energy density lithium-rich cathode active materials. Among various lithium-rich cathodes, lithium-rich nickel cobalt manganese layered oxide (HE-NCM) is considered to be used in lithium-ion batteries due to the high energy density from HE-NCM. Although this cathode has been developed over a decade ago, the use of HE-NCM as the next-generation battery chemistry has been a challenging task due to problems such as electrolyte oxidation and cathode structural instability at high voltage. Many researchers tried to solve these issues by surface modifications with metal oxides and fluorides since electrolyte oxidation and structural degradation begins from the cathode surface. Although surface modification strategies show promising results on mitigating side reactions between the cathode and electrolyte interface, much of the studies regarding the effects of surface modification as a mean to address lattice oxygen release have not much been investigated.

Battery researchers believe that the origin of the electrolyte oxidation is related to the interface between the cathode and liquid electrolyte, namely electron transfer from ethylene carbonate to the cathode surface at high voltage. Thus, studies regarding surface coatings including Al_2O_3, AlF_3, $LiAlO_2$, MgF_2, and others were implemented with highly insulating materials to prevent electrolyte oxidation. Although these coatings indeed show positive effects on cycling stability, cathode structural degradation still occurs. Extensive studies were continued by many researchers to find other governing factors to improve structural stability

and mitigate capacity degradation. A recent study revealed that surface degradation of HE-NCM is closely related to the lattice oxygen loss, and this loss is triggered by substantial depletion of lithium ions when charged up to 4.7 V, which then yields to underbonded oxygen in the lattice.

Herein, a Li-Mo-O coating is used to modify the HE-NCM surface to address the problem of lattice oxygen loss and electrode – electrolyte interfacial side reactions. To better distribute Mo coating, exfoliated molybdenum oxide hydroxide hydrate was used to coat on HE-NCM. The coated HE-NCM was then heat treated in air at 600 ^{o}C to induce Mo^{6+} surface diffusion and Li-Mo-O coating. The structural and chemical analysis of the coated HE-NCM was investigated using various spectroscopic tools such as XRD, XPS, Raman, SEM, EDS and TEM. After series of analysis, Li-Mo-O coated HE-NCM was washed with de-ionized water to remove the coating. Decoupling of the Li-Mo-O coating and Mo^{6+} surface diffusion effects were systematically initiated by comparing electrochemical performance tests on the pristine, water washed 3 wt% Li-Mo-O coated and 3 wt% Li-Mo-O coated HE-NCM. The coated HE-NCM shows enhanced stability for over 200 cycles when compared with non-surface modified HE-NCM. The surface modification procedure is facile and scalable, which can be potentially beneficial towards commercialization of lithium-rich layered oxides.

Acknowledgements

I would like to express my utmost appreciation to my supervisor Professor Linda F. Nazar for research guidance and support. I am thankful to my committee members, Professor Rodney Smith and Professor Vivek Maheshwari, for their comments and directions on this research and to all Nazar research group members for maintaining a warm and comfortable research environment. I would especially like to show gratitude to SeYoung Kim and Dr. KernHo Park for constructive research guidance and discussions. I would also like to thank BASF SE for the opportunity to conduct my cathode coating research by providing research funding and necessary battery materials.

Table of Contents

List of Figures

List of Tables and Equations

List of Abbreviations

AC	Alternating current
CEI	Cathode electrolyte interphase
DC	Direct current
DEC	Diethyl carbonate
DFT	Density functional theory
DMC	Dimethyl carbonate
DME	1,2-dimethoxyethane
DMSO	Dimethyl sulfoxide
dQ/dV	Differential capacity plot
EC	Ethylene carbonate
EDS	Energy dispersive X-ray spectroscopy
EIS	Electrochemical impedance spectroscopy
HE-NCM	High energy Li-rich lithium nickel cobalt manganese layered oxide
ICSD	Inorganic crystal structure database
J-T	Jahn Teller
LCO	Lithium cobalt oxide
LFP	Lithium iron phosphate
LHB	Lower hubbard band
Li^+	Lithium-ion
LIB	Lithium-ion battery
$LiPF_6$	Lithium hexafluorophosphate
LLO	Lithium-rich layered oxide
LMO	Lithium manganese oxide
LNMO	Lithium nickel manganese oxide
LNO	Lithium nickel oxide
Ni-Cd	Nickel cadmium
Ni-MH	Nickel metal hydride

NMC	Lithium nickel cobalt manganese layered oxide
OCV	Open circuit voltage
SEI	Solid electrolyte interphase
SEM	Scanning electron microscopy
SS	Stainless steel
TEM	Transmission electron microscopy
TM	Transition metal
UHB	Upper hubbard band
XPS	X-ray photoelectron spectroscopy
XPS	X-ray photoelectron spectroscopy
XRD	X-ray diffraction

Chapter 1. Introduction

1.1 Overview of Secondary Lithium-ion Batteries

The world's energy demand is continuously rising due to the rapid advances in technology, population increase, and power-hungry electronic devices.[1,2] Since energy storage and energy generation are equally important, high-performance energy storage devices are crucial for modern society. Previous battery chemistries, such as nickel-metal hydride (Ni-MH) and nickel-cadmium (Ni-Cd), were not sufficiently storing energy to meet the demands of our society (Figure 1.1).[1] Nowadays, secondary lithium-ion batteries (LIB) are the primary power sources in devices such as portable electronics and medical implants, and their applications are extended to rechargeable electric vehicles and grid-level energy storage.[3] Compared to predecessor technologies, substantially improved energy/power densities, rate performance, cycle-life, and no memory effect of Li-ion batteries allowed people to rely more on energy storage devices for a variety of applications.[4]

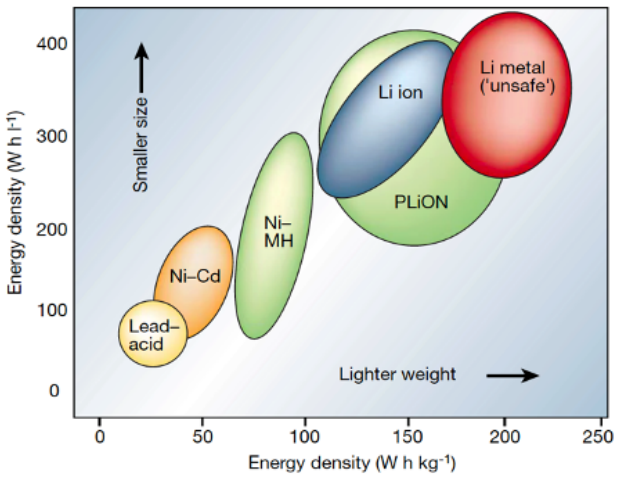

Figure 1.1 Gravimetric versus Volumetric Energy Density for Various Battery Chemistries.

Reproduced with permission from Ref. 1. Copyright 2001 from Springer Nature.

LIB is mainly composed of four different components: positive electrodes, negative electrodes, electrolyte, and separator (Figure 1.2).[5] Typically, lithium transition metal oxide is used for the positive electrode, and graphite is used for the negative electrode.[6] In the case of electrolytes, a mixture of organic solvents and lithium salt is used. The solvated salt electrolyte operates as an ion conductor which transfers Li^+ during charging and discharging. The separator acts as an insulator between cathodes and anodes to prevent short-circuiting during electrochemical operation. The porosity of the separator should be large enough for Li^+ to transport in a facile manner during the battery cycling.[5] These four components are combined to establish commercial LIB. Various configurations of LIB can be seen in Figure 2.

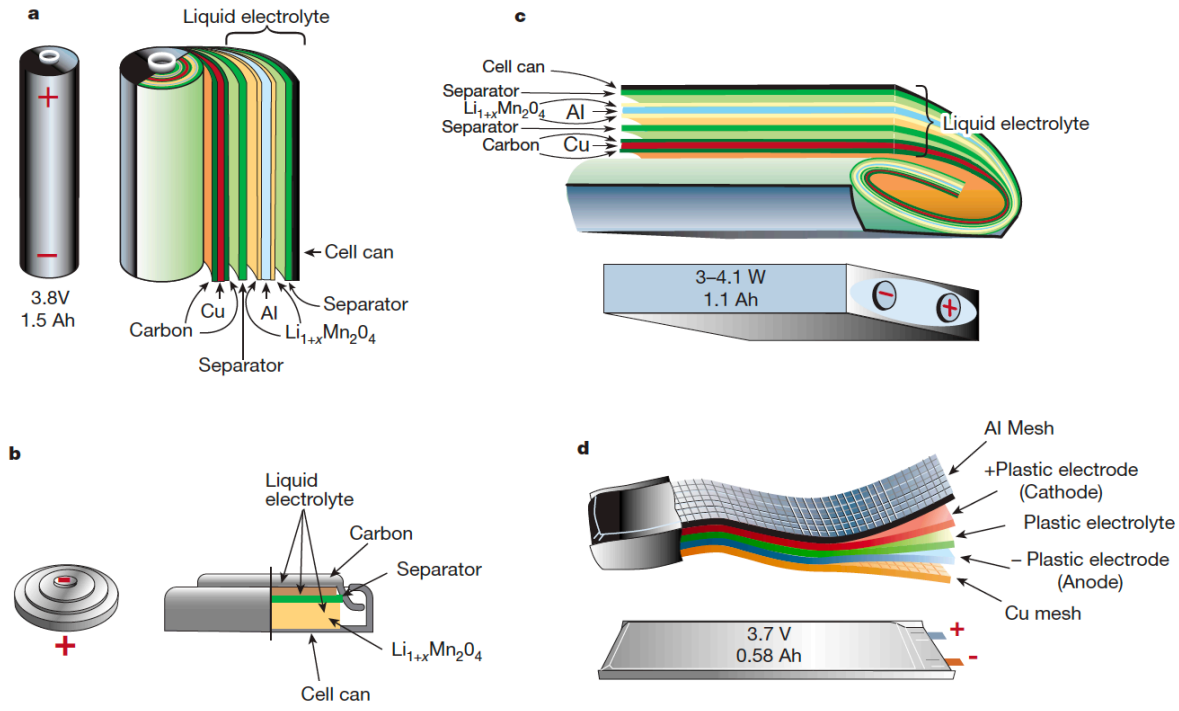

Figure 1.2 Various configurations of LIB. a) cylindrical, b) coin, c) prismatic and d) pouch cell.[5] Reproduced with permission from Ref. 1. Copyright 2001 from Springer Nature.

An active material from cathode and anode is mixed with conductive carbon and a

binder to make up an electrode.[6] The reason for the addition of conductive carbon is to distribute electronic conduction pathways so that the active materials can be electrochemically active. The role of the binder is to capture the active materials and conductive carbon on the current collector (Al for the cathode and Cu for the anode).[5]

During charging, transition metals in the lithium transition metal oxides are oxidized to extract (de-lithiated) lithium ions (equation 1.1).[7] The extracted lithium ions diffuse to the graphite through ion-conducting organic electrolytes and insert (lithiate) into the graphite layers (Figure 1.3).[5] Charge neutrality occurs after lithiation into the graphite electrode and creates the Li_xC_6 structure. The reaction ti1me for charge transfer to occur is fast compared to the Li^+ diffusion time from the electrolyte to the electrode. Thus, the electrochemical process of charging and discharging is diffusion-limited. The electrochemical reaction between the cathode and anode (e.g., $LiCoO_2$//Graphite) during the charging process is the following:[5]

Cathode reaction: $LiCoO_2 \rightarrow Li_{1-x}CoO_2 + xLi^+ + xe^-$

Anode reaction: $6C \rightarrow xLi^+ + xe^- + 6C\ Li_x$

Full cell reaction: $LiCoO_2 + 6C \rightarrow Li_{1-x}CoO_2 + Li_xC_6$

Equation 1.1 Cathode, anode and full cell chemical reaction.[3]

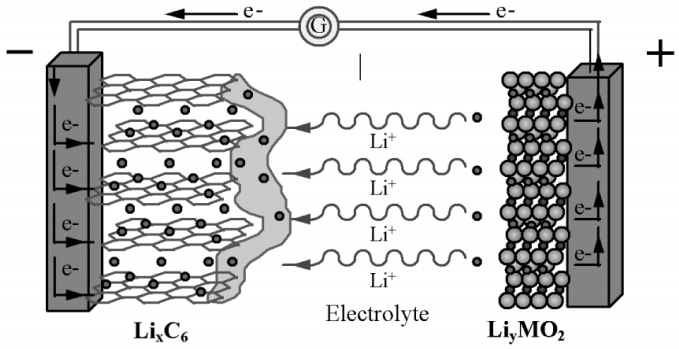

Figure 1.3 Schematic diagram of Lithium-ion battery (LIB).[3] Reproduced from Ref. 3 with permission from Royal Society of Chemistry.

There are reasons for lithium to be used as an ion source in cell chemistry. Lithium is the lightest metal in the periodic table, and this makes it an excellent ion transport medium since lighter ions will lead to facile diffusion.[1] Lithium also has the lowest standard reduction potential, which can lead to a cell's working voltage of 3 V or higher.[8] Although lithium is an excellent source for an anode material, lithium dendrite growth following battery charging and discharging eventually leads to an internal short-circuit, which is recognized as a serious safety issue.[9] For this reason, graphite is used as an anode for state-of-the-art modern lithium-ion batteries since lithium ions can intercalate within the layers of graphite, which can drastically reduce the problem of lithium dendrite growth.[10]

The cathode materials for LIB are often lithium contained metal oxides.[11] Different crystal structures categorize different kinds of metal oxide cathodes, which are layered (e.g., $LiCoO_2$), spinel (e.g., $LiMn_2O_4$), and olivine structures (e.g., $LiFePO_4$).[11] Among various cathode materials, the one that is most predominant in industry is the layered structure compound due to its reliability and high electrochemical performances.[12]

To understand the advantages of lithium layered oxides in detail, a thorough understanding of the structure of this compound is needed. Figure 1.4 shows the structure of lithium layered oxide in detail. Lithium-ion and transition metal oxide slabs are in place by stacked layers. Octahedral metal oxides are arranged in edge-sharing fashion, and each of them is lined up in a row to form a slab. The lattice oxygen surrounds lithium ions from the metal slab, and these ions also form an octahedral structure to consist of a lithium slab. Due to the Coulomb repulsion between metal slabs, lithium ions are easily able to be inserted and displaced during the charge and discharge process.[5]

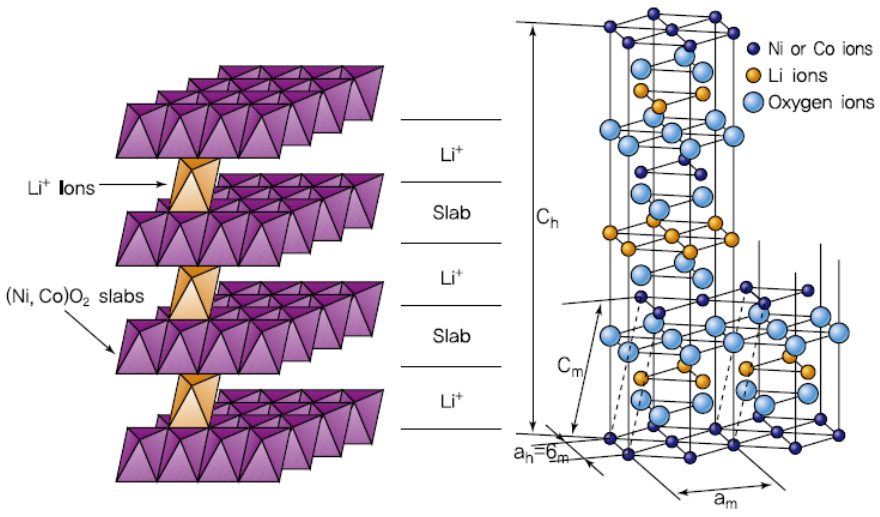

Figure 1.4 Lithium layered oxide structure in detail.[5] Reproduced with permission from Ref. 5 Copyright 2012 from John Wiley & Sons.

There are many advantages of utilizing $LiCoO_2$ (LCO) as a cathode material in LIB.[7] However, the cost of cobalt metal is expensive, and the degree of delithiation is limited due to the potentially irreversible phase transformation.[13] Phase transitions occur during the charging and discharging process. Depending on the degree of (de)lithiation, the transition can be reversible or irreversible. For instance, $LiCoO_2$ experiences phase transition from an O3 (an octahedral site occupied by lithium repeating three times) to P3 (a prismatic site occupied by lithium repeating three times) to O1 (an octahedral site occupied by lithium repeating one time) structure when lithium-ion contents become less than 0.5 (Figure 1.5).[5] The phase transition from P3 to O1 may be irreversible since a new structure of CoO_2 forms at O1 (Figure 1.6), which results in a practical capacity of the $LiCoO_2$ being approximately 150 mAh g^{-1} (equation 1.2) in contrast with the theoretical capacity of 274 mAh g^{-1} (Figure 1.7).[5]

$$\text{Capacity } \left[\frac{mAh}{g}\right] = \frac{n_e \times F \left[\frac{Ah}{mol}\right] \times 1000}{Molar\ mass\ of\ AM \left[\frac{g}{mol}\right]}$$

n_e = number of electron transferred

F = Faraday constant (26.8 Ah/mol)

mAh = miliampere flowing in one hour

A = one coulomb per second

Coulomb = 1.602 e+19 electrons

Equation 1.2 Theoretical capacity calculation equation [5]

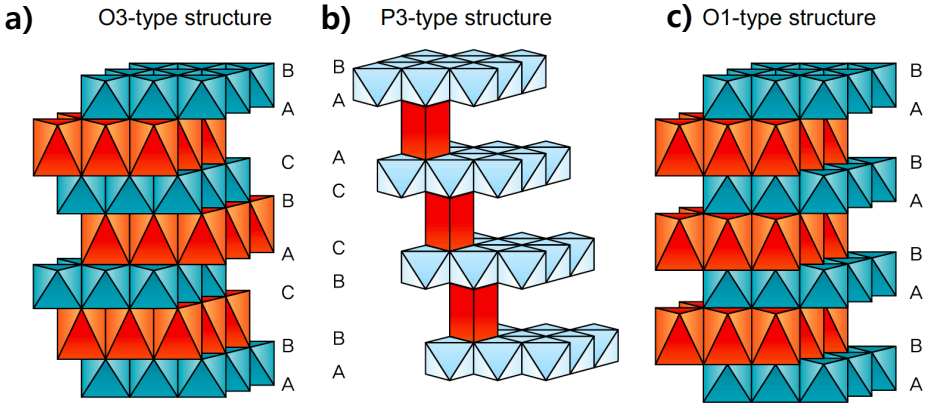

Figure 1.5 a O1, **b** P3 and **c** O1-type structure of cathode materials.[5] Reproduced with permission from Ref. 5 Copyright 2012 from John Wiley & Sons.

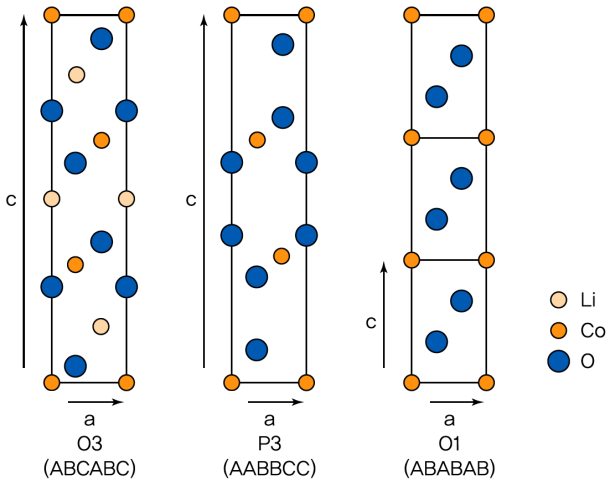

Figure 1.6 Phase transition process of $LiCoO_2$ during electrochemical operation.[5]

Reproduced with permission from Ref. 5 Copyright 2012 from John Wiley & Sons.

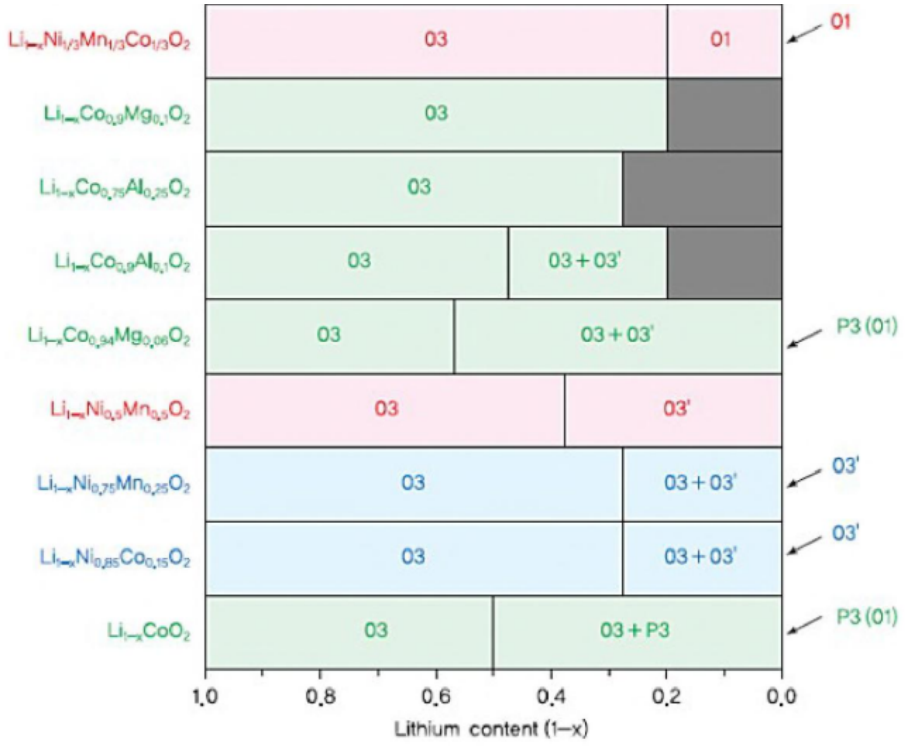

Figure 1.7 Phase transition of various layered oxide cathodes during cycling.[5]

Reproduced with permission from Ref. 5 Copyright 2012 from John Wiley & Sons.

Therefore, a better cathode was needed to increase the delithiation degree while achieving reasonable cost, electronic conductivity, and charge/discharge cycle stability.

An alternative cathode material was developed using Ni as the transition metal source (Figure 1.8). $LiNiO_2$ (LNO) exhibited a higher discharge capacity compared to LCO (20% lower than LNO).[14] Despite the advantage of high capacity, LNO has many problems. First, synthesizing stoichiometric LNO is challenging to achieve since LNO can easily become nonstoichiometric ($Li_{1-x}Ni_{1+x}O_2$).[15] The reason for this is related to the instability of Ni^{3+} and its subsequent cation disorder.[16] During the synthesis process of LNO, the low-spin of Ni^{3+}

makes it easier to form Ni^{2+} since the unpaired spin from Ni^{3+} leads to instability. The formed Ni^{2+} then easily replaces lithium-ion octahedral and Ni^{3+} octahedral sites to maintain charge neutrality (cation disorder).[16] Lastly, the structural instability at high voltage leads to lattice oxygen release, and this reacts with ethylene carbonate in the electrolyte to produce gases such as CO_2 and CO,.[17]

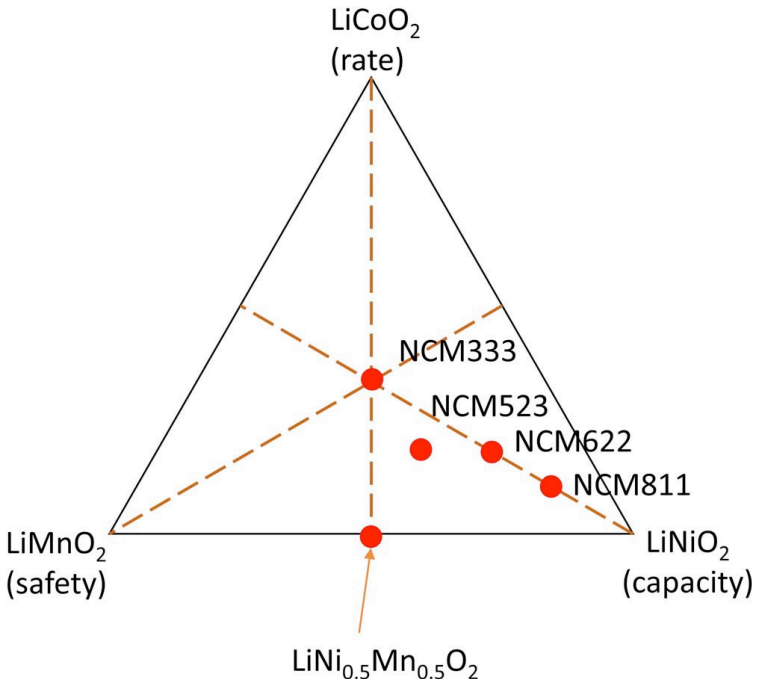

Figure. 1.8 Phase diagram of NCM with various transition metal ratio.[5] Reproduced with permission from Ref. 5 Copyright 2012 from John Wiley & Sons.

To resolve issues related to LCO and LNO, Mn is used along with Co and Ni to synthesize a class of cathode that uses three different transition metals.[12] These three components share an equal portion of contents, which result in having the formula $Li(Ni_{1/3}Co_{1/3}Mn_{1/3})O_2$ (also known as NCM or NCM111 in short).[12] The benefit of using Co^{3+} in NCM is related to its high rate performance. Mn^{4+} is used to increase structural stability since Mn^{4+} is electrochemically inactive due to its inability to oxidize further. The role of Ni^{2+}

is related to the capacity of the cathode.[18] The main contribution of the NCM capacity is from the Ni. Co becomes electrochemically active at a high voltage around 4.4 V.[19] This can be clearly seen from the energy versus density of state diagram for NCM111 (Figure 1.9).

Figure 1.9 shows the DOS diagram for NCM, which clearly shows the process of two-electron transfer via Ni^{2+}/Ni^{3+} and Ni^{3+}/Ni^{4+} until lithium contents of 0.5 are reached.[20] Delithiation can continue up to 80 %, based on the data from Figure 1.9. However, delithiation is limited to approximately 70 % (~ 4.3 V) due to structural integrity as well as possible oxygen evolution at high voltage. Since the degree of delithiation threshold is much higher than LCO as well as being cheaper due to reduced usage of Co for transition metal component, NCM is widely used for electric vehicle battery application.[12, 20, 21]

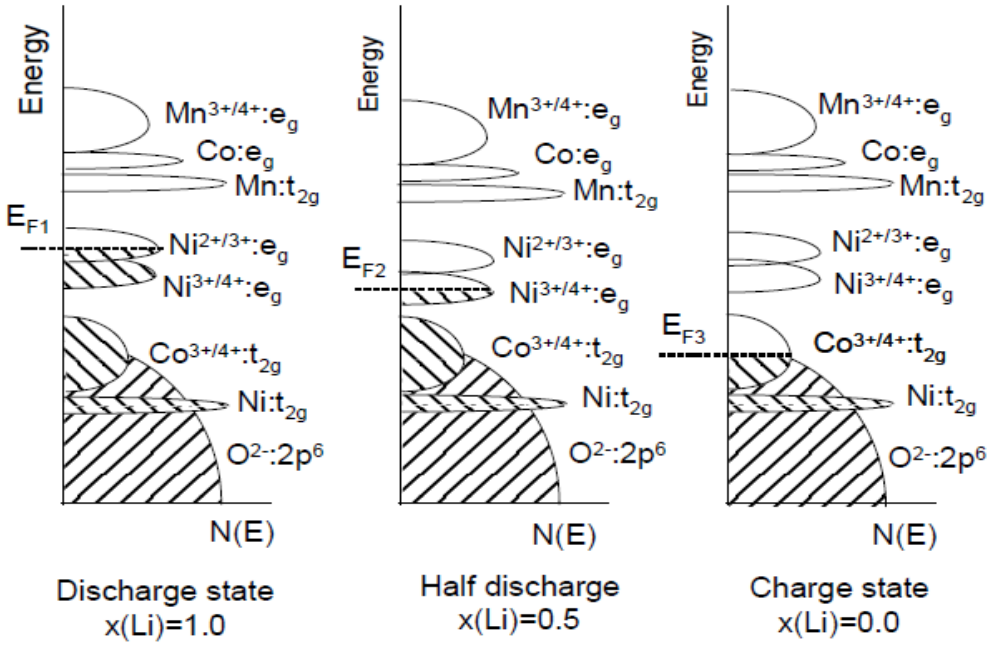

Figure 1.9 Energy versus density of state (DOS) diagram for NCM111.[20] Reproduced with permission from Ref. 20. Copyright 2017 from MDPI.

The synthesis of NCM uses the co-precipitation method (Figure 1.10).[22] Metal

precursors such as nickel, manganese, and cobalt sulfate primary particles are mixed with precipitating agents in a nitrogen atmosphere to synthesize metal composite hydroxide secondary particles consisting of Ni, Co, and Mn.[12, 22] These metal hydroxide secondary particles are again mixed with LiOH (lithium precursor) and calcined at high temperature in an air atmosphere to retrieve the final product of NCM cathode secondary particles with grain boundaries created from the aggregation of primary particles (Figure 1.10).[22]

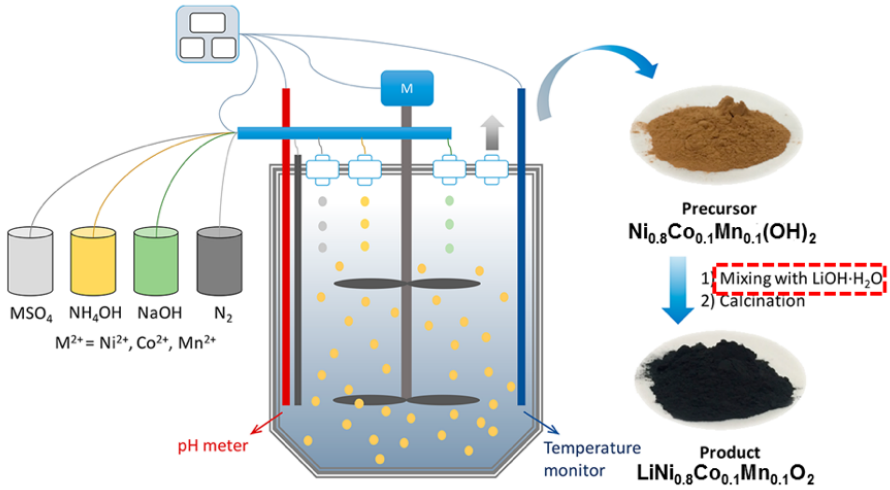

Figure 1.10 Synthesis procedure of NCM cathodes.[22] Reproduced with permission from Ref. 22. Copyright 2017 American Chemical Society.

Control of pH during the co-precipitation is essential as the value of pH determines the size and morphology of the material.[22] Also, the feeding rate of the precursor, the temperature, and stirring rate determines the overall shape of NCM.[22] Thus, these parameters should be carefully monitored to synthesize NCM with the desired shape and size.

Although NCM111 is superior to LCO for its high capacity and enhanced stability, its capacity is still not enough to satisfy the needs of high capacity batteries for applications such as long-range electric vehicles and grid-level energy storage systems.[23] Therefore, an extensive

amount of research had been performed to stretch the capacity of NCM111. So far, there are two strategies to increase the capacity of NCM111. First, one can increase the Ni content within the ternary metal ratio.[4] Since the Ni is the main capacity contributor within the working voltage of approximately 4.3 V it may increase the capacity only by increasing Ni contents. For example, $Li(Ni_{0.8}Co_{0.1}Mn_{0.1})O_2$ (also known NCM811 in short), can increase the practical capacity up to nearly 200 mAh g^{-1}.[13]

$$Ni^{3+} + O^{2-}_{(lattice)} \rightarrow Ni^{2+} + O^{-}$$

$$O^{-} + O^{-} \rightarrow O^{2-}_{(active)} + O$$

$$O^{-} + O \rightarrow O_2^{-}, \quad \text{or} \quad O + O \rightarrow O_2\uparrow$$

$$O^{2-}_{(active)} + CO_2/H_2O \rightarrow CO_3^{2-}/2\,OH^{-}$$

$$2\,Li^{+} + CO_3^{2-}/2\,OH^{-} \rightarrow Li_2CO_3/2LiOH$$

Equation 1.3 Proposed formation mechanism of Li_2CO_3 in Ni-rich cathodes[16]

However, there are drawbacks to Ni content increases. The first drawback is related to its extreme surface sensitivity in an air atmosphere (Equation 1.3).[13,16] Ni^{3+} in NCM811 undergoes spontaneous reduction to Ni^{2+} followed by oxidation of lattice oxygen.[16] This process weakens the bond between Ni and O and eventually releases O from the lattice. The released O^{2-} from the lattice then may react with CO_2 and H_2O in the atmosphere (if the Ni-rich cathode material is in the air atmosphere) to create Li_2CO_3 and LiOH on the surface of

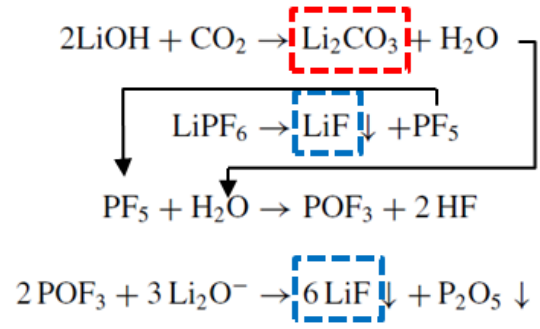

Figure 1.11. Proposed formation mechanism of HF from LiOH [14]

NCM811. These carbonates and hydroxides are detrimental towards LIB performance when the surface contaminated cathode is used to make the cells (Figure 1.11).[14] Hydroxide is especially deleterious since LiOH can react with CO_2 from ethylene carbonate (typical solvent for LIB electrolyte) oxidation during electrochemical operation and this reaction yields Li_2CO_3 and H_2O.[4,14] Water then reacts with PF_5 from $LiPF_6$ (typical lithium salt used in LIB electrolyte).[14] $LiPF_6$ is chemically unstable, and this is the reason why the reacted product of PF_5 can react with water to yield deleterious HF.[24,25] The HF can attack cathode materials to cause transition metal dissolution, and this may lead to a decrease in cathode capacity.[26] The eluted transition metal can then deposit on the surface of the anode, and this may further create problemsm, such as additional solid electrolyte interphase (SEI) growth catalyzed by the deposited metal on the anode causing impedance growth.[26] However, this proposed reaction step caused by LiOH is somewhat controversial since there are other literature reporting beneficial effects from LiOH and Li_2CO_3 coating on the cathode.[14,27-29] Thus, it is inconclusive that LiOH can be detrimental to the performance of LIB. Nevertheless, whether LiOH and Li_2CO_3 can be beneficial or not, a large amount of those carbonates and hydroxides on the cathode surface can cause an impedance increase and blockage of ion conduction pathways. Thus, it is beneficial not to have large amounts of LiOH and Li_2CO_3.[29, 30]

The second drawback of Ni-rich NCM is closely related to the anisotropic volume change of the Ni-rich NCM particle (Figure 1.12). A severe decrease in the interlayer lattice parameter c-axis above 4.1 V is causing this volume change.[31] This c-axis parameter shrinkage then causes the particle disintegration and leaves cracks within the particles.[31]

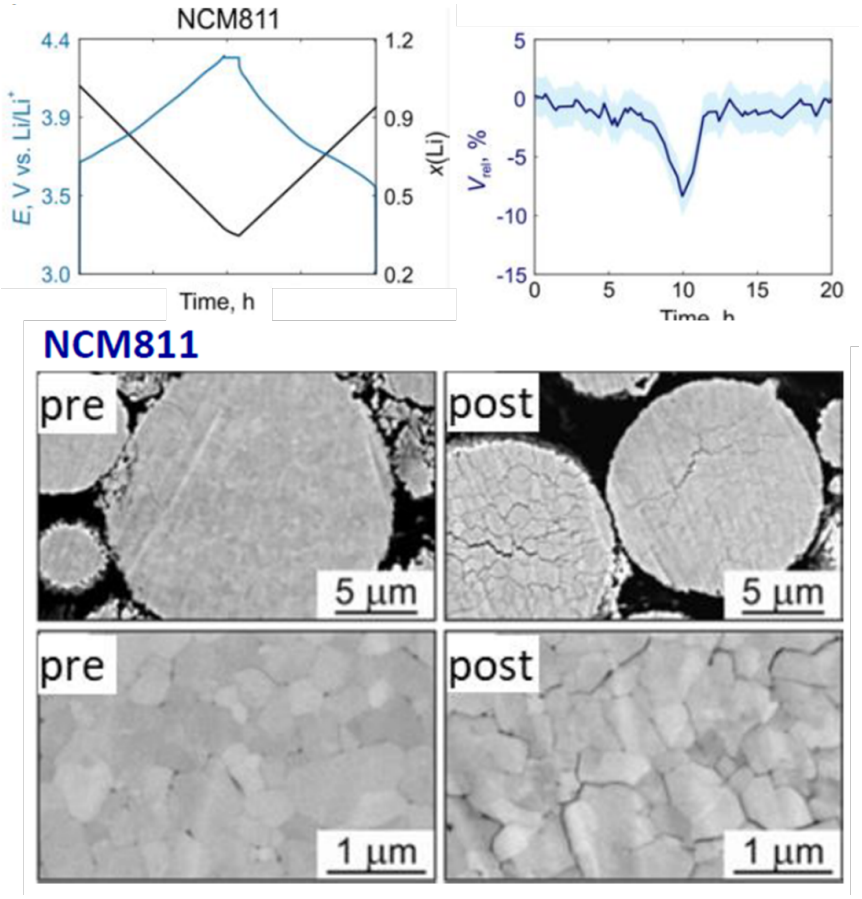

Figure 1.12 Anisotropic volume change in NCM811.[31] Reproduced with permission from Ref. 31. Copyright 2017 American Chemical Society.

The particle cracking can cause additional SEI to be created on the newly exposed surface induced by particle disintegration and may increase impedance.[31,32] Also, the particle may lose its electronic conduction pathways if the particle is isolated from the conductive carbon.[13,31]

Although Ni-rich strategy is attractive since a simple increase of Ni contents leads to considerable capacity increase, Ni-rich NCM cannot be considered for commercial application due to the reasons mentioned above. It is, therefore, crucial to come up with a different strategy in order to fulfill the energy needs from various power-hungry applications.[1,23] Instead of a

fundamental chemical approach, battery researchers worked closely with battery cell industries to optimize the design of the cells to utilize the inner spaces. However, due to the fundamental limitations in capacity from the battery materials, industries were faced with difficulties in further increasing the energy density of the battery. Rather than a temporary engineering solution, fundamental material innovations were needed to increase the capacity of the batteries while achieving safety and reliability.

1.2 Overview of lithium-rich layered oxide cathodes

Another way to improve capacity for lithium layered oxides is the implementation of lithium-rich layered oxides (Figure 1.13).[33] Lithium-rich layered oxides or high energy NCM (HE-NCM) achieve a single-phase solid solution composed of Li_2MnO_3 and $LiNiCoMnO_2$ (c Li_2MnO_3 (1-c) $LiTMO_2$ [TM = Ni, Co, Mn]).[4,34] The name "Li-rich" is due to Li_2MnO_3 possessing excess lithium in the Mn layer creating a so called "honeycomb structure".[34] The

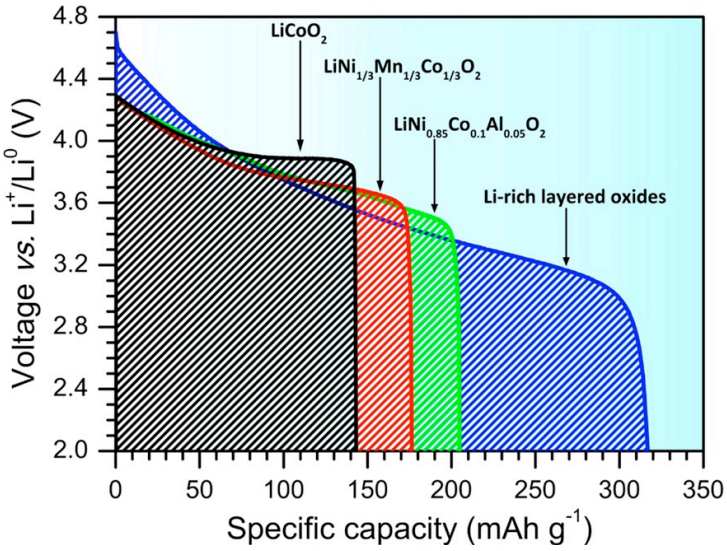

Figure 1.13 Discharge capacity comparisons among various cathode materials.[33] Reproduced with permission from Ref. 33. Copyright 2017 American Chemical Society.

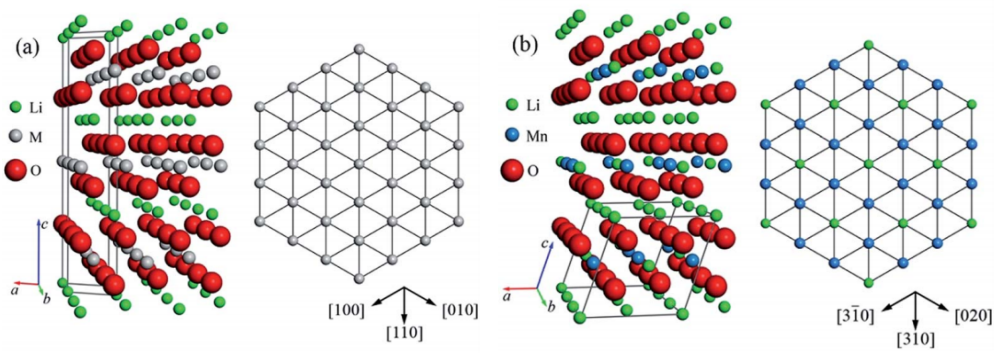

Figure 1.14 (a) Trigonal ($R\bar{3}m$) $LiTMO_2$ atom model (left) and atomic arrangement in the TM layer (right), (b) Monoclinic ($C2/m$) Li_2MnO_3 atom model (left) and atomic arrangement in the TM layer (right).[4] Reproduced with permission from Ref. 4. Copyright 2017 American Chemical Society.

HE-NCM positive electrode material drew a great deal of attention due to its high theoretical capacity of 270 mAh g^{-1} (Figure 1.14).[33] The synthesis of HE-NCM follows the same method that was used for NCM cathodes (co-precipitation).[34,35] To better understand Li-rich layered oxides, close attention towards the charging and discharging process as well as through understanding of its structural degradation processes are needed. During initial charging, when the voltage is below 4.4 V, lithium ions are de-intercalated from $R\bar{3}m$ $LiTMO_2$ lithium slabs (Figure 1.15).[36] A long plateau starts to develop at 4.5 V, which is accompanied by electrochemical activation of Li_2MnO_3 component.[36] During this activation process, Li from $C2/m$ Li_2MnO_3 is released along with oxygen.[36] The discharge process is the opposite process of the charging process. In this case, delithiated lithium ions are inserted back to the lithium sites in the $LiTMO_2$ and Li_2MnO_3.[36]

Despite its capacity advantage, HE-NCM suffers from structure degradations due to lattice oxygen release at high voltage operation.[36] The degradation mechanism is quite complicated

since the bulk and surface degradation (within 10 nm) are different. For surface degradation in detail, delithiation occurs from the solid solution c Li_2MnO_3 (1-c) $LiTMO_2$, and

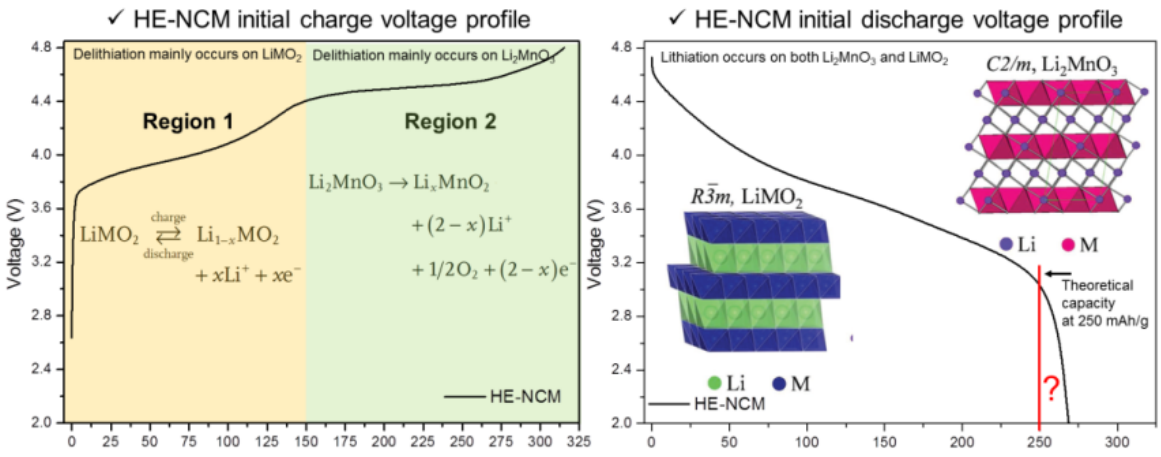

Figure 1.15 First cycle charge and discharge voltage profile of HE-NCM.

the structure changes to mainly rocksalt TMO until 4.4 V (Figure 1.16).[36] Delithiation continues to take place until 4.8 V, and the structure mainly changes to the disordered spinel TM_3O_4.[36] Discharge down to 2 V will lead to the relithiation of lithium ions in the vacant lithium site.[36] The structural transformation again occurs during the discharge process, and at 2 V, the majority of the surface structure of HE-NCM mainly becomes TMO, and a small portion of the structure becomes TM_3O_4.[36]

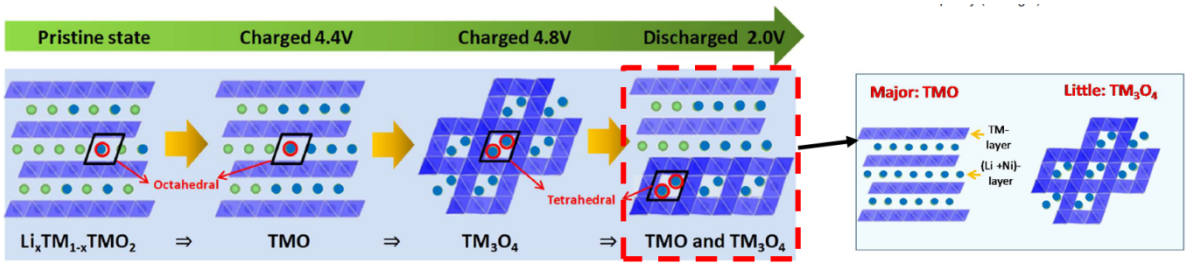

Figure 1.16 HE-NCM Surface degradation mechanisms in detail.[36] Reproduced with permission from Ref. 36. Copyright 2018 American Chemical Society.

For bulk degradation, the majority of the structure is monoclinic layered $LiTMO_2$, with a small amount of monoclinic layered Li_2MnO_3 being present (Figure 1.17).[36] During the charging process, lithium sites in Li_2MnO_3 become vacant due to delithiation. Some of the delithiated lithium cannot be lithiated back to the original lithium site due to the structural reorientation of Li_2MnO_3.[36] The formed lithium vacancy is filled up with transition metal during the discharge process. The transition metal slab is being glided to fill the lithium vacancy, and structure densification occurs by this process.[36]

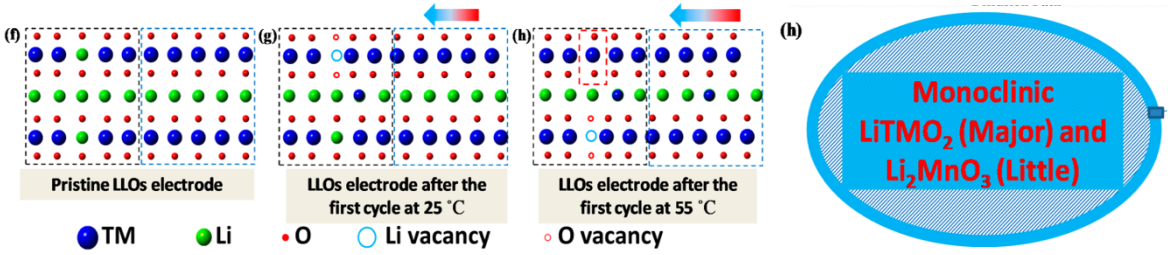

Figure 1.17 Bulk degradation of HE-NCM in detail (LLO = lithium-rich layered oxide).[36] Reproduced with permission from Ref. 36. Copyright 2018 American Chemical Society.

The degradation studies for surface and bulk HE-NCM elucidated how the structural transformation occurred during the electrochemical operation. However, the degradation process alone did not address the conundrum of exhibiting extra capacity caused by lithium-rich layered oxide cathodes. The commercial lithium-rich layered oxide from BASF SE (HE-NCM) has a composition of $Li_{1.33}Ni_{0.27}Co_{0.13}Mn_{0.60}O_{2+d}$. Based on the theoretical capacity calculation, HE-NCM should be exhibiting discharge capacity lower than 250 mAh g^{-1}. However, at a C/15 (the charge and discharge current when cell operation time is 15 hours) rate, HE-NCM produces the discharge capacity of approximately 275 mAh g^{-1} (Figure 1.16). Although many cathode researchers were puzzled about this unusual phenomenon, recent studies revealed an explanation with concrete experimental evidence.[37-42]

1.2.1 Introduction of Reversible Oxygen Anion Redox Process

The concept of a reversible oxygen anion redox process was suggested as a reason for the extra capacity contribution from lithium-rich layered oxide cathodes.[37-46] To better understand how this anion redox process works, understanding conventional cationic redox activity in LIB cathodes is needed first. For classical lithium layered oxides, cationic redox activity takes place to exhibit capacity.[6] For example, an LCO experiences a change in the oxidation state of Co^{3+} to Co^{4+} (cation redox activity) when delithiation takes place. However, for lithium-rich layered oxides, cations and anions (oxide ions) participate in redox activity during charging and discharging, which can lead to a high discharge capacity, sometimes exceeding theoretical capacity (Figure 1.18).[37]

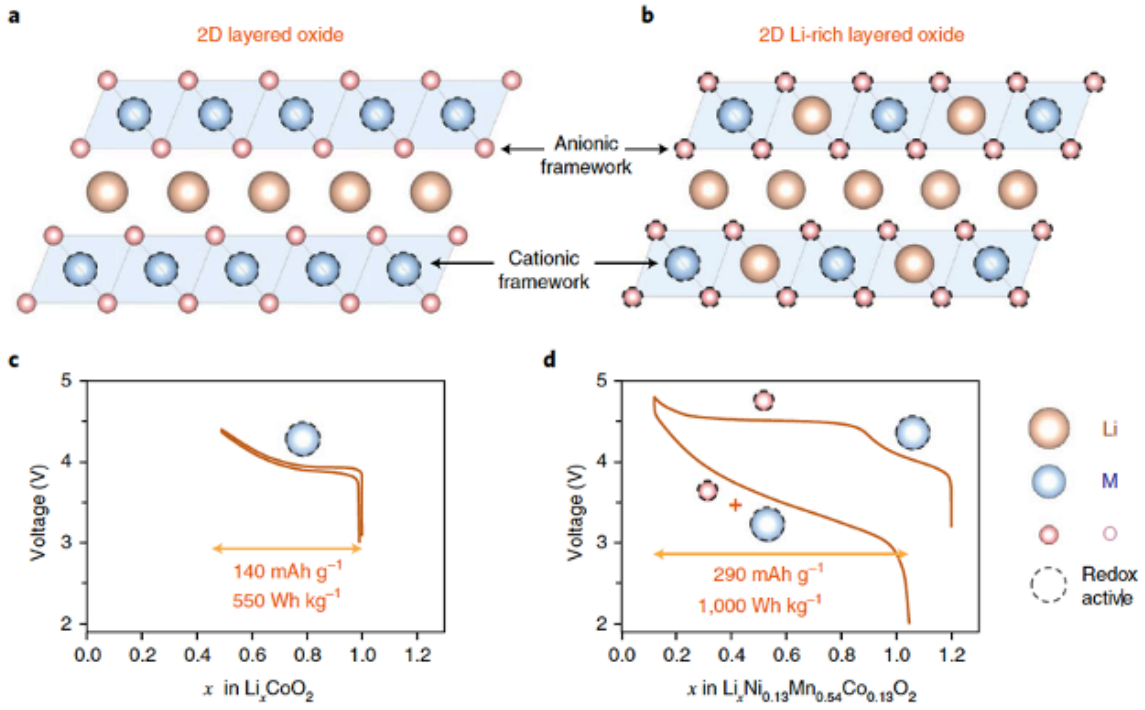

Figure 1.18 Illustration of cation and anion redox activity.[37] Reproduced with permission from Ref. 37. Copyright 2018 Springer Nature.

The reason behind Li-rich layered oxides exhibiting additional anionic redox activity is closely related to the arrangement of oxygen bonding within the transition metal slabs. In Li-rich NCM, an oxygen 2p orbital pointing towards a Li 2s orbital in Li-rich NCM is weakly bonded compared to the classical NCM where no Li exists in the TM layers. This weak binding behaves like an O 2p non-bonding orbital, and this non-bonding band is placed above the M-O band, which is a band induced from the interaction with TM's 3d orbitals and oxygen's 2p orbitals (Figure 1.19).[37]

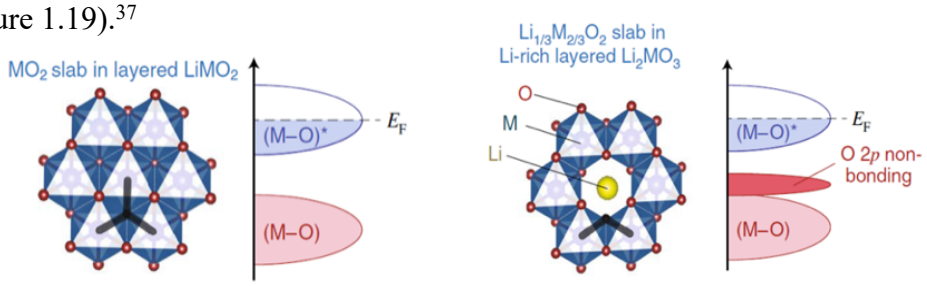

Figure 1.19 Band diagram of lithium layered oxide and Li-rich layered oxide.[37] Reproduced with permission from Ref. 37. Copyright 2018 Springer Nature.

The anion redox concept becomes more evident when the DOS is interpreted using Mott-Hubbard splitting (Figure 1.20).[37] The variable U represents the electron repulsion within d orbitals, and it is inversely proportional to the orbital volume. Delta is the energy difference between the M-O band and the M-O antibonding band. The partially filled M-O band can be

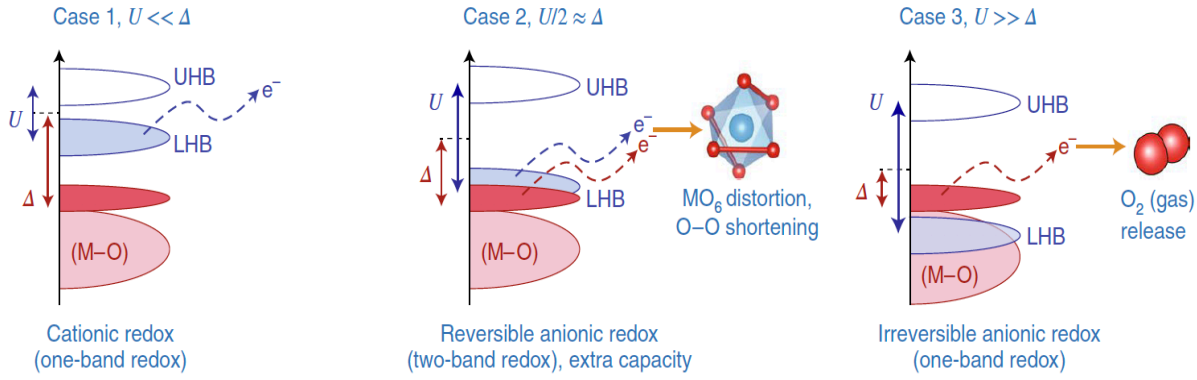

Figure 1.20 Process of cationic and anionic redox activity in detail.[37] Reproduced with

permission from Ref. 37. Copyright 2018 Springer Nature.

divided into an empty upper Hubbard band (UHB) and filled lower Hubbard band (LHB).[37,47,48] Case 1 is an example of cation redox activity that is taking place during the initial state of charging until approximately 4.4 V. In this case, LHB is placed above the non-bonding band, and electrons are moved from this band only. The electron repulsion gets larger during charging since the TM orbital volume reduces along with the delithiation process.[48]In region 2 when Li_2MnO_3 delithiation takes place, the electron repulsion becomes large enough that LHB is now at a similar energy level with the oxygen 2p non-bonding orbital. At this moment, cation & anion redox can coincide, and electrons are removed from both LHB and the non-bonding O 2p band and results in extra capacity.[37, 41, 48] Electron removal from these two bands induces degeneracy in the Fermi level, which then triggers J-T distortion.[37] When delithiation continues to take place, the electron repulsion gets even more substantial than before due to further oxidation of the TM, and the energy level of LHB is now below the energy level of the non-bonding O 2p band, which is shown in case 3. When this happens, electrons are solely removed from the non-bonding O 2p band, which yields to oxygen gas release and irreversible structure change.[37, 43]

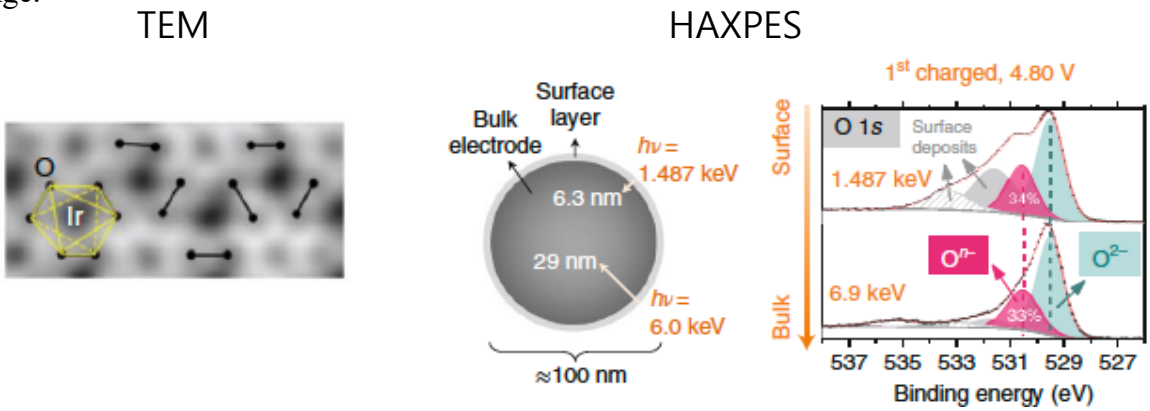

Figure 1.21 Experimental proofs for anionic redox activity.[37] Reproduced with permission from Ref. 37. Copyright 2018 Springer Nature.

The concept of anionic redox is confirmed by a series of experiments (Figure 1.21). The Jahn Teller distortion induced by anionic activity was directly observed by a transmission electron microscope (TEM).[37] Also, synchrotron-based bulk-sensitive hard X-ray photoelectron spectroscopy (HAXPES) was used to confirm oxide ion redox activity by performing the experiments during charge and discharge.[39, 41] The HAXPES not only can dive into the surface of the cathode particle, (~6.3 nm) but also scrutinize the bulk part of the cathode (~29 nm).

Recent studies from Bruce et al., further studied anion redox in lithium-rich NCM and the origin of oxygen loss was further scrutinized.[49-53] Based on multiple spectroscopic tools such as TEM and RIXS, along with DFT calculations, the group proved that irreversible in-plane migration of Mn occurs with oxide ion oxidation after the first cycle of Li_2MnO_3 activation.[49] This Mn migration is triggered by oxide ion oxidation. The weakened Mn – O bond due to the oxide ion oxidation promotes migration to the vacant lithium sites in the honeycomb structure and ultimately creates vacancy clusters.[49-52] The oxide ions trapped in the cluster bind and form molecular O_2. During discharge, molecular O_2 reduces back to oxide ions and the vacancy cluster is filled with lithium ions.[50] Due to the in-plane Mn migration during charging, lithium that was inserted to the vacancy cluster during discharge was not located at the original positions. The coordination of orphan oxygen induces higher energy O 2p state since the net interaction between Li – O after in-plane Mn migration is weaker than the net interaction between Li – O before in-plane Mn migration.[50,52,54] The higher energy state of O 2p is vulnerable from oxygen release due to the weaker bonding interaction.

The escaped oxygen can have many forms: O^{2-}, O^-, O_2^{2-}, and O_2.[17,55,56] These oxygen containing species then react with ethylene carbonate in the electrolyte and further produces side products such as LiF, polymer species, etc. which then deposit back to the cathode surface

to increase impedance (Figure 1.22).[14,57,58] Phase transitions also occur upon oxygen release.[25,55,59] When oxygen escapes from the lattice, TM in the octahedral site of the metal slab can be easily migrated to the octahedral site of the lithium slab. This phase transition from layered to spinel to eventually rocksalt structure drastically reduces capacity.[25,60,61]

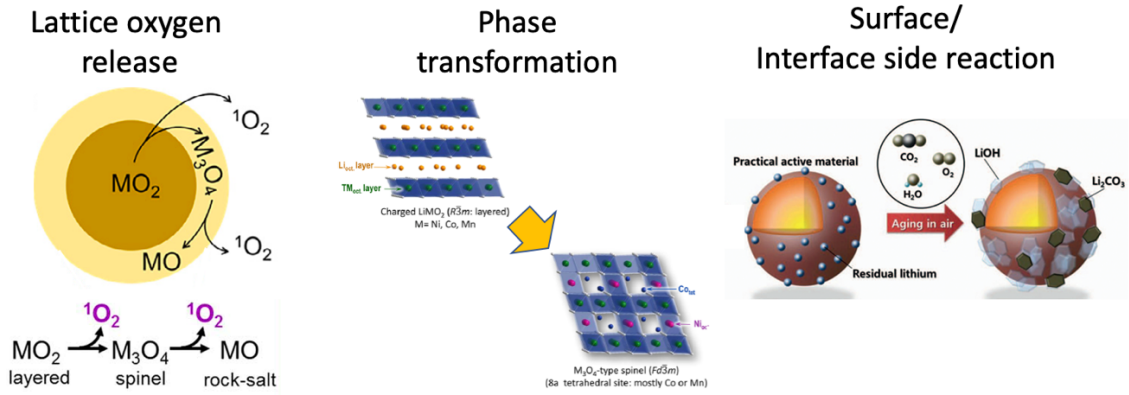

Figure 1.22 Drawbacks of Li-rich layered oxide [17,55,56] Reproduced with permission from Ref. 17 and 55. Copyright 2018 American Chemical Society and Elsevier.

1.3 Scope of This Thesis

In conclusion, it is needless to say that degradation of lithium-rich layered oxides are closely related to the surface of the cathode particles. Thus, an improvement in the cathode interface is greatly needed to address the abovementioned drawbacks. This thesis is focused on the surface modification of commercial lithium-rich layered oxides, also known as HE-NCM. Before mentioning the surface modification in detail (**Chapter 3**), characterization methods that were used during this research will be mentioned in the next chapter.

Chapter 2. Method of Characterization

2.1 X-ray Diffraction (XRD)

X-ray diffraction (XRD) is used to detect the bulk crystal structure as well as the phase of the materials.[62] In 1913, Bragg's law was first introduced to better understand diffraction data from materials.[62] From $n\lambda = 2d\sin\theta$, the diffraction data can be interpreted to conduct structural analysis.[62] The variable n is a positive integer, λ is the wavelength of the X-ray, d is the crystallographic plane distance also known as d-spacing, and θ is the angle between the X-ray and the crystallographic plane (Figure 2.1).[62] During XRD analysis, X-rays travel from the X-ray source, and the beam hits the crystal sample. The beams are reflected from planes in the crystal, and the distance traveled to the X-ray detector differs by one wavelength; thus, the value of n becomes 1. The scattered rays can constructively interfere, and this produces diffracted beams.[62] The instrument that was used for this thesis is a PANalytical Empyrean. Cu Ka radiation with λ = 0.15405 nm was used, and the instrument was functional at 40 kV with 30 mA. The Bragg-Brentano geometry was used for the sample scan (Figure 2.2).

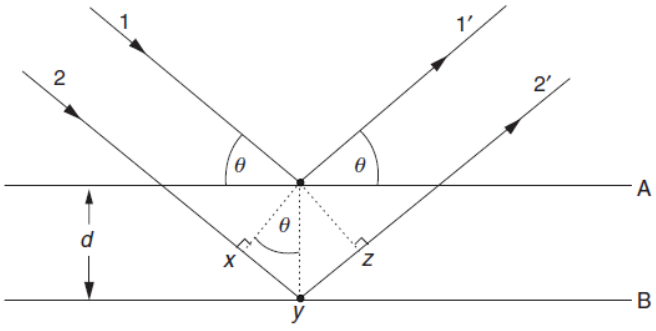

Figure 2.1 Illustration of Bragg's law.[63] Reproduced with permission from Ref. 63.

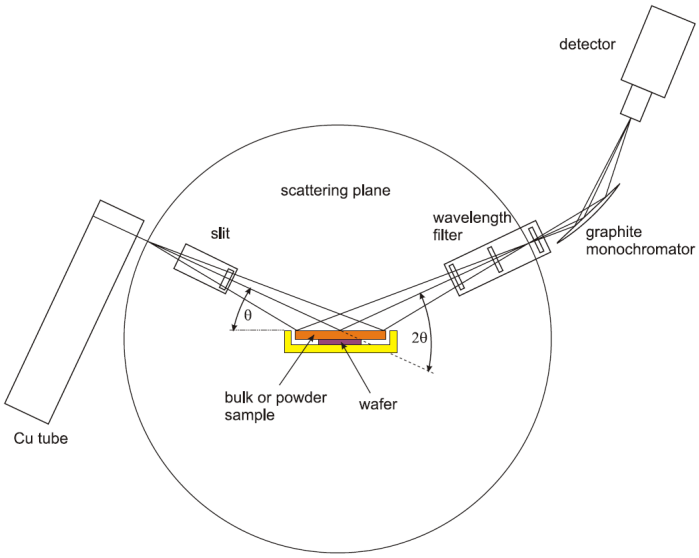

Figure 2.2 Illustration of Bragg-Brentano geometry of the XRD.[62] Reproduced with permission from Ref. 62 Copyright 2014 from John Wiley & Sons.

2.2 X-ray Photoelectron Spectroscopy (XPS)

X-ray photoelectron spectroscopy (XPS) utilizes X-rays to hit the surface of the sample in an effort to generate photoelectrons (Figure 2.3).[62,64] The generated X-rays from the equipment are focused on the sample, and they have the energy to ionize the sample and yield kinetic energy (KE). Since the energy of the incident X-ray photon (hv) is the energy value from the equipment, electron ionization energy (binding energy [BE]) can be determined by the photon energy subtracted by the kinetic energy. Since the binding energies for the core electrons of an element are unique, element identification is possible.[62, 65] The depth of which XPS can probe is about 10 nm. A Thermo VG ESCA Lab 250 was used for this thesis study.

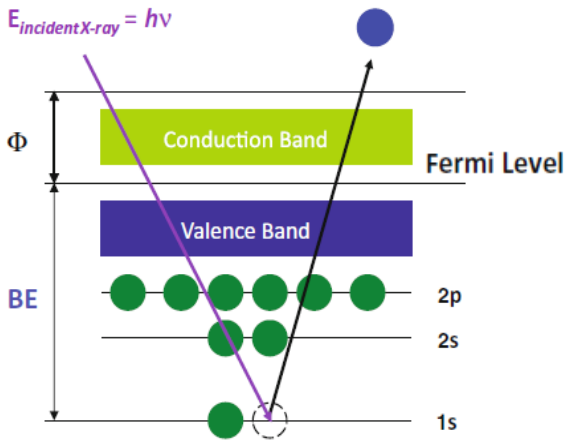

Figure 2.3 Photoelectron emission process.[64] Reproduced with permission from Ref 64.

2.3 Scanning Electron Microscopy (SEM) and Energy Dispersive X-ray Spectroscopy (EDS)

Scanning Electron Microscopy (SEM) is an electron reflection technique which is used to identify the localized morphology of the sample.[62] A highly energized electron beam hits the sample, and this interaction generates secondary electrons (SE), backscattered electrons (BSE), and characteristic X-rays (EDS) (Figure 2.4).[62] The bonded electrons from the sample are taken out by the incident electron beam and yield to secondary electrons. These secondary electrons typically have a depth of approximately 10 nm.[62] The electrons with a degree of scattering angle above 90 degrees are identified as BSE. They can be utilized for identifying heavy elements since the degree of scattering is higher for the heavy elements.[62] Due to the higher energy of BSE, the depth of BSE is up to 3 um. In the process of SE ejection, the excitation of the low binding energy shell electron creates a vacancy of the electron site. Along with this, excess energy is then released as a form of X-ray.[62] This can be collected by an EDS detector and identify the sample's element since the X-ray emitted from excess energy is dependent on the element's unique orbital.[62] Zeiss FESEM 1530 was used for SEM and EDS for this thesis

study.

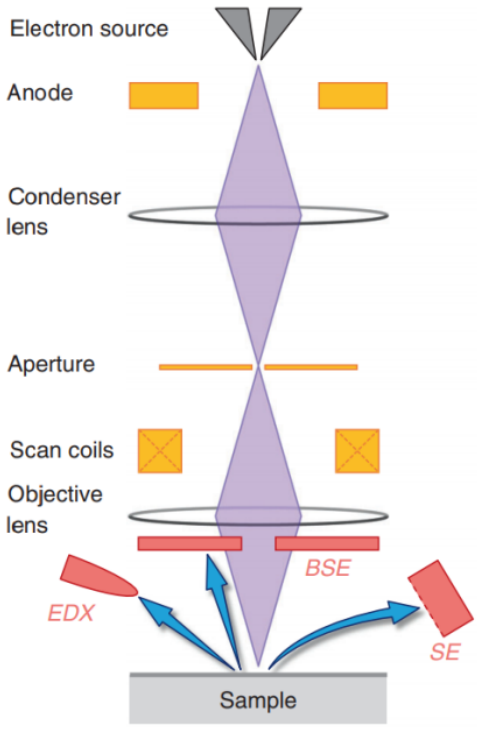

Figure 2.4 Scheme of a scanning electron microscope.[62] Reproduced with permission from Ref. 62 Copyright 2014 from John Wiley & Sons.

2.4 Transmission electron microscopy (TEM)

To identify structural information, transmission electron microscopy (TEM) was used. Due to its high resolution of 10 Å, TEM is an ideal localized analysis for observing extreme features such as the surface of a small particle.[62] Instead of electron reflection, such as in the case of SEM, TEM utilizes undiffracted beams (Figure 2.5).[62] The FEI Titan 80-300 HB in McMaster University Canadian Centre for Electron Microscopy was used for this thesis study.

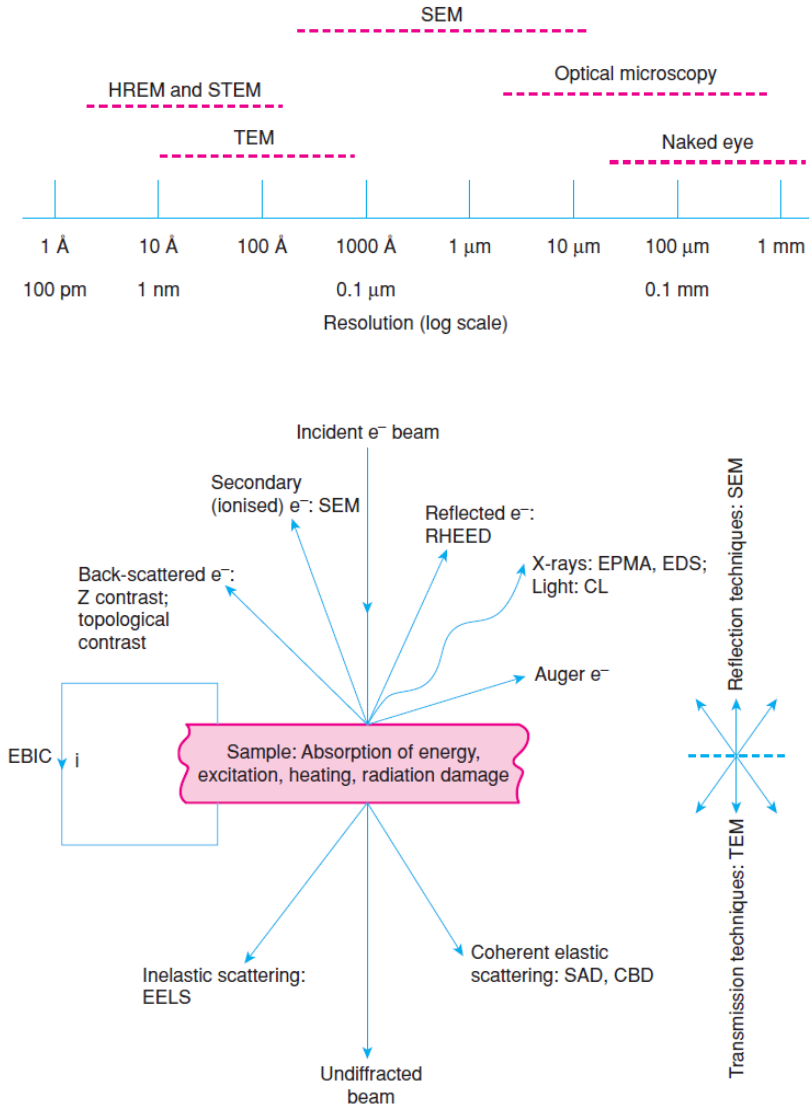

Figure 2.5 Difference between SEM and TEM and their resolution.[62] Reproduced with permission from Ref. 62 Copyright 2014 from John Wiley & Sons.

2.5 Raman Spectroscopy

The excitation of an atom's vibrational modes in a solid is possible by light scattering.[62] The laser was used to scatter light to the sample. When light interacts with molecules in a sample, the energy level of the incident photons should be mostly the same as the energy level of the scattered photons.[62] However, a small number of the scattered photons will have a

different frequency, thereby exhibiting a small difference in energy.[62] This difference is defined as the Raman shift. The chemical bonds experience a deformation of electron clouds (polarization) when they interact with a laser.[62] The interactions then provide Raman active bands, which can be used to find structural information on the sample.[62] The Raman instrument that was used for this thesis study is a Horiba Raman spectrometer T64000 with a 532 nm laser excitation wavelength.

2.6 Galvanostatic charge/discharge Cycle Test

The electrochemical performance of the surface-modified cathodes was tested using a galvanostatic charge/discharge cycle test. Since this study is a part of the BASF Battery Network project, there was a specific electrochemical testing protocol that needed to be followed (Table 1). The testing protocol for the cycling test is the following:

Table 1. The BASF Battery Network protocol

Step	Cut-off critarion	C-rate charge	C-rate discharge	No. of cycles
Activation	4.8-2.0 V vs. Li+/Li	C/15-CC	C/15-CC	1
Stabilization	4.7-2.0 V vs. Li+/Li	C/10-CC	C/10-CC	3
Fast cycling	4.7-2.0 V vs. Li+/Li	C/2-CCCV	3C-CC	3
Slow cycling	4.7-2.0 V vs. Li+/Li	C/2-CCCV	1C-CC	33
Repeating the entire steps for 8 times (exception for activation step)				

The C-rate is a rate at which a battery is charged/discharged. For instance, a 1C rate is defined as the rate at which the battery is fully charged/discharged in 1 hour with CC representing constant current. Since this is a galvanostatic experiment, the constant current was applied to the cell. The abbreviation CCCV stands for constant current-constant voltage. When the cell reaches a target voltage (e.g., 4.7 V), the current decays exponentially in order to

maintain its voltage. The reason for performing CCCV is closely related to reaching the originally targeted state of charge (depth of discharge for cathode). The cell cannot achieve the targeted state of charge due to overpotential. Thus, the current decays slowly by performing a CV step after the CC step of charge. This minimizes the cell's overpotential which allows for the anode and cathode to lithiate and delithiate to achieve the desired state of charge.

The activation step was performed to activate Li_2MnO_3 in the cathode. Also, a very slow stabilization step was added for the purpose of creating a robust SEI and also to observe charge/discharge performance at a minimum overpotential operating environment. A Maccor Series 400 Automated Test System was used to perform cycle tests for this thesis study.

2.7 Electrochemical Impedance Spectroscopy (EIS)

The performance of an electrochemical cell is highly dependent on its impedance. Alternating current (AC) impedance analysis is used to identify the response of the current in the alternating current environment to obtain inductance, capacitance, and resistance values.

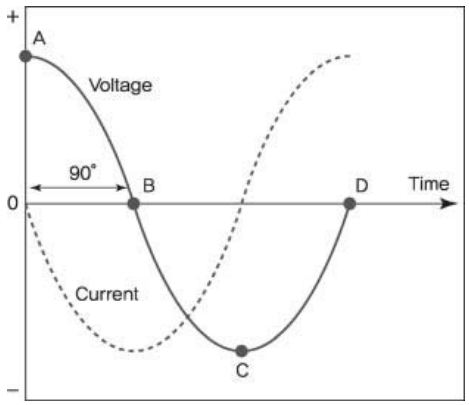

Figure 2.6 Voltage and current phase difference.[5] Reproduced with permission from Ref. 5 Copyright 2012 from John Wiley & Sons.

When a sinusoidal potential is applied to the cell, current changes as a response to such excitation.[5] This current also has the representation of a sinusoid with the same frequency. However, the phase is shifted as represented in Figure 2.6.[5]

Considering phase differences for voltage and current as well as Euler's relationship, mathematical representations of impedance is the following (Equation 2.1):

$$V_t = V_0 \sin(\omega t) = V_0 \exp(i\omega t), I_t = I_0 \sin(\omega t + \emptyset) = \exp(i\omega t - \emptyset), \omega = 2\pi f$$

$$|Z(\omega)| = \frac{V(t)}{I(t)} = \frac{V_0 \sin(\omega t)}{I_0 \sin(\omega t + \emptyset)} = Z_0 \frac{\sin(\omega t)}{\sin(\omega t + \emptyset)} = Z_0(\cos\emptyset + i \sin\emptyset)$$

Where V_t is the potential at time V_0 is the amplitude of the signal

ω is the angular speed, f is frequency and $\emptyset$ is the phase shifted amount

Equation 2.1 Mathematical representations of impedance [5]

Impedance can be represented as a diagram in the complex plane. This plot is known as a Nyquist plot (Figure 2.7).[5]

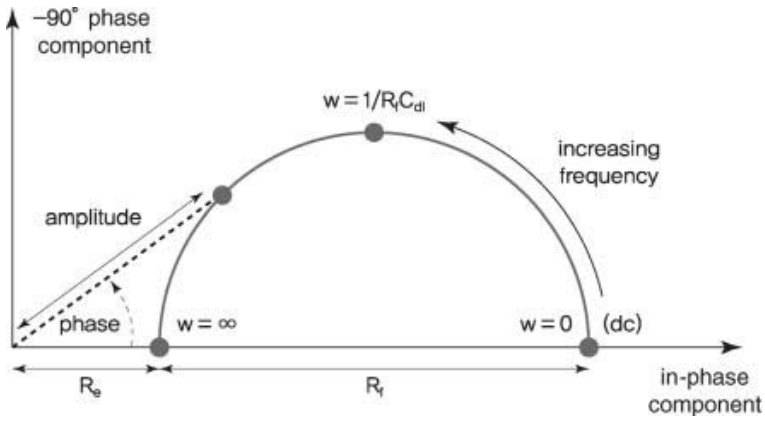

Figure 2.7 Illustration of Nyquist plots.[5] Reproduced with permission from Ref. 5 Copyright 2012 from John Wiley & Sons.

When θ (phase angle) is zero, the impedance only exhibits the real part. Thus, there should be no value on the y-axis and only the x-axis is represented on the Nyquist plot.[5] The value of the y-axis can be shown if there is a capacitance value. The Nyquist plot of LIB can be represented in the right Nyquist plot in Figure 2.7.[5] Besides the ohmic resistance (R_s or R_{ohm}), which is due to the resistance from the electrolyte, separator, and contact resistance from the cell terminal, the plot can be divided into three different sections of high, middle and low-frequency range region.[11, 66-77] The high-frequency region can be recognized to be between 1000 to 100 Hz, and this area has a semi-circle in which the diameter value of the circle is designated to the film resistance of the electrode (R_{SEI}). The middle frequency is within the frequency range of 10 to 0.1 Hz, and the diameter of the semi-circle in this region is closely related to the charge transfer resistance (R_{ct}) of the electrode during electrochemical operation. Lastly, the low-frequency region is designated to the frequency below 0.1 Hz, and this region is used to analyze the diffusion resistance of the electrode (R_{diff}). A Biologics VMP3 potentiostat was used to perform EIS for this thesis study. The results from EIS were carefully fitted to retrieve resistance values using EC-Lab software from Biologics.

Chapter 3 Li-Mo-O Coating on High Energy Lithium Layered Oxide

3.1 Introduction

The advent of lithium-rich layered oxide cathodes and their anionic redox capability paved a ground towards next-generation high capacity LIB.[38] A commercial Lithium-rich NCM cathode (HE-NCM), for instance, outperformed classical high-nickel NCM cathodes by both capacity and production cost.[37] However, the cycle stability of HE-NCM is somewhat questionable, thus making it difficult to use in real-life applications.[34,35] Many previous studies have shown that the oxygen loss and structural degradation of HE-NCM begins from the surface of the cathode (Table 2).[25,55,60,61,78] Therefore, performing a treatment on the HE-NCM surface was logical to prevent structural deterioration and cathode surficial lattice oxygen loss. Multiple surface modification methods were implemented to suppress the degradation.[71,79-101]

Table 2 Previous studies on variety of cathode surface modifications[102-115,148]

Coating	Coating precursor	Cathode	Calcination Temp (°C)	Method	Journal	Authors	Year
MoO_3	MoO_3	Li-rich NCM	790	Ball milling	RSC Adv.	Y. Gao & D. Li	2016
WO_3	$(NH_4)_{10}H_2(W_2O_7)_6$	NCM811	450 in argon	Wet coating	ACS Appl. Mater. Interface	D. Becker & M. Winter	2019
ZrO_2	zirconium (IV) butoxide in butanol & EtOH	NCM811	450 - 800	Wet coating	Adv. Energy Mater.	F. Schipper & D. Aurbach	2018
MgO	MgO	LCO	600	Pulsed laser deposition	Electrochemistry	K. Yamamoto & Z. Ogumi	2014
$LiAlF_4$	$AlCl_3$, lithium tert-butoxide, TiF_4	NCM811	200 - 300	ALD	ACS Nano	J. Xie & Y. Cui	2017
Li-Nb-O	lithium niobium ethoxide	NCM811	500	Wet coating	ACS Appl. Mater. Interface	F. Xin & M. S. Whittingham	2019

For instance, polyimide coating was performed on Li-rich NCM from polyamic acid

as a coating precursor.[101] The logic behind this coating was due to polyamic acid's strong affinity to the transition metal oxide surface, thus enabling the ability to establish continuous protective polyimide layers on the cathode. Despite the claim, insignificant cycle stability improvement was shown on the polyimide layer coated cathode compared to the non-coated Li-rich NCM. Other studies tried inorganic materials as coatings for the cathode.[30,84,98,116-122] For example, the utilization of LiF as a coating material was reported to be beneficial for cycle stability.[98] The existence of an already fluorinated protective surface may prevent from HF attack, thereby preventing transition metal dissolution from the cathode structure. However, the coverage of inorganic material coating often can be imperfect, and the exposed surface may still experience structural degradation over cycles.

Winter et al. performed a tungsten oxide coating on NCM811 to improve its cycle stability.[106] By reacting residual lithium on the NCM811 surface with ammonium tungstate at 400 °C, WO_3 and/or Li_2WO_4 were formed. Although the exact coating composition could not be identified due to the limited analysis techniques and the nature of small thickness of the coating, the tungsten oxide coated NCM811 exhibited improved cycle stability. Winter et al. claimed that the improved cycle performance is attributed to the protective shield of the tungsten oxide coating against electrolyte which allowed delaying cathode lattice oxygen release.[106]

Li et al. utilized MoO_3 to coat Li-rich NCM to improve its electrochemical performance.[105] Instead of the commonly used wet coating method, mechanical ball milling was used to break down the micron sized MoO_3 particles to nano-chunks. It was then mixed with Li-rich NCM and heat treated at 790 °C. Li et al. claimed that they had formed a MoO_3 coating along with a spinel phase formation upon heat treatment with MoO_3 and Li-rich

NCM.[105] The spinel formation was actually beneficial towards the rate performance since the phase has 3-dimensional lithium ion diffusion pathways thereby improving ion diffusion. Also, the MoO_3 coating can reduce the side reactions between the electrode and electrolyte during battery cycling and this ultimately reduces the impedance of the coated cathode. However, the paper did not clearly explain how the spinel formation was established during the synthesis step. Also, the paper failed to explain the relationship between the MoO_3 coating and the spinel phase.

Aurbach et al. demonstrated the viability of a ZrO_2 coating on NCM811 by using zirconium butoxide in butanol and ethanol.[148] The group claimed that reduced voltage hysteresis was observed from the ZrO_2 coated NCM811 during 700 ^oC heat treatment in air. The group also performed cross-sectional SEM and EDS analysis and proved that the Zr migration occurred on the coated NCM811 up to 4 um from the cathode surface. The group claimed that the enhanced electrochemical performance is attributed to the combination of the ZrO_2 coating as well as Zr doping. [148] However, the effects from the coating and doping were not well separated to observe the improvement independently to quantify which effect is more beneficial towards the electrochemical performance.

Regardless of different coating materials, coating strategy on cathodes seems beneficial as a means to delay cathode degradation.[102-115,148] For this thesis study, Li-Mo-O coating and Mo^{6+} surface diffusion are introduced as a surface modification strategy on HE-NCM. This suggested modification has also shown promising cycle stability. Several characterizations were performed on the modified material in order to understand the cause of the stability compared to none-modified HE-NCM.

3.2 Lithium Molybdenum Oxide (Li_xMoO_3)

Molybdenum trioxide is an interesting material due to its reversible intercalation /deintercalation of alkali ions.[123] In addition to its ability to accommodate lithium ions into the lattice, the electronic conductivity of MoO_3 increases along with the degree of ion intercalation, which results in changing its electronic property from insulator to semi-conductor.[123] A coating that possesses an insulating property at high voltage (> 4.5 V) can help to prevent electrochemical oxidation of ethylene carbonate (EC) in the electrolyte.[24] EC oxidation may result in OCV drop due to impedance increase caused by deposition of reacted products.[24] Gas generation from EC oxidation such as CO and CO_2 generation is also detrimental as the gases can be trapped into the electrode pores and this reduces electrochemical active areas.[24] A coating that has a semi-conductor property at low voltage may increase the intercalation/deintercalation rate performance of the cathode due to enhanced electron charge transfer.[124] Due to such advantages, MoO_3 was considered by many researchers as a cathode material in the LIB application.[123] Structural studies were performed to further verify the viability of battery applications by other research groups.[123] There are different types of MoO_3, and the most frequently studied types are listed in Figure 3.1.[123] For battery active material applications, a crystalline form of MoO_3 is preferred over amorphous MoO_3 due to a higher and flatter voltage profile, as was shown in the previous studies.[123] The most thermodynamically stable form is α-MoO_3, which consists of a double sheet of MoO_6 octahedra (Figure 3.1 a).[123] To explain its structure in detail, the structure is organized as edge-sharing chains of the octahedron in which two chains of octahedral edges are shared to establish layers. These layers of MoO_6 are then stacked along the c-axis in a staggered fashion by van der Waals forces.[123] Other types of MoO_3 are the metastable cubic β-MoO_3 (Figure 3.1 b) and

hexagonal h-MoO_3 (Figure 3.1 c). Due to the vacancy in their structure, intercalation of alkali ions is possible.

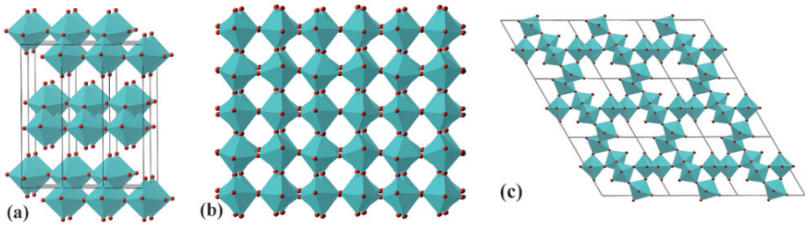

Figure 3.1 Structures of molybdenum trioxide: (a) layered α-MoO_3, (b) cubic β-MoO_3, and (c) hexagonal h-MoO_3.[123] Reproduced with permission from Ref. 123. Copyright 2009 from Royal Society of Chemistry.

The electrochemical properties were studied in detail from studies by other researchers as well.[125] A series of galvanostatic tests were performed on various MoO_3 (Figure 3.2).[125] According to the stoichiometry of α-MoO_3, Li_2MoO_3 can be made upon lithiation. In the process of lithiation, the oxidation state of Mo can change from Mo(VI)O_3 to LiMo(V)O_3 and Li_2Mo(IV)O_3, assuming full lithiation in MoO_3.[125] However, the galvanostatic test confirmed that α-MoO_3 could only accommodate approximately 1.5 Li per Mo.[125] The capacity, however, exhibited from α-MoO_3 is around 280 mAh g^{-1} which can be considered as a reasonably high capacity cathode compared to other layered oxide cathodes.

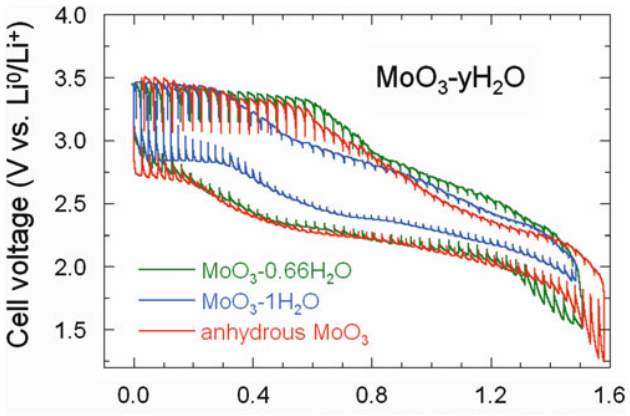

Figure 3.2 Charge/discharge voltage profile of various MoO_3.[125] Reproduced with permission

from Ref. 125. Copyright 2016 from Springer Nature.

The other benefit of using MoO_3 as a battery material is related to its variable electronic conductivity upon (de)lithiation.[124] Studies by other group suggested that with lithiation in the MoO_3 lattices, electrons are introduced into the conduction bands, thereby increasing electronic conductivity. Although there are variations on the absolute value of electronic conductivity increase upon lithiation, the trend of increasing conductivity with ion insertion was in agreement with different literature sources (Figure 3.3).[123, 124]

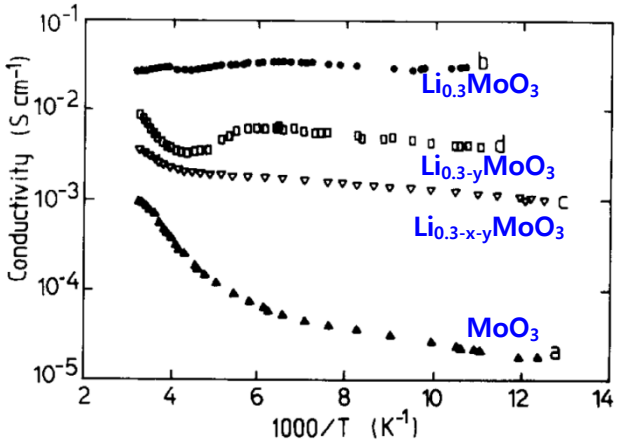

Figure 3.3 Electronic conductivity values of lithiated α-MoO_3 from various literatures.[123] Reproduced with permission from Ref. 123. Copyright 2009 from Royal Society of Chemistry.

The lithium diffusion coefficient was investigated by other researchers to find the ionic conductivity of MoO_3 (Figure 3.4).[123] Based on the Li^+ transference number as well as the chemical diffusion coefficient and thermodynamic factors, Li^+ ionic conductivity was identified, and the maximum value of 10^{-4} S cm^{-1} was found for x = 0.7 which is relatively high for ionic conductivity considering the ionic conductivity of a typical LIB cathode, NCM111, is

approximately 10^{-8} S cm^{-1}.[123]

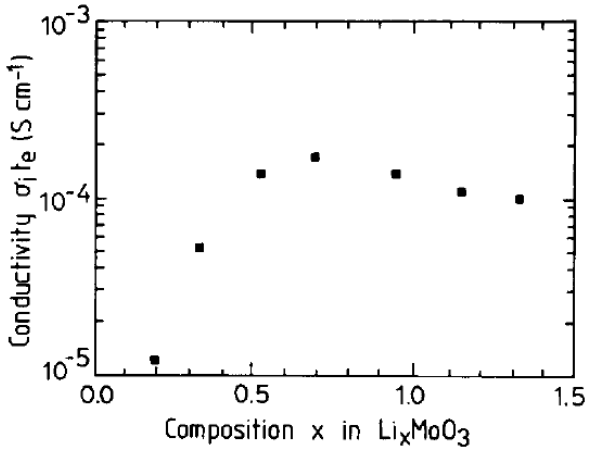

Figure 3.4 Ionic conductivity of Li_xMoO_3.[123] Reproduced with permission from Royal Society of Chemistry. Reproduced with permission from Ref. 123. Copyright 2009 from Royal Society of Chemistry.

Although MoO_3 has many advantages for use in LIB materials, it often undergoes severe discharge capacity degradation over cycles due to structural collapse and subsequent

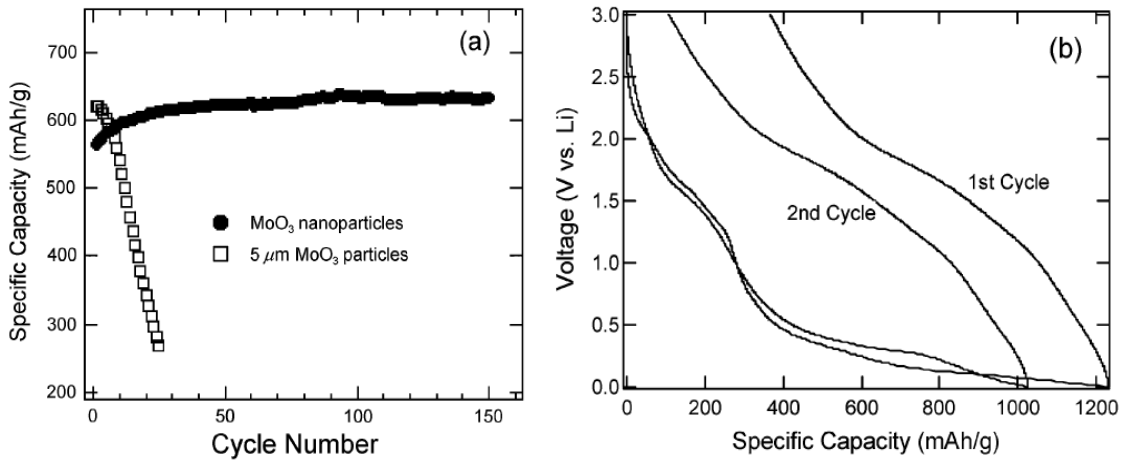

Figure 3.5 Size effect of MoO_3. (a) Improved performance of MoO_3 nanoparticle vs micron-sized MoO_3. (b) First and second cycle voltage profile from MoO_3 nanoparticle.[126] Reproduced with permission from Ref. 126. Copyright 2008 from John Wiley and Sons.

loss of electronic conductivity as it was suggested by Lee et al.[126] Therefore, various studies were performed to mitigate capacity degradation. One of the effective methods to improve the cyclability is with size reduction of the MoO_3 particles (Figure 3.5).[126] A study revealed that 5-\20 nm of α-MoO_3 nanoparticles synthesized by the chemical vapor deposition method was used as an anode material. The study revealed that the size of the MoO_3 particles differentiate the cycle performance upon frequent (de)lithiation.

Besenhard et al. demonstrated chemical lithiation of MoO_3 using lithium iodide. The group showed an improve cycle performance over non-lithiated MoO_3.[124] Galvanostatic cycle tests were performed on Li_xMoO_3 with x = 0, 0.1, 0.25, 0.5 and 1 (Figure 3.6). The samples, with lithiation, were exhibiting improved cycle performance because of improved electronic conductivity from chemically lithiated MoO_3 and the robust establishment of a MoO_3 lithiated phase.

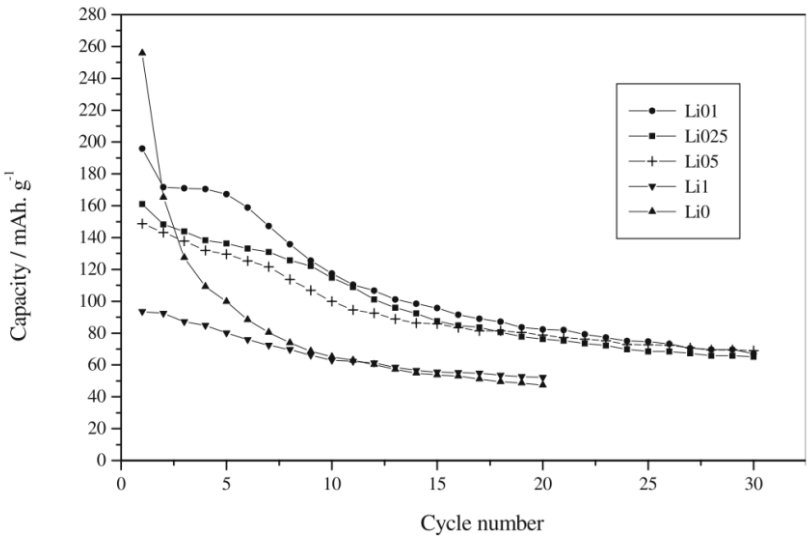

Figure 3.6 Cycle test on Li_xMoO_3 with x = 0, 0.1, 0.25, 0.5 and 1.[124] Reproduced with permission from Ref. 124. Copyright 2007 from Springer Nature.

3.3 Li_xMoO_3 Coated High Energy Lithium Layered Oxide

3.3.1 Synthesis

For this thesis study, nano-sized Li_xMoO_3 was used to coat HE-NCM due to the advantages of improved electronic conductivity and enhanced stability from the nano-sized morphology stated in section 3.2. Therefore, commercially available MoO_3 (Sigma Aldrich) needed to be exfoliated first since the sheet of MoO_3 is stacked like a sandwich as an agglomerated MoO_3 with the particle size of approximately 10 um. There are a number of exfoliation methods for MoO_3.[127-129] Several exfoliation approaches (high-intensity sonication with a solvent, liquid exfoliation method using isopropanol and water, etc.), were applied, and they were not successful. Inspired by chemical exfoliation of graphene, a similar analogy was applied to synthesize MoO_3 nanoparticles.[129] A previous study from Shukoor et al. examined the possibility of MoO_3 chemical exfoliation by using amine and nitric acid.[129] Instead of using commercial MoO_3, layered molybdic acid (MoO_3 $2H_2O$) was applied as a precursor. The exfoliation procedure is as follows. Molybdic acid (10 mM) and octylamine (5mM) were added in a solution containing ethanol (33%) and water (66%). The mixture was then vigorously stirred for 48 hours to evaporate the solution. The remained composite was then stirred with

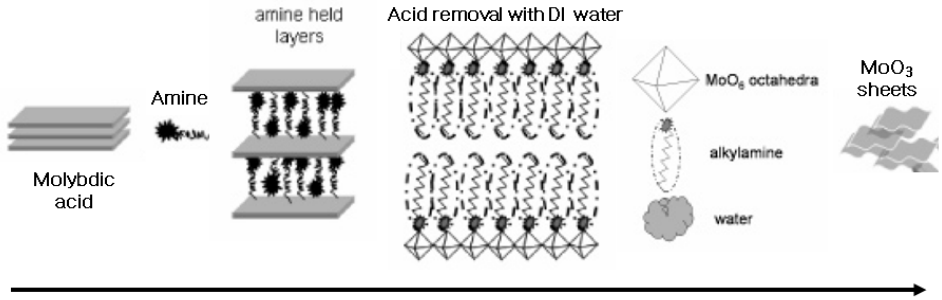

Figure 3.7 Exfoliation MoO_3 synthesis process.[129] Reproduced with permission from Ref. 129. Copyright 2006 from American Chemical Society.

33% nitric acid for 48 hours. The mixture was washed with deionized water several times to remove the acidity of the solution by carefully monitoring the pH. The reason for using molybdic acid is closely related to the presence of H_2O molecules in between MoO_6 octahedral layers (Figure 3.7).[129] Intercalation of octylamines was possible by replacing residing H_2O with octylamines. The driving force for intercalation is related to the proton transfer from the OH group of the molybdic acid to octylamine and attraction from the electrostatic force between positively charged octylamine and negatively charged MoO_6 layers.[129]

		morphology	
sample	d_L (d spacing)	amine intercalated	acid treated
MoO_3−PA	12.988 Å	hexagonal lamellar sheets	rods of 50−200 nm diameter and a few micrometers in length
MoO_3−BA	13.43 Å	mixture of sheets and scrolls	rods and scrolls <60 nm in diameter and of length around 1 μm
MoO_3−OA	23.2 Å	sheets of oxide−amine composite	disks, platelets of sizes 100−250 nm along with low percentage of rods
MoO_3−DDA	22.19 Å	mixture of rods and sheets	rods and sheets of various sizes
MoO_3−HDA	37.8 Å	nanorods of oxide−amine composite	rods of length 200 nm and <60 nm in diameter

Figure 3.8 Different MoO_3 morphology after various amine intercalation.[129] Reproduced with permission from Ref. 129. Copyright 2006 from American Chemical Society.

According to Shukoor, the morphology of synthesized MoO_3 is highly dependent on the kind of amine used (Figure 3.7). Depending on the length of the amine (from propylamine to hexadecylamine), the final morphology of MoO_3 after acid treatment diversifies from rods to sheets (Figure 3.8). Since the application of the synthesized MoO_3 is for HE-NCM coating, octylamine was chosen as it can yield sheets of MoO_3. Utilizing the exfoliation study by Shukoor et al., exfoliation of molybdic acid was performed for this thesis study as well.

Contrary to the data from Shukoor et al., the morphology of the synthesized MoO_3 after DI water washing was not a sheet, but more hexagonal nanorods (Figure 3.9 c).

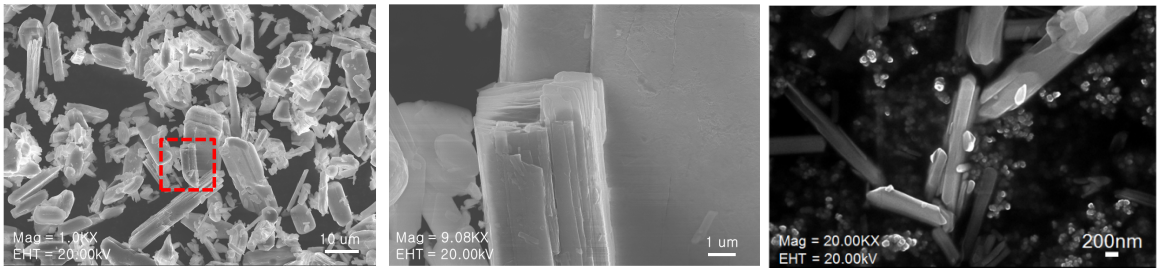

Figure 3.9 (a and b) None exfoliated MoO_3, (c) H_xMoO_{3+y} from molybdic acid exfoliation

The synthesized H_xMoO_{3+y} was then used to initiate chemical lithiation with LiI (Equation 3.1). Utilizing the technique from Besenhard et al., H_xMoO_{3+y} was stirred with dry LiI in water-free hexane solution in an Ar filled glovebox for 24 hours.[124] Since the electronic and ionic conductivity of the lithiated MoO_3 can be increased starting from x = 0.2, the amount of LiI was calculated accordingly to synthesize $Li_{0.2}H_xMoO_{3+y}$. The chemical reaction that took place during this step is the following (Equation 3.1):

$$2H_zMoO_{3+y} + 2LiI \rightarrow 2Li_xH_zMoO_{3+y} + I_2$$

Equation 3.1 Chemical lithiation of H_zMoO_{3+y} using LiI [124]

Iodine was made along with lithiated H_zMoO_{3+y} during the chemical lithiation of MoO_3. Thus, I_2 was carefully removed after stirring by washing $Li_xH_zMoO_{3+y}$ with hexane several times. The color of the $Li_xH_zMoO_{3+y}$ was deep blue in color confirming that Li was intercalated in H_zMoO_{3+y}. XRD was used to examine the structural information on the synthesized H_xMoO_{3+y} and its lithiated version (Figure 3.10). The XRD data confirmed that

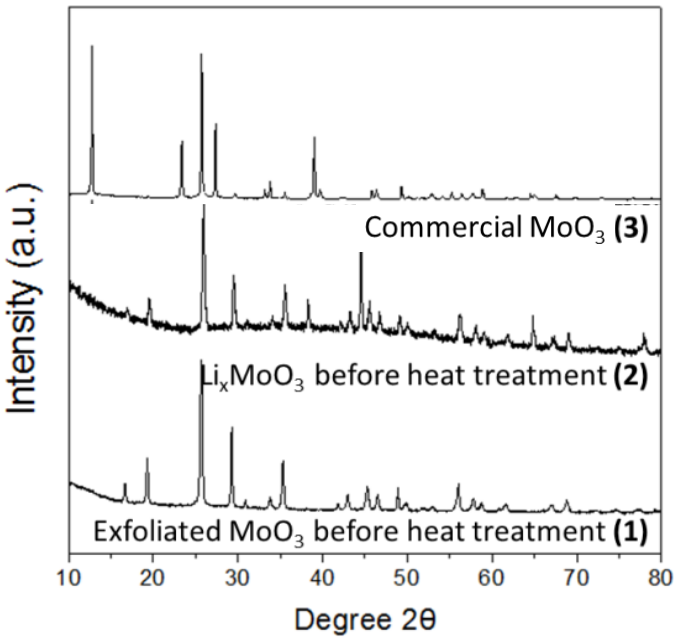

Figure 3.10 XRD data of commercial and synthesized H_xMoO_{3+y} and its lithiated version

the final product of MoO_3 was H_xMoO_{3+y}, which has a hexagonal bronze structure with a *P6₃/m* space group. Another literature source confirmed the legitimacy of the exfoliation result as they claimed that hexagonal MoO_3 was synthesized when nitric acid was used.[131] The synthesized lithiated H_xMoO_{3+y} was then used to coat HE-NCM. Dimethyl sulfoxide (DMSO) was used as a solvent in the coating process due to its highly polar nature, allowing lithiated H_xMoO_{3+y} to be dispersed well in the solvent. Lithiated H_xMoO_{3+y} was added in the DMSO solvent, and ultrasonication was used to disperse the particles well. Dried HE-NCM was added in the dispersed solution and the composite was evacuated for a brief amount of time (approximately three minutes) using the Schlenk line to remove any possible remaining air pockets within the HE-NCM secondary particles. After the evacuation step, the mixture was stirred at 200 °C for 3 hours to evaporate the solvent. The precipitated sample was then calcined at 400 °C in air with a ramping and cooling rate of 5 °C per minute and dwelling of 5 hours to remove possible impurities on the coated cathode surface (Figure 3.11).

Figure 3.11 HE-NCM coating procedure

3.3.2 Characterization

To confirm the surface coating of lithiated H_xMoO_{3+y} sheets on HE-NCM, scanning electron microscopy (SEM) was done on the coated and non-coated samples (Figure 3.12). By observing the surface morphology and comparing coated and non-coated samples, the distribution of lithiated H_xMoO_{3+y} nanoparticles were seen on the surface of HE-NCM.

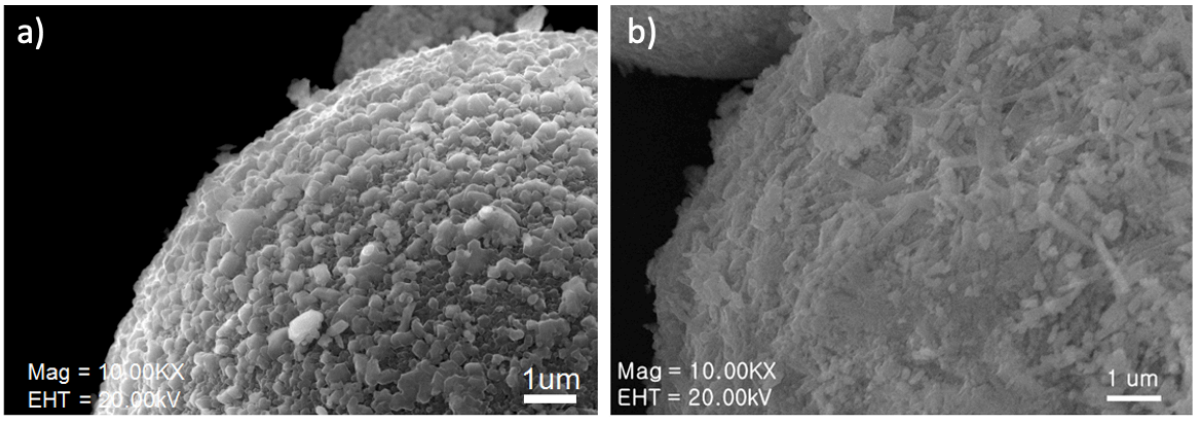

Figure 3.12 SEM of (a) non-coated and (b) coated HE-NCM

Energy Dispersive X-ray Spectroscopy (EDS) was performed on the coated sample to confirm the presence of Mo contents on the surface (Figure 3.13). EDS results showed that Mo was distributed on the surface of HE-NCM. Also, Mo was dispersed quite evenly since the degree of Mo dispersion is similar to the other transition metals like Ni, Co, and Mn.

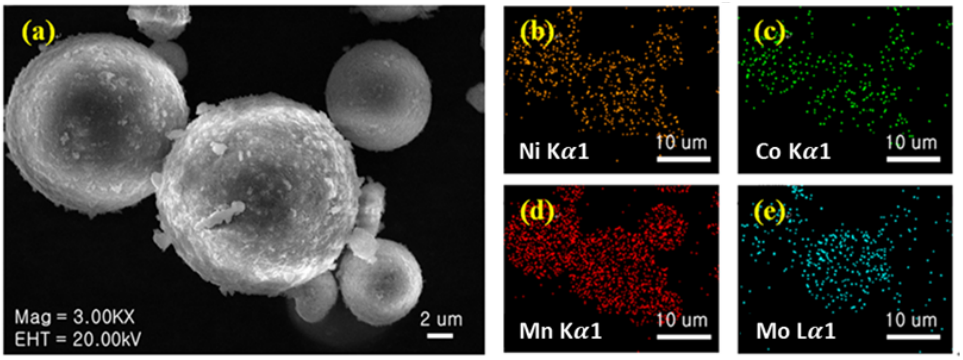

Figure 3.13 SEM (a) and EDS of the coated HE-NCM (b-e)

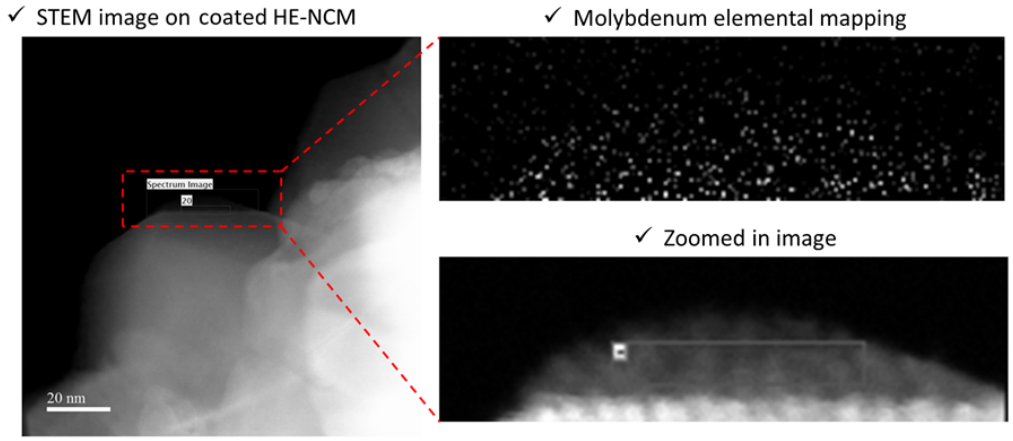

Figure 3.14 STEM of lithiated H_xMoO_{3+y} coated HE-NCM

Scanning transmission electron microscopy (STEM) was performed on the coated sample to further verify the existence of lithiated H_xMoO_{3+y} sheets on the surface of HE-NCM (Figure 3.14). STEM results exhibited that the 6 – 10 nm lithiated H_xMoO_{3+y} were attached on the HE-NCM surface.

XPS was performed on the surface of the coated HE-NCM to elucidate intercalation capability during cell operation (Figure 3.15). Electrodes were made with 92.5 wt% cathode active material, 4 wt% carbon black (Super C65), and 3.5 wt% PVDF binder (Solef 5130). XPS data for the powder form of the exfoliated H_xMoO_{3+y} is listed in Figure 3.15 c. Electrodes made

with the coated cathode with a calcination temperature of 400 °C were analyzed with XPS as the data is represented in Figure 3.15 d. Lastly, Figure 3.15 e shows the data with lithium molybdenum oxide coated HE-NCM that is discharged to 2 V at a C/20 rate after the 1st activation charge up to 4.8 V. The voltage of the cell was on hold at 2 V for 3 hours before being quickly disassembled in an argon-filled glovebox. The H_xMoO_{3+y} XPS data is showing quite clear peaks of Mo $3d_{3/2}$ and an Mo $3d_{5/2}$ doublet at 236.5 eV and 233.4 eV, which is the result of the spin-orbit coupling.[131] The data is in good agreement with reference papers.[131-135] The XPS data of lithium molybdenum oxide coated HE-NCM shows a reduced oxidation state from Mo^{6+}. Chemical lithiation of MoO_3 with LiI may have reduced Mo^{6+} to a lower oxidation state.[124] Also, previous studies revealed that a shifting in Mo 3d and O 1s peaks towards lower binding energy are indications of the presence of oxygen vacancies as the calcination temperature increased from 200 °C to 700 °C.[131] The oxygen-deficient regions can induce a smaller oxygen ion coordination number than before heat treatment. This can ultimately result in reduced Mo – O covalency, which can lead to a shift in Mo 3d and O 1s peaks towards the lower binding energy.[131]

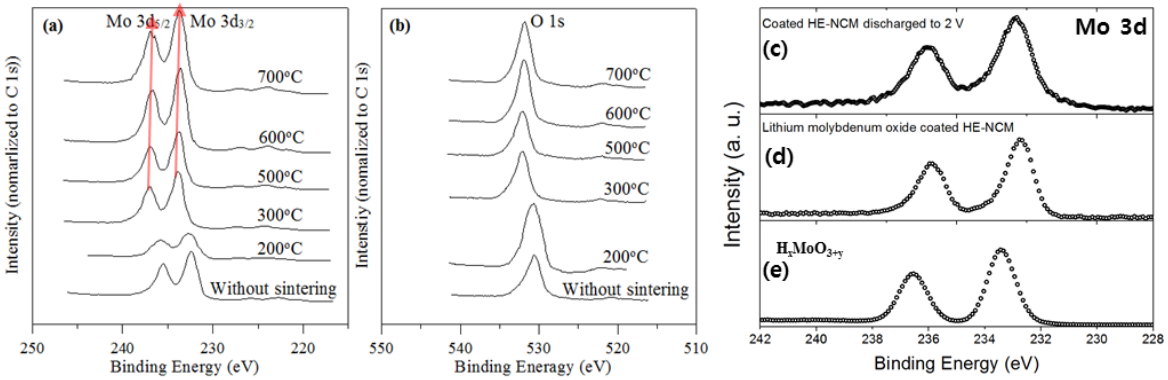

Figure 3.15 XPS data of H_xMoO_{3+y}, lithiated H_xMoO_{3+y} coated HE-NCM and lithiated H_xMoO_{3+y} coated HE-NCM discharged to 2 V.[131] Reproduced with permission from Ref. 131.

The step after lithiated H_xMoO_{3+y} coating involves high-temperature heat treatment. Therefore, a structural study was needed to elucidate the possibility of high-temperature heat treatment affecting the structural property of lithiated H_xMoO_{3+y}. Using a XRD analysis, heat-treated lithiated H_xMoO_{3+y} at 400 °C and 600 °C were analyzed (Figure 3.16). One notable phenomenon was that at 600 °C, most of the heat treated lithiated H_xMoO_{3+y} seemed to be liquefied and recrystallized on the alumina crucible and very few powdered samples were left to conduct a XRD analysis. Also, the color of the heat-treated powder changed from dark blue to pale blue at 400 °C and the color changed to yellow for lithiated H_xMoO_{3+y} powder at 600 °C heat treatment. After a closer look at the diffraction data, a conclusion was made that phase transition occurred from hexagonal lithiated H_xMoO_{3+y} to α-MoO_3 after heat treatment.[124,133,135] Also, the diffraction patterns of heat-treated samples resembled more of

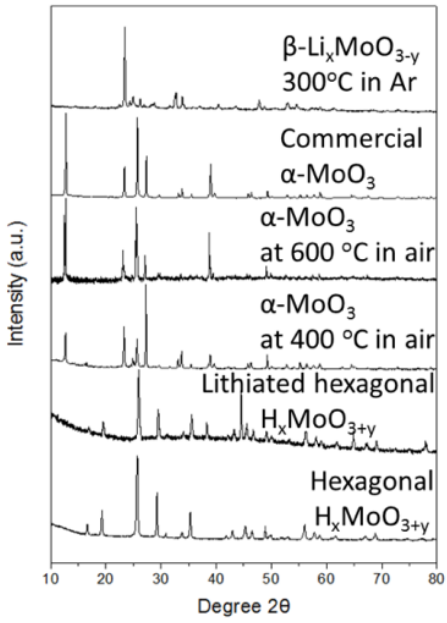

Figure 3.16 XRD results for heat treated lithiated H_xMoO_{3+y} and commercial MoO_3

commercial α-MoO_3. Based on the powder color change, a speculation was made that Li^+ might

have been removed or isolated from the lithiated H_xMoO_{3+y} during heat treatment. An additional experiment was performed to reserve Li^+ in lithiated H_xMoO_{3+y}. To prevent Li isolation from lithiated H_xMoO_{3+y}, the sample was heat-treated at 300 °C under argon atmosphere. XRD was performed on the newly heat-treated sample in argon, and the result of the diffraction analysis exhibited to be β-Li_xMoO_3. The color of the heat-treated sample was also retaining a dark blue color, which can also be an indication that the sample was able to reserve Li in the lattice.

3.3.3 Electrochemistry

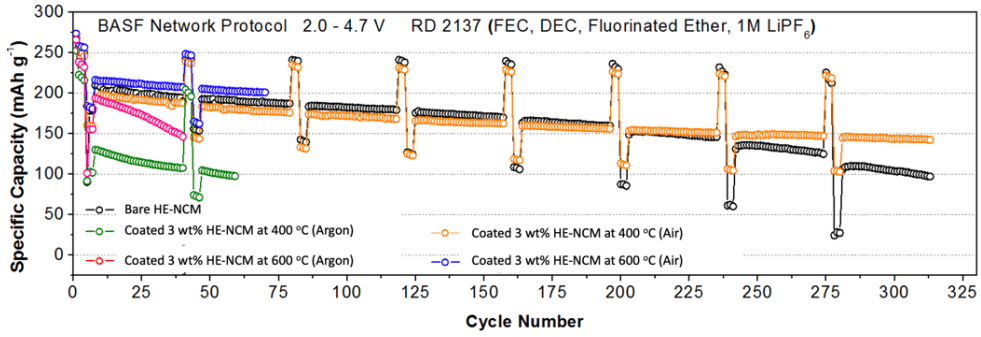

Figure 3.17 Discharge cycle performance data of bare and coated HE-NCM samples

Cell data were gathered using bare and coated HE-NCM at various temperatures (400 °C and 600 °C) in argon and air atmosphere (Figure 3.17). The testing protocol was followed by BASF Network protocol (C/15 x 1ea, 0.1C x 3ea, 0.5C & 3C x 3ea, 0.5C & 1C x 33ea (repeating this steps for 8 times)). Since lithiated H_xMoO_{3+y} retained its Li^+ in H_xMoO_{3+y} when it was heat-treated in an argon atmosphere, the discharge cycle performance of the cells was expected to be better than the coated sample that was heat-treated in air due to the increased electronic conductivity from the lithiated H_xMoO_{3+y}. Contrary to the expected results, lithiated H_xMoO_{3+y} coated HE-NCM that was heat-treated in argon atmosphere exhibited lower

performance versus the cells that were heat-treated in air. A possible explanation might be that the metal oxide in NCM might have been reduced during the heat treatment, which can lead to a minor structural degradation on the surface of HE-NCM, thus yielding lower capacity than the ones heat-treated in air. This is one of the reasons that cathodes are made in an air atmosphere. Lithiated H_xMoO_{3+y} coated HE-NCM without heat-treatment was also tested, but the performance was even worse than the coated HE-NCM that was heat-treated in argon. However, the coated cathode that was heat-treated in air showed good stability as well as high discharge cycle performance throughout the entire cycle.

Symmetric cell electrochemical impedance spectroscopy (EIS) was used to elucidate resistance information from bare and lithiated H_xMoO_{3+y} coated HE-NCM heat treated in air at 400 ºC (Figure 3.18). The electrodes were cut in half and used them as working and counter electrodes. Please note that there can be potential issues of using the symmetric cell configuration such as possible cathode electrolyte interface breakage during cell disassembly for EIS measurement after cycling, a misalignment of cathodes during the symmetric cell fabrication and etc. Despite the abovementioned disadvantages, the symmetric EIS analysis is a powerful technique to analyze the cathode impedance by eliminating the resistance attributed from lithium metal degradation during cycling. The EIS was performed on each cell before cycling and after the completion of the loop cycle. Ten hours of OCV period was given before conducting EIS to ease out any overpotential remaining in the cell. The EIS data before the cell cycle showed one semi-circle for each cell. This semi-circle is attributed to the charge transfer resistance of the cell. The surface film resistance was absent since the data was gathered before battery cycling. The EIS data after the battery cycling exhibited a dramatic difference between the bare and coated HE-NCM. The surface film and charge

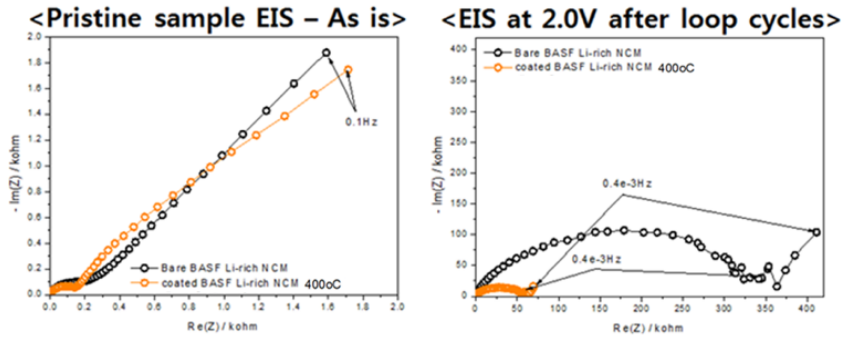

Figure 3.18 Symmetric EIS data of bare and heat treated coated HE-NCM

transfer resistance are included in the semi-circle. Although the overlap of the two semi-circles attributed to surface film and charge transfer resistance made it difficult to decouple different resistance factors, the data certainly displayed significantly lower cell resistance versus the bare HE-NCM.

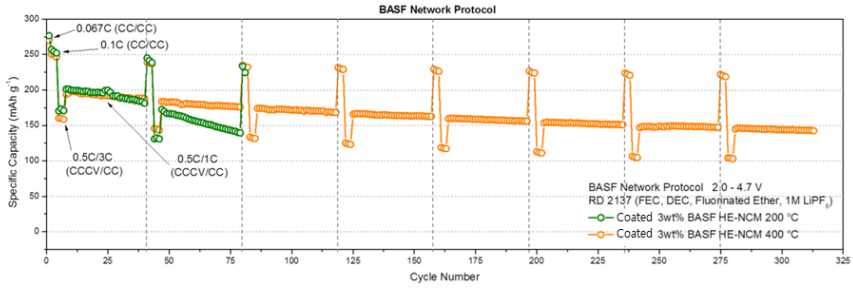

Figure 3.19 Discharge cycle performance data of dried and heat treated coated HE-NCM

Since a possible metal reduction during heat treatment in argon atmosphere may have disrupted the cycle performance, discharge cycle performance from a dried (200 °C in air) lithiated H_xMoO_{3+y} 3wt % coated HE-NCM was needed as a simple drying process at 200 °C in air may eliminate the metal reduction problem. For that reason, cell data was gathered for dried (200 °C in air) and heat-treated (400 °C in air) lithiated H_xMoO_{3+y} 3wt % coated HE-NCM to determine whether variable electrical conductivity of lithiated H_xMoO_{3+y} by

extraction/insertion of Li^+ in H_xMoO_{3+y} is beneficial towards cycle performance (Figure 3.19). The temperature of 200 °C in air was chosen for the purpose of removing possible solvent residue (boiling point of DMSO is 189 °C).[136] The cycle results revealed that the dried sample was showing inferior cycle performance versus the heat-treated coated sample in the air atmosphere at 400 °C. Although the reason for the inferior cycle result from the coated sample dried at 200 °C in air is unclear, a possible reason for the cycle result could be related to the reactivity of H_xMoO_{3+y} with HE-NCM during high temperature (400 °C) heat treatment in air. It could be that H_xMoO_{3+y} reacted with the HE-NCM surface by Mo^{6+} diffusion on the surface of HE-NCM. Since one of the major contributions of capacity fading is from the structural instability due to cathode lattice oxygen loss, perhaps surface diffusion of Mo^{6+} may provide higher structural stability. Further proof of this claim will be stated in detail in the next chapter. Based on the cycle performance data, the results provided a hint that the heat treatment is somehow beneficial towards the cycle stability. Thus, in-depth analyses on the heat-treated samples were needed to understand the origin of cycle stability.

The cycle performances of the bare and coated HE-NCM heat-treated in air at 400 °C were further scrutinized by analyzing voltage profiles and their differential capacity plots.

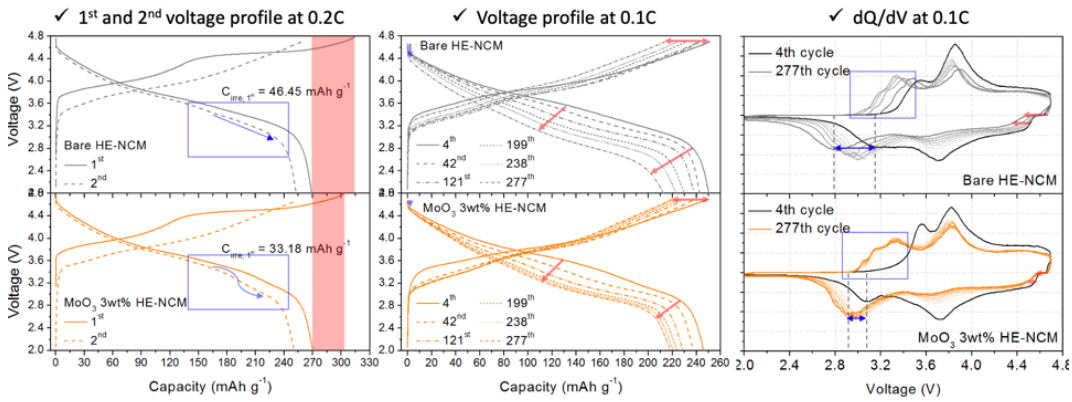

Figure 3.20 Voltage profiles and dQ/dV plots from bare and coated HE-NCM cells using

lithium metal as an anode

The left graphs in Figure 3.20 are the 1st and 2nd cycle voltage profile of the bare and the coated cells. The difference between charge and discharge capacity is the value for irreversible capacity (C_{irre}). Irreversible capacity should be monitored since it is the result of the inability of Li^+ to be intercalated back to the cathode after the first charge.[137-139] Usually, high C_{irre} caused by elongation of the charge profile at above 4.4 V can be interpreted as the cathode experiencing either undesirable EC oxidation or cathode lattice oxygen release. The other case for high C_{irre} is caused by early stage (below 4.4 V) elongation of the charge profile due to decomposition of residual lithium compounds such as Li_2CO_3 and LiOH.[140] If the high C_{irre} is determined by low discharge capacity, this can be interpreted as an inability of the anode to discharge Li^+ or inability of the cathode to receive Li^+ from the anode.[137, 141] The inability of the cathode may be the result of problems with its bulk structure, or there may be problems with the cathode interface preventing Li^+ to be intercalated, thus yielding low discharge capacity. Looking at the voltage profile data from the bare and the coated samples, higher C_{irre} was observed for the bare sample, and this C_{irre} was induced by elongation of an early stage charge voltage profile. No profile elongation on the discharge profile was observed except for the blue boxed region which indicates an additional voltage plateau for the coated samples. The absence of profile elongation can be an indication that the cathode bulk structure for bare and coated cells does not have any problem of receiving Li^+. Also, Li metal was used for the anode and the profile that is being examined is from the first cycle. Therefore, the problem related to Li metal degradation can be neglected. Based on the charge and discharge voltage profiles of bare and coated cells, a conclusion was made that the higher C_{irre} may have been attributed to the excess residual lithium that had been placed on the surface of HE-NCM. The amount of the residual lithium contents from the coated cathode is low because the coating process involves

solvent evaporation. The DMSO used in the coating process may have removed excess residual lithium on the bare HE-NCM.

The discharge voltage profiles were closely examined. The plateau in the voltage profile can be interpreted as the phase transition associated with changes in the lattice parameter of the active material. For the coated cells, an additional voltage plateau was observed at approximately 3.1 V from the 1st cycle. No such plateau was identified for the bare samples. This phase transition is closely related to spinel-like phase Mn reduction, and the plateau was continuously developed until the 120th cycle for the coated samples. The plateau seemed to be stabilized for the coated cells after the 120th cycle. However, the bare samples experienced continuous growth of the Mn reduction plateau without an indication of stabilization. Also, the bare cell experienced continuous severe voltage drop throughout the discharge.

The Mn reduction plateau growth is more observable in a differential capacity (dQ/dV) plot. The differential capacity plot is the first-order differentiation of the capacity with respect to voltage, which gives information on the phase transition as well as the capacity exhibited from the cathode.[142-144] The location of a peak in a dQ/dV plot provides the voltage where phase transition occurs, which is associated with expansion/shrinkage of the lattice parameters during charging or discharging. The area of the peak can be interpreted as the capacity exhibited at the coordinating voltage. Coupled with in-situ XRD data, previous studies have revealed detailed redox processes occurring in HE-NCM.

There are three regions associated with a HE-NCM dQ/dV plot.[37,145,146] Region I in Figure 3.21 is associated with Mn and oxide ion redox. There are different kinds of Mn redox

behavior in region I. The reduction peak at a lower voltage (below ~ 2.8 V) is associated with spinel phase Mn reduction. A value of 3.0 V is assigned to the combination of oxygen redox and spinel-like phase Mn reduction, where the spinel-like phase is defined to be the incompletion of transition metal ion migration from the 3b sites of the octahedral site ($(Li)_{3a}[TM]_{3b}O_2$) of the TM slabs into the Li slab of 3a octahedral site to become an ideal cubic spinel phase $(Li)_{8a}[TM_2]_{16d}O_4$.[147,148] Region II is related to layered Ni and Co reduction at 3.7 V. Finally, region III is associated with oxygen reduction.[37,38,41,43,146] Corresponding oxidation peaks are also listed in each region in Figure 3.21.

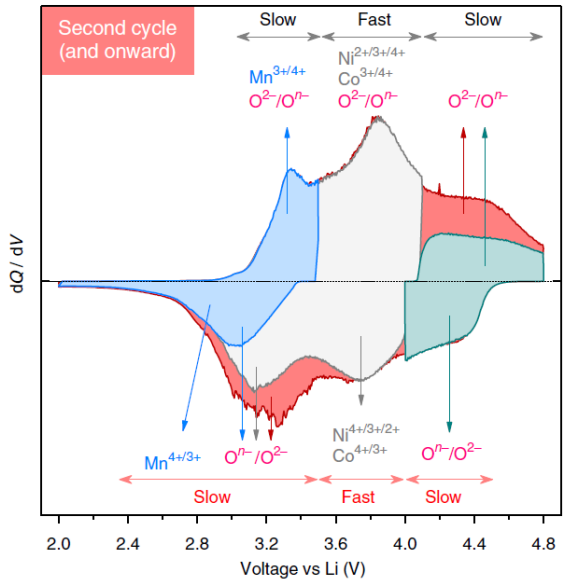

Figure 3.21 A typical differential capacity (dQ/dV) plot for HE-NCM.[37,145] Reproduced with permission from Ref. 37. Copyright 2017 from Springer Nature.

The Mn reduction peak in the bare HE-NCM dQ/dV plot displayed a continuous shift from 3.1 V to 2.8 V. This shift in the Mn reduction peak is an indication of gradual structural degradation from layered to spinel phase. However, the coated HE-NCM heat treated at 400 °C showed remarkable structural stabilization in addition to the evolution of a small Mn reduction

peak shift at first discharge. The trend of the Mn oxidation peak growth is also a bit different between the bare and coated samples. For bare cells, the Mn oxidation peak at approximately 3.1 V was shifted to a lower voltage during the beginning stage of the cycle. However, this Mn oxidation peak suddenly shifted back to a higher potential at approximatwly 3.3V, with a slight decrease in peak height (blue square region). The coated HE-NCM developed its Mn oxidation peaks at 3.2 V, and no shift like the bare cell's data occurred for the coated sample. Also, the area corresponding to this oxidation peak at 3.2 V became more prominent after consecutive cycles for the coated sample. Based on the differential capacity plots from the bare and the coated cells, a conclusion was made that the phase transition from layered to spinel phase was stabilized by having a heat-treated lithiated H_xMoO_{3+y} coating. One unusual characteristic from the dQ/dV plot of heat-treated coated cells is that the samples were showing a distinct oxidation and reduction peak at approximately 3.55 V and 3.1 V, respectively, from the 1st cycle. This

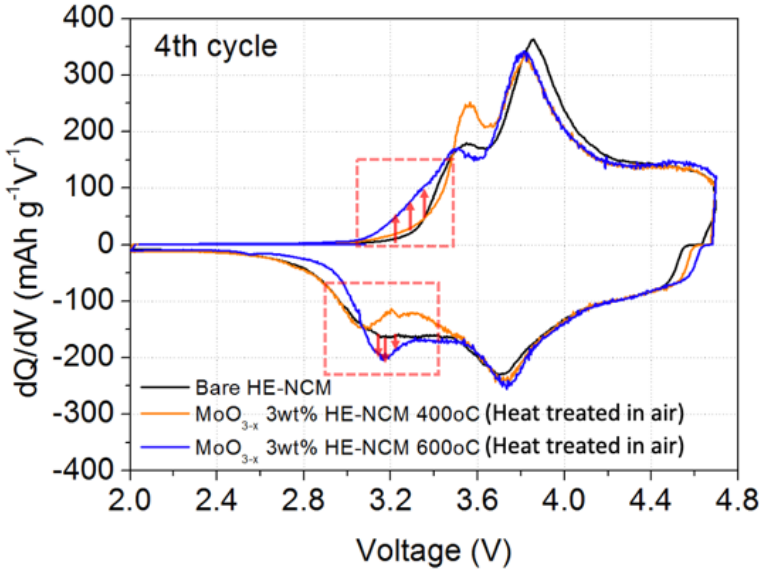

Figure 3.22 Differential capacity plot from bare and lithiated H_xMoO_{3+y} coated HE-NCM at various calcination temperatures

oxidation and reduction peak at the first cycle is absent for the bare sample. This distinct peak was then developed to become an oxidation and reduction peak for oxygen and the spinel-like Mn redox region over consecutive charge-discharge cycles. These grown oxygen and spinel-like Mn redox peaks were shifted a miniscule amount during cycles with respect to the oxygen and spinel-like Mn redox peak shift from the bare cells, To further investigate the growth of the abovementioned redox peaks in detail, 4th cycle differential capacity profiles were plotted using bare HE-NCM, lithiated H_xMoO_{3+y} 3 wt% coated HE-NCM at 400 °C and 600 °C (Figure 3.22). The results showed that the initial redox peaks observed for the coated cells at approximately 3.55 V and 3.1 V were observed for only the heat-treated coated cells (400 °C and 600 °C). It also seemed like the development of these redox peaks at 3.55 V and 3.1 V is proportional to the degree of heat treatment since the coated sample with 600 °C heat treatment displayed more distinct redox peaks at 3.55 V and 3.1 V. The bare HE-NCM was washed with DMSO and then heat-treated at 600 °C to identify whether this Mn reduction peak is an effect of heat treatment. It turned out that DMSO washed bare HE-NCM did not show distinct peak evolution at 3 V. Based on the 4th cycle differential capacity data, a speculation was made that a reaction occurred between the lithiated H_xMoO_{3+y} and HE-NCM surface. Because of this reaction, HE-NCM lattice oxygen may have escaped. The oxygen vacancies can induce metal migration to the lithium slab due to the underbonded metal in the octahedral site making it easier to migrate to the lithium site. According to Li et al., MoO_3 has an interesting property of extracting lithium-ions from the bulk lithium source such as cathodes.[149] Studies have been reported that MoO_3 can be used to leach out Li+ from lithium-rich NCM under high-temperature calcination (above 525 °C) by utilizing the following reaction in Equation 3.2:

$$Li_{1+X_{rich}}M_{1-X_{rich}}O_2 + \beta MoO_3 \rightarrow Li_{1+X_{rich}-2\beta}M_{1-X_{rich}}O_{2-2\beta} + \beta Li_2MoO_4 + \frac{\beta}{2}O_2(\uparrow)$$

Equation 3.2 Lithium leaching reaction by MoO_3 [149]

According to Li et al., MoO_3 can react with lithium-rich NCM to extract Li^+ as well as an oxygen extraction from the surface region (within 10 nm) of lithium-rich NCM at above 525 °C.[149] As a result, the formation of a liquid layer of MoO_3 - Li_2O eutectic liquid solution was possible. The study also claimed that the created liquid solution can be cooled to become a crystallized *R-3* Li_2MoO_4 coating on lithium-rich NCM. This study can be correlated to the heat treatment results of this thesis study because lithiated H_xMoO_{3+y} melting was observed for samples with heat treatment temperatures above 600 °C. Therefore, a hypothesis was made that the formation of a liquid layer of MoO_3 - Li_2O eutectic liquid solution was made with a lithiated H_xMoO_{3+y} coating, and the liquid layer was cooled to room temperature to obtain the Li_2MoO_4 coating.

There are many advantages from using Li_2MoO_4 as a cathode coating. It is an excellent lithium-ion conductor due to its 3-dimensional structure linked by MoO_4 tetrahedron and corner-shared LiO_4 (Figure 3.23).[150-154] Also, the insulating property of Li_2MoO_4 (10^{-11} S cm^{-1} at 433 K) can effectively prevent electron transfer from EC to the cathode at high voltage if Li_2MoO_4 is used as a coating material.[150-154]

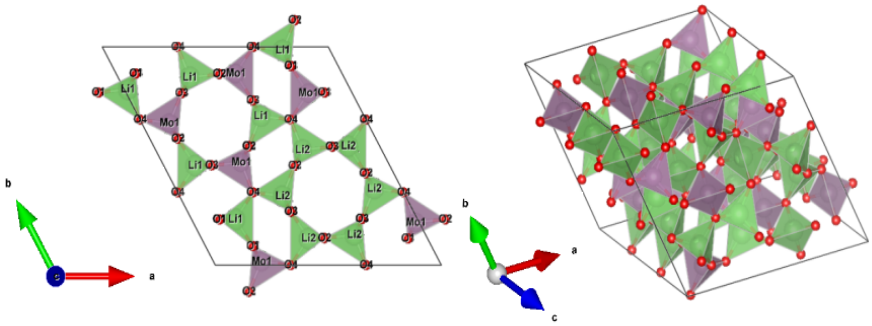

Figure 3.23 Crystal structure of *R-3* Li_2MoO_4 [155]

The other advantage that needs to be mentioned is related to Mo surface diffusion on HE-NCM. The Mo^{6+} from Li_2MoO_4 can be diffused on the surface region of the HE-NCM during high-temperature calcination, and the subsequent establishment of a Mo contained HE-NCM sub-surface is possible. According to Tamman's rule, a mixture of the two reactants can be achieved when the sintering temperature is two-thirds of the melting point of lower melting components.[156,157] Between MoO_3 and HE-NCM, the limiting melting point reagent is MoO_3 since its melting point is 795 °C, whereas the typical melting point of a LIB cathode is above 1000 °C.[149] Also, the size of the H_xMoO_{3+y} is nanoscale and the effect from the particle size will lower the melting point of H_xMoO_{3+y}. Coupled with Li leaching from MoO_3 which can induce lithium site vacancies in the lithium slabs and possibly also in Li site vacancies in the honeycomb arranged transition metal slabs, some of Mo from MoO_3 may be easily diffused in those vacancies during high-temperature heat treatment. The metal cation diffusion in NCM's lithium site during high temperature heat treatment is a well-known phenomenon according to previous studies.[158-160] Also, there is a possibility that during Li extraction by MoO_3, some of the transition metals from the 3b sites of transition metal slabs might have been migrated to the 3a sites of lithium vacancies, according to Li et al,.[149] The metal vacancies created by either metal migration from 3b sites to 3a lithium sites or 3a sites Li vacancies created by Li^+ extraction from MoO_3 then may be partially filled with diffused Mo since the ionic radius of Mn^{4+} (53 pm), Co^{3+} (54.5 pm) and Ni^{2+} (69 pm) from $LiTMO_2$ and Mo^{6+} (59 pm) from MoO_3 are very similar to each other.[161] Just as the Li_2SnO_3 coating establishes Sn^{4+} doping (ionic radius of 69 pm) and spinel-like phase on Li-rich NCM after 900 °C heat treatment, Mo diffusion in lithium sites and/or a portion of TM migration during the lithium extraction process may have occurred and have established a spinel-like phase on the surface of HE-NCM.[157,161]

This may be the reason for having a small spinel-like phase peak during the first discharge dQ/dV profile. Compared to the HE-NCM without diffused Mo on the surface, the Mo surface diffused HE-NCM can provide improved cycle stabilization due to the high dissociation energy of the Mo – O (Figure 3.24). Compared to other transition metals with O, namely Co – O (397.4 kJ mol^{-1}), Ni – O (366 kJ mol^{-1}), and Mn – O (362 kJ mol^{-1}), Mo – O has a higher dissociation energy of 502 kJ mol^{-1}.[162] Because of such high dissociation energy, the Mo ion diffusion into the HE-NCM surface may retain lattice oxygen by stabilizing the structure against phase transformation during long-term cycling. The effective prevention of oxygen release can result in maintaining reversible oxygen redox capability as well.

$$D^{o}_{298}(\mathrm{A{-}B}) \approx D^{o}(\mathrm{A{-}B}) + (3/2)RT = D^{o}(\mathrm{A{-}B}) + 3.7181\ \mathrm{kJ\ mol^{-1}}$$

A–B	D^{o}_{298}/kJ mol^{-1}
Ni–O	366 ± 30
Mn–O	362 ± 25
Co–O	397.4 ± 8.7
Mo–O	502

Figure 3.24 Bond dissociation energies of Ni, Mn, Co and Mo with O at 298K.[162]

Reproduced with permission from Taylor & Francis Group.

Based on the data from the previous studies by Li et al., a speculation was made for this thesis study that lithiated H_xMoO_{3+y} may have been melted on the HE-NCM surface and extracted lithium-ions from the cathode to form a Li_2MoO_4 coating.[149] If the speculation turned out to be an accurate claim, then better dispersion of the exfoliated nano H_xMoO_{3+y} is needed to maximize the coverage of Li_2MoO_4 on the HE-NCM surface to increase the distribution of Mo diffusion on the cathode surface upon heat treatment. Thus, a slight modification was done on the coating method.

3.4 Li-Mo-O Coated High Energy Lithium Layered Oxide

3.4.1 Synthesis

The modified coating method is stated in this section. The exfoliation steps using molybdic acid and octylamine are the same as before (Figure 3.25).[129] After exfoliation, the synthesized H_xMoO_{3+y} was then inserted in the DMSO solution. To better distribute Mo diffusion on the entire HE-NCM surface, 3 wt% H_xMoO_{3+y} powder was well-dispersed in DMSO using ultrasonication (20 kHz, 750 W) with 50 % power irradiation intensity for 3 minutes. After the dispersion, a small amount of LiOH (0.1 wt%) was added and sonicated using the same sonication condition stated above. The initial purpose of LiOH addition in the solution was to create lithium-ion intercalated molybdenum oxide during high-temperature calcination. However, a series of experiments proved that this is an unnecessary step as H_xMoO_{3+y} with HE-NCM alone can yield Li_2MoO_4 and this will be discussed in detail in Figure 3.28. After the sonication, bare HE-NCM was added in the H_xMoO_{3+y} and LiOH solution and evacuated using the Schlenk line for 1 minute to remove possibly trapped gas within the pores of HE-NCM. After the evacuation step, the sample was stirred at a constant temperature of 200 °C to evaporate DMSO. The precipitated sample was then carefully collected and heat-treated in air atmosphere with a ramping and cooling rate of 5 °C per minute and a dwelling duration of 5 hours.

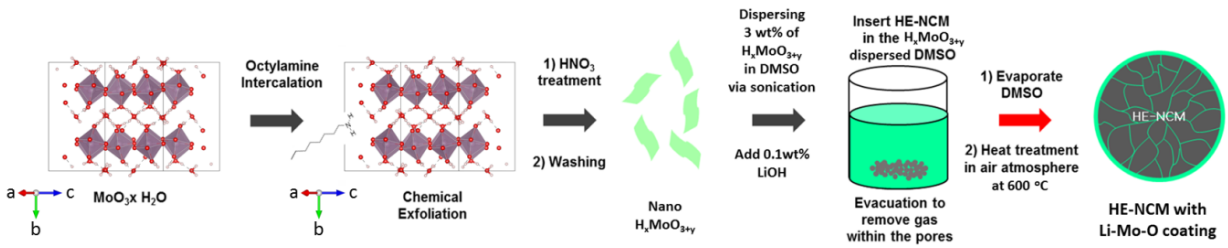

Figure 3.25 Li-Mo-O coated HE-NCM synthesis procedure

3.5 Results and Discussion

3.5.1 Characterization

The presence of Mo and O on the surface of the coated HE-NCM was verified using SEM, EDS and HR-TEM (Figure 3.26). The SEM data show no difference in morphology between bare and 3 wt% Li-Mo-O coated HE-NCM. The EDS data showed Mo signals that are evenly distributed to the entire HE-NCM secondary particles. The dispersion of the Mo signal is very similar to the rest of the transition metal, such as Ni, Co, and Mn. Considering Li_2MnO_3 and $Li(TM)O_2$ are mixed in solid solution manner, the similar signal distribution of Mo can be interpreted as an indication of well-dispersed Li-Mo-O constituents over the surface of HE-NCM. The HR-TEM data also confirmed the presence of Li-Mo-O coating with a thickness of 8 - 10 nm. Note that some of the HE-NCM surface were covered with an island coating.

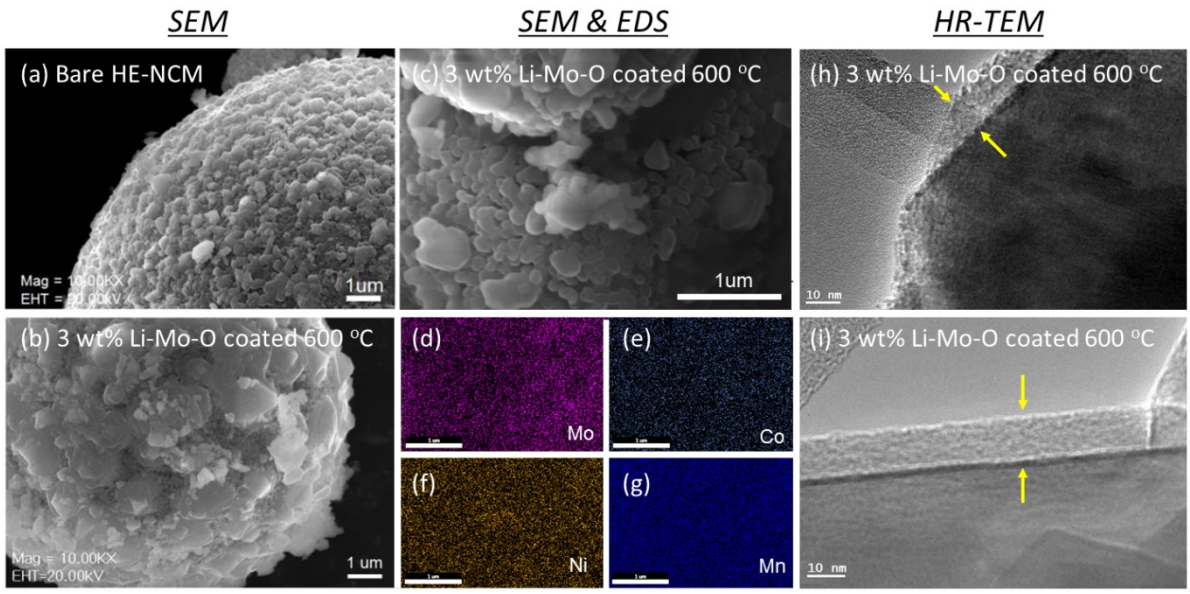

Figure 3.26 SEM, EDS and HR-TEM data of bare and 3 wt% Li-Mo-O coated HE-NCM

A XRD study was performed on the molybdenum oxide as well as the coated sample

to gain structural information on the coated material. For the molybdenum oxide structural study, exfoliated hexagonal H_xMoO_{3+y} and LiOH were well-dispersed in DMSO using ultrasonication and the solvent was evaporated to gather structural information immediately after solvent evaporation (Figure 3.27).

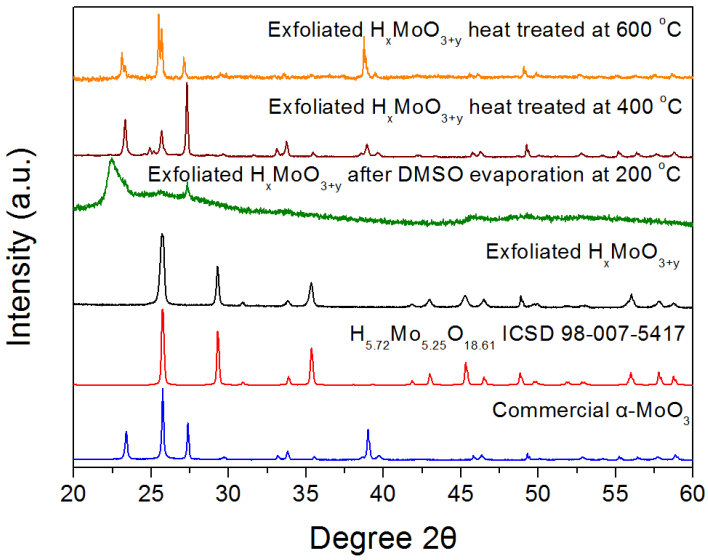

Figure 3.27 XRD data of H_xMoO_{3+y} at different calcination temperatures

The XRD data after solvent evaporation revealed a somewhat noisy and broad peak shape. This widened peak shape is possibly an indication of nano-sized particles or could be related to H_xMoO_{3+y} became amorphized due to the ultrasonication breaking down the crystalline structure. As the heat treatment temperature increased, the shape of the peak became sharper. This can be an indication of the increased crystallinity of the particles. After comparing it with XRD reference data, the heat-treated H_xMoO_{3+y} became an α-MoO_3.

The heat treated coated HE-NCM was also analyzed using XRD. However, the small amount of coating (3 wt%) was not enough to show a difference in XRD data compared to the bare HE-NCM due to the detection limit of diffractometer. Therefore, the coating weight

percentages were increased from 3 wt% up to 30 wt% as well as the content of LiOH from 0.1 wt% up to 1 wt%. XRD was then performed to see the structural change from the coated sample after heat treatment (Figure 3.28). For a 30 wt% coating, XRD data revealed patterns which correspond to $R\bar{3}$ Li_2MoO_4, $R\bar{3}m$ from NCM, *C2/m* related superstructure from Li_2MnO_3 and $Fd\bar{3}m$ spinel phase of $LiNi_{0.5}Mn_{1.5}O_4$. The XRD data of Li_2MoO_4 was an interesting result because α-MoO_3 was obtained when H_xMoO_{3+y} was heat treated alone in air at 600 °C. This result can also be an indication that H_xMoO_{3+y} reacted with the HE-NCM surface to form Li_2MoO_4. Although the structural information for 3 wt% coating is difficult to identify from XRD, a conclusion was made that the coating is composed of Li, Mo and O based on EDS analysis and Li and possibly O extraction reactions by H_xMoO_{3+y}. A rational speculation can be made based on the 30 wt% coating XRD data that the 3 wt% coating may or may not be Li_2MoO_4 and determining the exact composition requires further advanced X-ray studies such as Extended X-ray Absorption Fine Structure analysis to estimate the local structural parameters (e.g. interatomic distances for Mo–O bonds) of the coated HE-NCM. Due to such reasons, the 3 wt% coating is stated to be a Li-Mo-O coating.

H_xMoO_{3+y} 30 wt% coated HE-NCM was heat treated at various temperatures to find the origin of Li_2MoO_4 in detail (Figure 3.28). The peaks corresponding to Li_2MoO_4 were not identified immediately after the solvent evaporation (200 °C). This could be due to the nano-sized particles of the exfoliated hexagonal H_xMoO_{3+y} or the insufficient thermal energy to initiate Li and O extraction reaction by H_xMoO_{3+y}. As the temperature increased, peaks from Li_2MoO_4 were spotted beginning at 400 °C. This can be the result of the extraction reaction of Li and O induced from molybdenum oxide to form Li_2MoO_4 (equation 3.2).

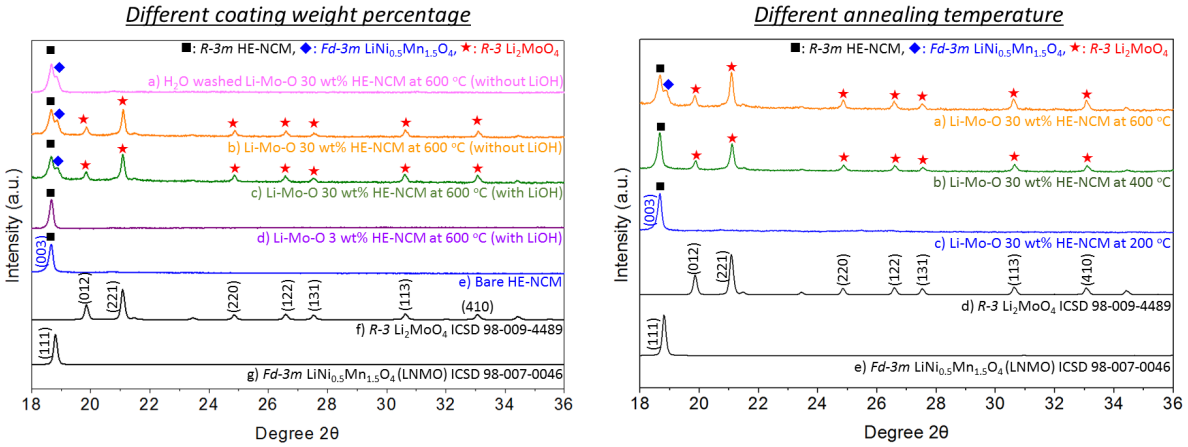

Figure 3.28 XRD data of various Li-Mo-O coating loading and different calcination temperature of the coated HE-NCM

Recent studies from Bruce et al. revealed a relationship between the ordering of the Li_2MnO_3 superstructure and reversible oxygen redox capability.[49,50,52] Coupled with various spectroscopic tools, studies mentioned that the origin of voltage drop at high potential (voltage hysteresis) is related to the Li_2MnO_3 structure disorder. Since lithium ions return to the vacancy clusters created from in-plane Mn migration, the interaction between the returned Li and O is weak.[50] This leads to a high energy state of O 2p and ultimately induces voltage drop. One way to mitigate this voltage drop at high potential is related to having a different Li_2MnO_3 superstructure. Reducing lithium contents in the superstructure by substitution of lithium with Mn can lead to having a denser ordering of transition metal. This modified Mn ordering was able to retain the original crystal structure while exhibiting reversible oxygen ion redox. This structural modification significantly reduced the formation of molecular oxygen during charge and ultimately prevented voltage drop during discharge.[50, 52]

A speculation was made for Li-Mo-O coated HE-NCM that the surface diffused Mo might have occupied vacant lithium sites in the Li_2MnO_3 superstructure. By MoO_3 lithium

extraction from the lithium-ions in the honeycomb structure, Mo from MoO_3 might have been diffused during high-temperature calcination. Based on the 30 wt% coating XRD data, all of the new peaks in the region of the superstructure peaks were from Li_2MoO_4, and no new peaks were identified. Therefore, Mo may not have occupied Li vacant sites in the Li_2MnO_3 superstructure during high-temperature heat treatment.

One notable trend from XRD data is the evidence of spinel formation at above specific heat treatment temperatures. For 600 °C, (111), (011), (222), (400), and (331) are the XRD peaks that corresponds to a disordered spinel $LiNi_{0.5}Mn_{1.5}O_4$ (LNMO).[91,157,163-168] The HighScore Plus analysis program was used to analyze the XRD data and the data confirmed the corresponding peaks for the 600 °C sample to be related to the LNMO. The lithium extraction by MoO_3 can possibly induce oxygen vacancies on the HE-NCM surface according to Equation 3.2. As the O extraction reaction progresses with the temperature increase, the oxygen vacancies on the HE-NCM surface can also increase. These possible oxygen vacancies induced by lithium extraction reactions can establish underbonded TM with reduced coordination number. The underbonding of TM ultimately promotes metal migration to the lithium site (TM migration from the 3b sites of an octahedral site ($(Li)_{3a}[TM]_{3b}O_2$) of the TM slabs into the Li slab of 3a octahedral site) to establish a spinel-like phase. The amount of MoO_3 coating is proportional to the amount of Li^+ and O extraction. For example, a 30 wt% H_xMoO_{3+y} coating on HE-NCM has a larger amount of Li^+ and O extraction when heat treated at 600 °C in air then a 3 wt% H_xMoO_{3+y} coating when heat treated at 600 °C in air. This is why LNMO was detected more notably than 3 wt% of Li-Mo-O coated HE-NCM. The lower amount (3 wt%) of H_xMoO_{3+y} coating may have extracted less Li^+ and O and formed a smaller amount of LNMO than the 30 wt% Li-Mo-O coating .

To find out whether the spinel phase can be established just by adding LiOH and heat treating with no presence of H_xMoO_{3+y}, XRD data was gathered from the HE-NCM with 1 wt% LiOH added (the equivalent amount of LiOH that was used for the 30 wt% Li-Mo-O coating). The addition of LiOH followed the same coating procedures that were used for the 30 wt% Li-Mo-O coating on HE-NCM except for the addition of H_xMoO_{3+y} in DMSO. Compared to the bare HE-NCM, the XRD data displayed no change in peaks upon various heat treatment temperatures (Figure 3.29).

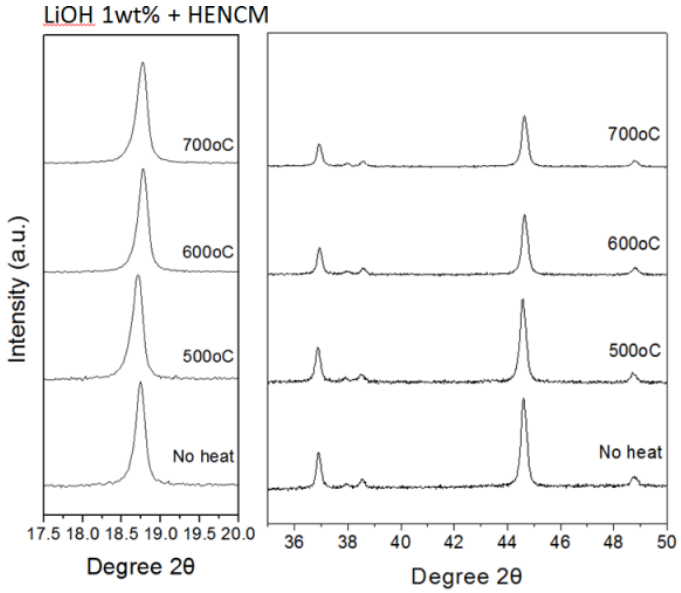

Figure 3.29 XRD data of LiOH 1 wt% addition to HE-NCM at different heat treatment temperatures

Thus, the conclusion was made that the spinel formation is not from the addition of LiOH. To better find the origin of the spinel phase, a 30 wt% Li-Mo-O coating was washed with water and then XRD was performed (Figure 3.30). Since Li_2MoO_4 is very soluble in water, the coated HE-NCM was washed with DI water for 1 hour and then vacuum dried over night to perform XRD. The water washed sample did not show any peaks related to Li_2MoO_4 while peaks related to LNMO were still identified. Therefore, the spinel phase was not established in

the coating, but was established on HE-NCM and the LNMO was induced by the Li-Mo-O coating upon heat treatment by equation 3.2.

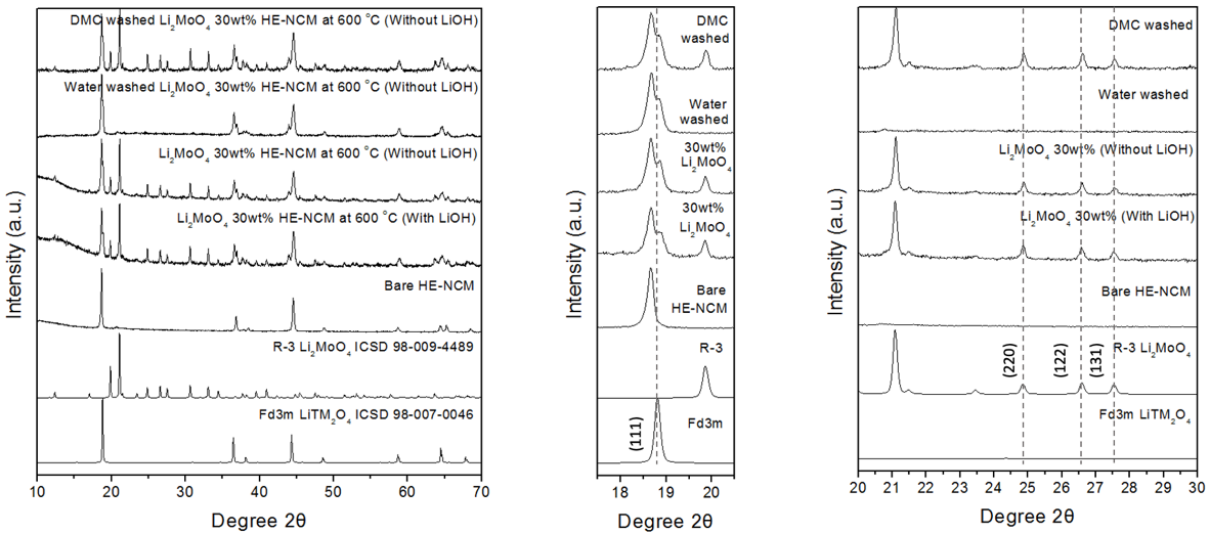

Figure 3.30 XRD data of bare HE-NCM, 30 wt% Li-Mo-O coated HE-NCM, 1 wt% LiOH addition on HE-NCM, water and DMC washed 30 wt% Li-Mo-O coated HE-NCM at 600 °C calcination temperature

Since Li_2MoO_4 is very soluble in water, questions arose as to whether Li_2MoO_4 was soluble in organic solvent as well (Figure 3.30). Thus, DMC was used to wash 30 wt% Li_2MoO_4 coated HE-NCM for 1 hour and then XRD was performed. The peaks corresponding to Li_2MoO_4 showed the sample being unwashed and the peaks from $LiNi_{0.5}Mn_{1.5}O_4$ were also identified. This result revealed that the Li_2MoO_4 coating was not soluble in DMC. An additional experiment was done to re-confirm whether Li_2MoO_4 is soluble in organic electrolyte. 10 mg of commercial Li_2MoO_4 from Sigma Aldrich was added in a vial filled with 5 ml LP57 electrolyte (EC:EMC = 3:7, 1M $LiPF_6$). The solution was constantly stirred with a stir bar for 18 hours and observed whether Li_2MoO_4 was dissolved in the electrolyte. Figure 3.31 confirms that Li_2MoO_4 is not soluble in a typical organic electrolyte as the added Li_2MoO_4

was still observed after the stir.

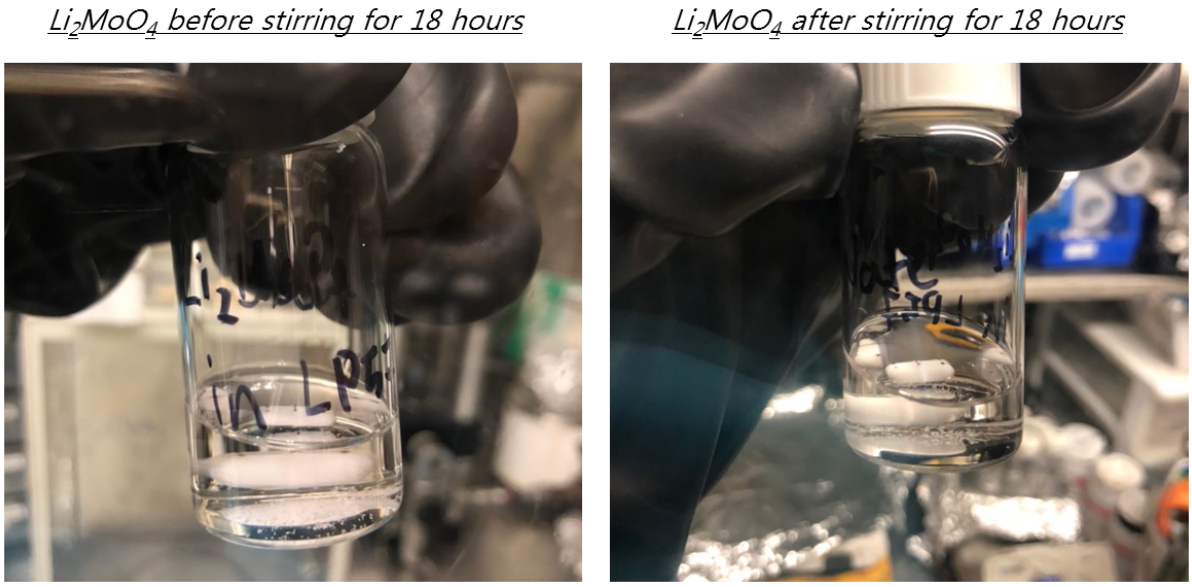

Figure 3.31 Li_2MoO_4 solubility test in a commercial organic electrolyte

Raman spectroscopy was also used to further prove the evolution of the spinel phase established from the coated HE-NCM during heat treatment at 600 °C (Figure 3.31). Various coating loadings from 3 to 30 wt% were applied to observe the modified structural information induced by the Li-Mo-O coating. As expected, bare HE-NCM had peaks corresponding to approximately 590 and 480 cm^{-1}, which are attributed to A_{1g} and E_g mode from $LiTMO_2$ and approximately 562 and 425 cm^{-1} which corrspond to A_g and B_g mode from

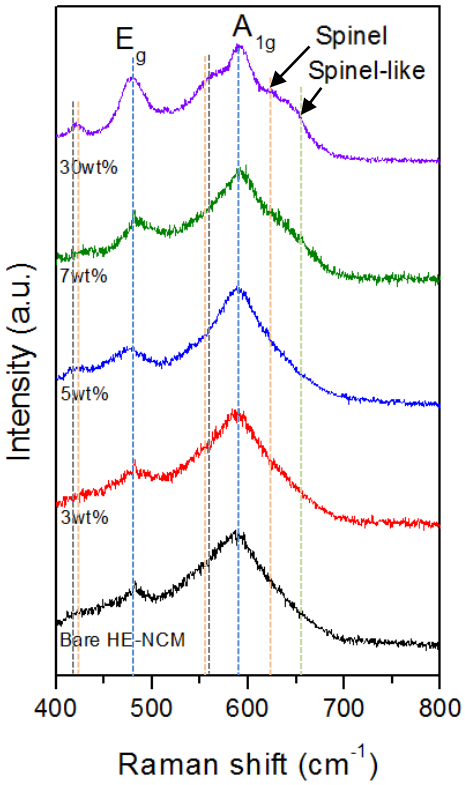

Raman shift	Assignment	Correspondence
~664 cm^{-1}	T2g, shorter Mn – O due to oxygen displacement	Spinel-like
~ 625 cm^{-1}	A1g, Mn^{3+} – O	$LiMn_2O_4$
~ 590 cm^{-1}	A1g, out of plane M-O stretch	$LiMO_2$
~ 562 cm^{-1}	Bg, Ag	Li_2MnO_3
~ 560 cm^{-1}	A1g, Mn^{4+} – O	$LiMn_2O_4$
~ 480 cm^{-1}	Eg, in plane O-M-O bend	$LiMO_2$
~ 430 cm^{-1}	Eg, mixed valence state of $Mn^{3.5+}$ – O	$LiMn_2O_4$
~ 425 cm^{-1}	Bg, Ag	Li_2MnO_3

Figure 3.32 Raman data of bare and coated HE-NCM with various coating loading [169-171]

Li_2MnO_3.[169] The peak trend from 3 to 5 wt % coating was comparable to bare HE-NCM. This is due to the resolution limit of the laser used. The wavelength of the laser used for this experiment was 532 nm, which has a depth resolution at the micron level.[62] Thus, any structural modification that had occurred below micron level might be difficult to observe from this characterization technique. However, the difference in peak trends started to appear when the coating loading was above 7 wt%. For a 7 wt% Li-Mo-O coating, a broad peak corresponding to approximately 664 cm^{-1} appeared. This is an indication of T_{2g} mode from a shorter Mn–O spinel-like phase due to the oxygen displacement.[169] When the coating loading was increased up to 30 wt%, new peaks designated to spinel phase $LiMn_2O_4$ appeared at 580 cm^{-1} and 625 cm^{-1}.[171] Based on this appearance of spinel phase peaks for the 30 wt% coating, it was

concluded that the Li-Mo-O coating that had direct contact with HE-NCM was reacted with the cathode and established a spinel and/or spinel-like phase. The increase in coating contents can induce more oxygen vacancies in the cathode lattice upon heat treatment at 600 ºC and more oxygen extraction can lead to more aggressive metal migration to the 3a lithium site, thereby establishing more spinel phase. This explains why the intensity of the spinel peak increased from the coating loading of 7 wt% to 30 wt%.

The XPS depth profile for 3 wt% Li-Mo-O coated HE-NCM was used to identify the Mo entity at the sub-surface below the coating as well as the oxidation state of the transition metals (Figure 3.32 and 3.33). The probing depth for Ar sputtering is approximately 2 nm/60 seconds. Also, XPS survey data was used to compare the peak intensity of each element for different sputtering depths (Figure 3.32). From the survey data, the decrease in Mo^{6+} peak intensity after each sputtering was observed. This can be an indication that Mo from the coating is diffused from the surface of HE-NCM. Although the Ni and Co peak intensity were comparable after each sputtering, Mn peak intensity was increased after each sputtering which is inversely proportional to the Mo intensity.

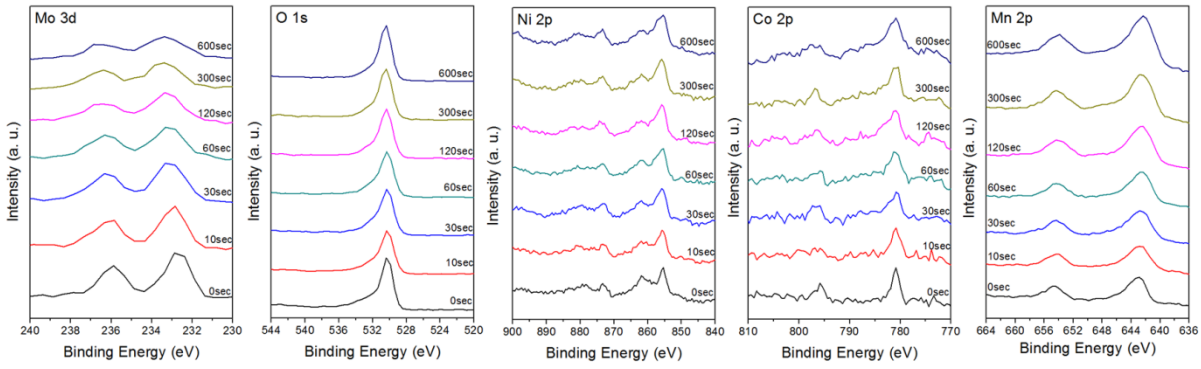

Figure 3.33 XPS depth profiling survey data for Mo 3d, O 1s, Ni 2p, Co 2p and Mn 2p from 3 wt% Li-Mo-O coating on HE-NCM at 600 ºC

To better observe the trend of the peak shape and its intensity, XPS depth profiling results of

10 seconds and 600 seconds Ar sputtering data were compared to each other (Figure 3.33).

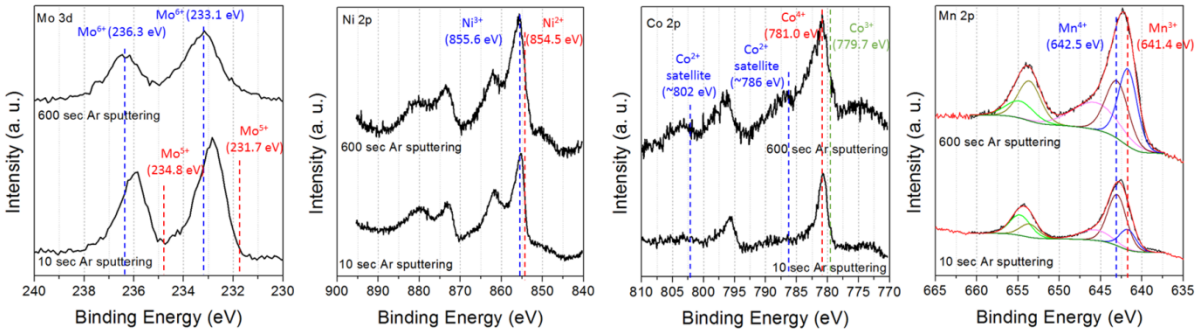

Figure 3.34 XPS depth profiling data for Mo 3d, O 1s, Ni 2p, Co 2p and Mn 2p at 10 seconds and 600 seconds Ar sputtering results from 3wt% Li-Mo-O coating on HE-NCM at 600 ºC[131,172-176]

Predominant oxidation states of Ni, Mn and Co at the surface (10 seconds Ar sputtering data) were observed to be 3+, 4+ and 4+, respectively (The Ni, Mn and Co oxidation state of bare HE-NCM should be close to 2+, 4+, 3+, respectively).[4] The increase in oxidation state of Ni and Co is possibly due to the Li extraction reaction by H_xMoO_{3+y} at 600 ºC increasing the oxidation state of transition metals.[149] The Mo oxidation state for Li_2MoO_4 should be Mo^{6+} and the 10 seconds Ar sputtering data correlating to Mo^{6+} may support the possibility of Li_2MoO_4 coating establishment on the HE-NCM surface. Also, Mo^{6+} peaks were observed from the 600 seconds Ar sputtering data and this can be an indication that Mo^{6+} is diffused on the HE-NCM surface up to 20 nm since the approximate sputtering probing depth is approximately 2 nm/60 seconds. The Ni 2p 10 seconds and 600 seconds Ar sputtering data are comparable to each other and the main peaks for both sputtering data maintained their peak position at 855.6 eV, which corresponds to Ni^{3+}.[172,175] A significant peak shape difference of 10 seconds and 600 seconds Ar sputtering data was observed from Co 2p XPS results. The significant increase of satellite peaks at 786 eV and 802 eV is observed which corresponds to Co^{2+} referenced to

CoO.[173,176] Based on the Co 2p 600 seconds Ar sputtering results, a speculation can be made that rocksalt CoO may have also formed along with the LNMO formation during the 600 ºC heat treatment in air. However, the XRD data does not show the evidence of rocksalt phase formation which can be an indication that the formation of CoO is very small. For Mn 2p XPS results, the peak at 641.4 eV (Mn^{3+}) was increased after 600 seconds Ar sputtering.[174] This could be because the oxygen vacancies induced from the 600 ºC heat treatment in air may lead to partial reduction of Mn^{4+} to Mn^{3+} due to the formation of off-stoichiometric LNMO ($LiNi_{0.5}Mn_{1.5}O_{4-x}$).[177]

The XPS depth profiling results show that Mo^{6+} is diffused on the 3 wt% Li-Mo-O coated HE-NCM surface during heat treatment at 600 ºC. However, the exact site of the Mo^{6+} placement in HE-NCM structure is difficult to identify with the currently available data. Previous reports regarding Mo^{6+} doping on disordered spinel LNMO claimed that Mo^{6+} can replace Ni and Mn which are in the 16d octahedral site of $[Li^+]_{8a}[TM_2]_{16d}O_4$.[177] Transition metals with similar atomic radii to Mo^{6+} (59 pm) such as Cr^{3+} (62 pm) and W^{6+} (60 pm) can also occupy octahedral sites of LNMO.[177] Also, a study by Sun et al. showed that Ti^{4+} (61 pm) can occupy both tetrahedral and octahedral sites of LNMO.[177] Considering the electron configuration of Mo^{6+} being $[Kr]5s^04d^0$, there is no 4d electrons for Mo^{6+}. Thus, the Ligand Field Stabilization Energies of octahedral and tetrahedral sites are both zero. Therefore, Mo^{6+} does not have any preference on octahedral or tetrahedral coordination.

Previous reports on Mo doped LNMO claim that the unit cell is slightly increased after Mo doping.[177] The increased unit cell after the cation doping is attributed to the increased repulsion forces within the lattice or larger size of the cation atomic radius if the inserted cation has the larger atomic radius.[177, 183] The d-spacing from XRD data can be calculated using

Bragg's law and compared to the d-spacing values from the spinel peaks of the reference LNMO and Li_2MoO_4 30wt% coated HE-NCM at 600 °C (Figure 3.34).

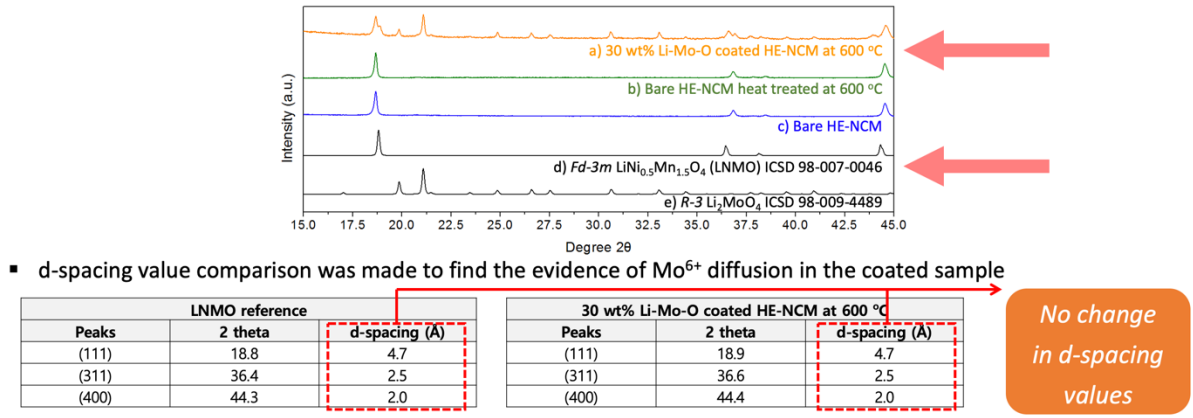

- d-spacing value comparison was made to find the evidence of Mo^{6+} diffusion in the coated sample

LNMO reference		
Peaks	2 theta	d-spacing (Å)
(111)	18.8	4.7
(311)	36.4	2.5
(400)	44.3	2.0

30 wt% Li-Mo-O coated HE-NCM at 600 °C		
Peaks	2 theta	d-spacing (Å)
(111)	18.9	4.7
(311)	36.6	2.5
(400)	44.4	2.0

No change in d-spacing values

Figure 3.35 The d-spacing values from LNMO reference peaks and spinel peaks of 30 wt% Li-Mo-O coated HE-NCM heat treated at 600 °C

Contrary to the expected result, the 30 wt% Li_2MoO_4 coated HE-NCM heat treated at 600 °C shows the same d-spacing values as the reference LNMO values. Although the d-spacing value was obtained up to one decimal place, a miniscule peak position difference for (311) and (400) peaks can be seen for LNMO reference and 30 wt% Li-Mo-O coated HE-NCM heat treated at 600 °C. The slight peak shift to the left for 30 wt% Li-Mo-O coated HE-NCM can be interpreted as an evidence of the smaller size of its unit cell. The smaller unit cell size for the coated HE-NCM heat treated at 600 °C could be attributed to the replacement of Ni^{2+} (69 pm) with a smaller atomic radii of Mo^{6+} (59 pm). In summary, the exact composition of the near-surface (below the coating) is difficult to identify with the currently analyzed data. It is certain that Mo^{6+} is diffused into the near-surface region up to approximately 20 nm according to XPS depth profiling analysis. However, the exact site where the Mo^{6+} is located is unclear at the moment since the calculated spinel phase d-spacing data of the coated and the reference LNMO are comparable each other. By observing the degree of higher degree peak shift (e.g. (311) and

(400) peaks) between the coated and the reference LNMO, the peak shift for the coated sample shows slight peak shift to the right. This means that the unit cell for the coated sample is slightly smaller than the reference LNMO. Considering the ionic radius of Ni^{2+}, Co^{3+}, Mn^{4+} and Mo^{6+}, the decrease of unit cell for the coated sample could possibly be an indication that Ni^{2+} may have been replace with Mo^{6+}. This may have decreased the unit cell of the coated HE-NCM. Also, the octahedral and tetrahedral site of the Ligand Field Stabilization Energy of Mo^{6+} are both zero which means that Mo^{6+} does not have any preference on octahedral or tetrahedral coordination. The Mo^{6+} may not even be located in the spinel structure and it may be diffused into the layered $(Li)_{3a}[TM]_{3b}O_2$ structure of either 3a or 3b octahedral sites. To find the exact location of diffused Mo^{6+} in the HE-NCM near-surface region, advanced X-ray techniques such as Extended X-ray Absorption Fine Structure is needed. The interatomic distances between TM – O can be used to gain structural information. A study using X-ray Absorption Near Edge structure analysis can be incorporated to find an accurate average valence state of the metal ion on the near-surface region.[179] A speculation was made that there may be rocksalt CoO formed along with LNMO in the near-surface region since the reduction of Co is observed from XPS depth profile analysis. For the composition of the coated material, the coated entity went through chemical reactions with the HE-NCM at the surface. However, the exact structural information of the 3 wt% Li-Mo-O coating is difficult to identify due to the detection limit of the diffractometer. Based on the XRD data of the 30 wt% coating at 600 ^{o}C, Li_2MoO_4 was established from the reaction between HE-NCM and H_xMoO_{3+y}. However, the XRD results from the 30 wt% Li-Mo-O coating does not represent the 3 wt% coating as there are other possibilities for 3 wt% coating to form a different structure with a different composition (e.g. a possibility of a solid solution phase from HE-NCM and Li_2MoO_4). It is certain that for 3 wt%

coated HE-NCM, there is an even distribution of Mo on the surface based on the EDS data. The presence of oxygen is confirmed by XPS data along with the proof of the MoO_3 induced Li^+ extraction reaction by observing an increase in oxidation state of Ni, Co, and Mn to be from 2+, 3+ and 4+ to higher oxidation states at the surface of HE-NCM. Therefore, the coated material should be composed of Li, Mo and O for 3 wt% coated HE-NCM.

3.5.2 Electrochemistry

An electrochemical cycle performance test was conducted on the 3 wt% Li-Mo-O coated HE-NCM at various calcination temperatures to observe the heat treatment effect on Li-Mo-O coated HE-NCM. Coating loading was fixed to 3 wt% to see exclusively on the temperature effect. Li-Mo-O coated HE-NCM was heat-treated from 300 to 700 °C and used to fabricate coin cells to conduct cycling tests (Figure 3.36). The sample with the lowest calcination temperature (300 °C) exhibited the lowest discharge capacity and stability. As the heat treatment temperature increases, the capacity and stability of the cells also increased. The cells with material from the 600 °C heat treatment exhibited the best performance among all the cells. The cells with 700 °C calcined coated HE-NCM were exhibiting lower performance than the sample that went through 600 °C heat treatment.

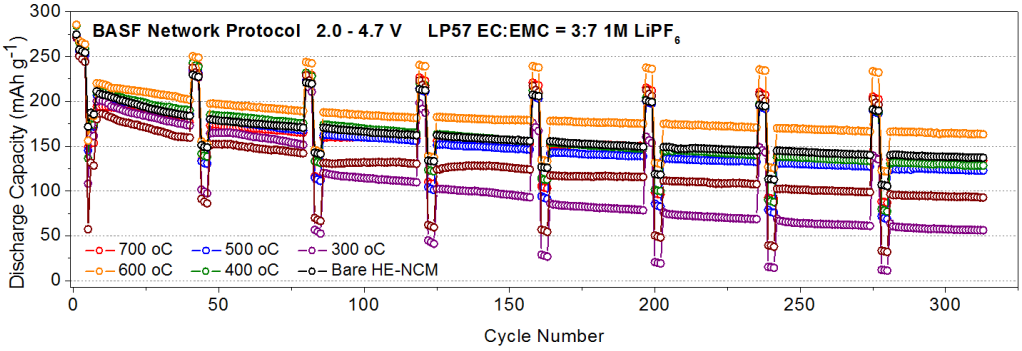

Figure 3.36 3 wt% Li-Mo-O coated HE-NCM with various calcination temperatures

To better understand the cycling results, 0.1C differential capacity profiles of all cells were closely examined from long term cycling results. The 0.1C results were chosen for the differential capacity plot analysis to minimize the overpotential and gather the phase transition information of the cathode. As the cycle continues, all of the cells, whether they were coated or not, exhibited phase transformation from a layered to a spinel-like phase since the oxidation and reduction peaks at 3.6 V and 3.2 V, respectively shifted right and left (Figure 3.37).

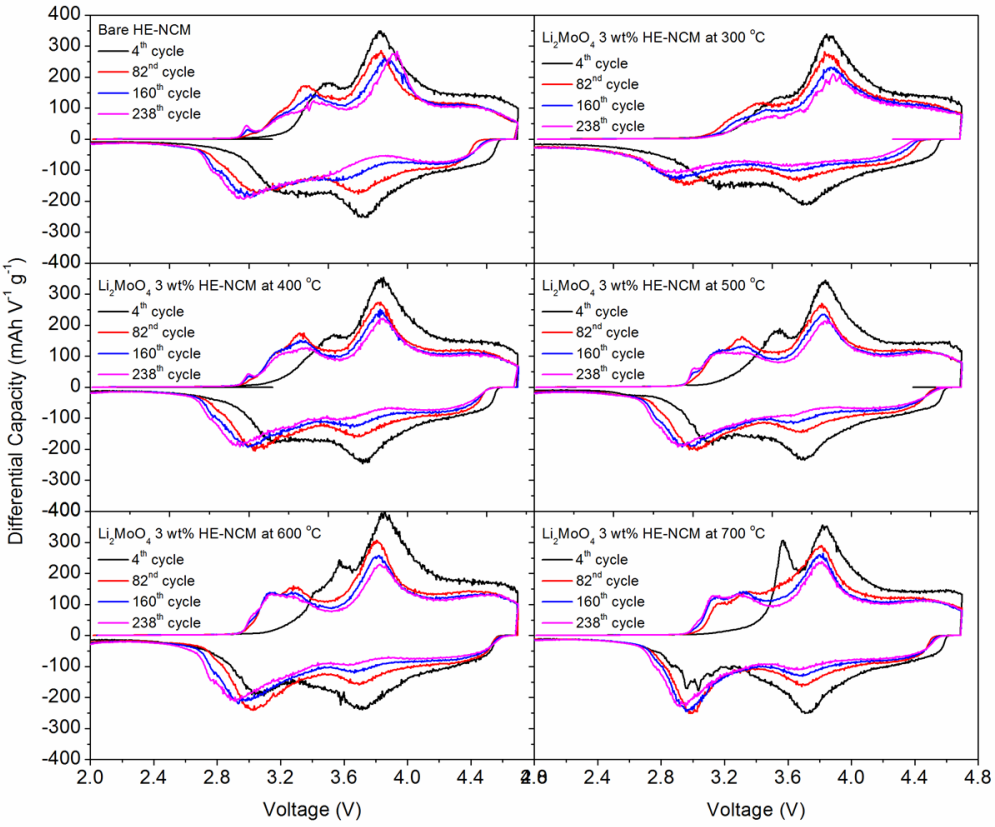

Figure 3.37 0.1C cycle voltage profile of 3 wt% Li-Mo-O coated HE-NCM with various calcination temperatures

This phase transformation phenomenon corresponds to the studies from Ogumi et al., and many others.[178,179] Oxidation and reduction of oxide ions contribute to the evolution of redox peaks at specific voltages.[41,43,142,157,179,180] Some amount of oxygen reduction occurs between 3.0 and

3.2 V where Mn reduction also occurs.[146] Mn redox gradually evolves from $LiMnO_2$ to a spinel-like Mn redox due to the structural transformation from layered to spinel phase by Mn migration from the transition metal to the lithium layer along with some lattice oxygen release. The spinel-like phase then can be created from the cathode's secondary particles over many cycles. Thus, a spinel-like Mn redox in the charging and discharging processes was recognized to be the result of the Mn charge compensation induced from lattice oxygen release.[146] This increases the Mn spinel-like phase peak intensity in the differential capacity plot. The situation worsens when lattice oxygen release continues to occur. The spinel-like phase can lose more lattice oxygen over cycles, and the amount of (de)lithiation continuously decreases along with the oxygen loss and metal dissolution from the structure (decrease in spinel-like peak intensity), and the structure eventually goes from spinel to rocksalt phase (further peak shift to lower voltage).[17,60,78] This structural degradation process can be monitored by the Mn redox peak shift and peak intensity from the differential capacity plot. With this knowledge from the differential capacity plot analysis, structural degradation of bare HE-NCM was closely examined. As the long-term cycle continues, bare HE-NCM's Mn reduction peak was shifted from 3.2 V to ~ 2.9 V. A continuous Mn reduction peak shif was observed for the bare HE-NCM. This reduction peak shift could be the result of continuous structural degradation of the layered to spinel phase as well as an increase in overpotential due to the deposition of inorganic byproduct such as LiF.[17,181] The inorganic byproducts can be deposited on the surface of HE-NCM by multiple reaction routes. The residual lithium contents such as LiOH and Li_2CO_3 on the HE-NCM surface can react with CO_2, which is from the oxidation of EC to form more Li_2CO_3 and H_2O.[182] The $LiPF_6$ in the electrolyte is highly unstable within the working voltage of LIB and thus disintegrates to become LiF and PF_5. The formed PF_5 then can react with H_2O

from the abovementioned reaction between residual lithium and CO_2 to yield LiF. The detailed reaction is stated in Figure 1.12.[56,182] The other route to deposit inorganic byproduct is with the reaction of singlet oxygen and EC. When the evolution of singlet oxygen from the cathode lattice occurs during high voltage charging (> 4.4 V), the singlet oxygen can react with EC and yield hydrogen peroxide (H_2O_2) and vinylene carbonate (VC).[17] The H_2O_2 can be oxidized by the following reaction:

$$3H_2O_2 \rightarrow 2H^+ + 2e^- + 2O_2 + 2H_2O$$

Equation 3.3 Oxidation of H_2O_2 [17]

The yielded H_2O then can further react with $LiPF_6$ to yield LiF and deleterious HF.[24] LiF is a well-known insulator, and a significant amount of LiF deposition on the cathode can seriously reduce its electronic conductivity, thus increasing the cell's overpotential.[14,57,58,182] The Mn oxidation peak at 3.5 V was shifted to 3.3 V. As the cycle continued, the intensity of the oxidation peak decreased, which indicates continuous lattice oxygen loss from the spinel-like phase to become a spinel phase.[146] This claim is further verified by the identification of small spinel phase oxidation peak growth of the 160th cycle at approximately 3.0 V. The intensity of this spinel oxidation peak was further increased as the cycle continued. The result of the cell's overpotential increase can also be seen by observing an oxidation peak shift from 3.8 V to 3.9 V. The oxidation peaks at 3.8 V correspond to the oxidation of Ni^{2+} and Co^{3+} from $LiTMO_2$.[37] The peak decrease was observed from bare HE-NCM until the 82nd cycle, and a peak shift from 3.8 V to 3.9 V occurred at the 160th cycle. The peak shift continued until the 238th cycle. This shift can be attributed to the deposition of LiF, and other insulating byproducts from the reaction between residual lithium on the surface of bare HE-NCM and CO_2 from EC oxidation.[56] The observed overpotential could also be attributed to the reaction between singlet

oxygen and EC to form LiF on the HE-NCM surface. The significant decrease of differential capacity profile area can be seen at above 4.4 V, which corresponds to oxidation of oxide ions.[50,52] A significant reduction in peak intensity decrease was observed for the oxide ion reduction region. This further indicates that significant lattice oxygen was lost during cycling. A substantial loss of the reduction peak intensity corresponding to Ni^{3+} and Co^{4+} reduction were observed along with its peak shift from 3.7 V to 3.5 V due to the structural transformation to spinel phase and increased overpotential from the byproduct deposition on the surface.

Li-Mo-O coated HE-NCM at 300 °C exhibited the most severe degradation behavior among all heat-treated samples. This could indicate that the lower amount of formed Li-Mo-O coating (due to the insufficient thermal energy to initiate Li and O extraction) was not beneficial towards the battery cycle performance or it could be that the insufficient amount of Mo^{6+} diffusion into the near-surface occurred at 300 ºC. Continuous redox peak intensity decrease and severe Mn reduction peak shift to the lower voltage was observed. However, the overpotential caused by additional byproduct deposition along the cycle appeared to be less than the bare sample since an insignificant amount of the oxidation peak shift was observed at 3.8 V. This could be because of most of the insulating byproducts that were deposited on the surface of bare HE-NCM originated from residual LiOH and Li_2CO_3.[56-58,182] The deposition of the residual lithium species causing overpotential rise is again verified by examining the redox peak shift from DMSO washed HE-NCM, which will be discussed in the later section. A severe decrease in redox peak for Li-Mo-O coated HE-NCM at 300 °C revealed that the calcination temperature of 300 °C may not be enough to diffuse a sufficient amount of Mo^{6+}. It could also be due to insufficient amount of Li-Mo-O is formed at 300 °C since the Li_2MoO_4 XRD peaks kept increasing up to 600 °C based on the 30 wt% coating XRD data. The redox peak intensity

retention was improved along with the calcination temperature increase. The oxide ion redox area (greater than 4.4 V) is especially preserved as the heat treatment temperature increases. At the calcination temperature of 600 °C, the Li-Mo-O coated HE-NCM showed significant improvement in preserving the oxide ion redox peak area compared to bare HE-NCM.

This increased reversibility of the anion redox can be attributed to effectively preserving redox-active lattice oxygen.[49-52] The anion redox peak retention was improved along with the calcination temperature increase. Due to the higher dissociation energy of Mo – O (502 kJ mol^{-1}) compared to Co – O (397.4 kJ mol^{-1}), Ni – O (366 kJ mol^{-1}), and Mn – O (362 kJ mol^{-1}), metal – oxygen bonding can be strengthened when Mo^{6+} is diffused into the HE-NCM structure and ultimately mitigate the release of oxide ions during long-term battery cycling. Also, the formed Li-Mo-O coating at 600 ºC can prevent the side reactions between the cathode interface and electrolyte which can further promote longer battery cycle life.

The sample that was heat treated up to 700 °C showed a reduced oxygen ion redox region as well as a more prominent Mn reduction peak at 3.0 V over cycles. Based on the data, this could be because of too much oxygen vacancies induced from Li and O extraction reactions by molybdenum oxide hydroxide hydrate during heat treatment at 700 °C. A smaller amount of redox-active oxygen ions on the surface region could have been reserved along with the increased formation of the spinel-like phase. These events might have lowered the capacity for the 700 °C heat treated coated sample. It could also be that the heat treatment at 700 °C induces more oxygen vacancies which can induce more spinel phase as well. As the LNMO synthesis above 700 °C can yield off-stoichiometric $LiNi_{0.5}Mn_{1.5}O_{4-x}$, a similar off-stoichiometric phenomenon may have occurred for the coated HE-NCM at 700 °C.

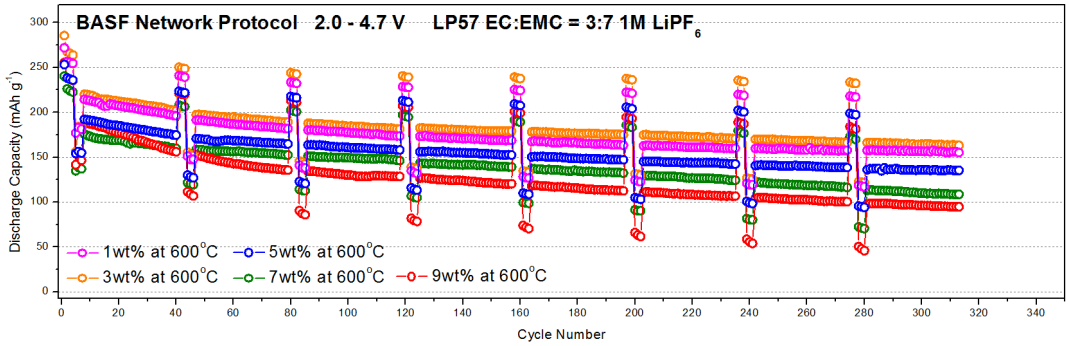

Figure 3.38 Cycle test with different Li-Mo-O coating loading on HE-NCM

A cycle test was performed with different coating loading as well (Figure 3.38). The heat treatment temperature was fixed at 600 °C to observe the effect from the variation of the coating loading. In accordance with many other metal oxide coatings literature sources, the optimal loading for Li-Mo-O coating turned out to be 3 wt%. Many previous studies claimed that the thickness of the coating affects electrochemical performance.[79,84,183-185] If the insulating coating is too thick, the electronic conductivity reduces significantly which can lower the cathode cycle performance. Also, the capacity contribution from the coating is negligible since the redox potential for the Li_2MoO_4 appears at below 2V. Thus, the increase in coating loading can lower the absolute capacity of the electrode. On the other hand, the insufficient thickness of the coating can cause imperfections. The uncoated part of the cathode surface is then vulnerable from electrolyte oxidation and HF attack, which can further cause detrimental issues such as additional CEI growth and transition metal dissolution.[186-188]

Based on the long term cycle studies and the differential capacity analysis, Li-Mo-O surface modification shows an improved cycling performance on HE-NCM. However, there were some unanswered questions regarding the coating, such as the effect of the addition of 0.1 wt% LiOH, Li-Mo-O coating synthesis without addition of 0.1 wt% LiOH, residual lithium washing effects by the solvent used during the coating process, and the contribution of the Mo

diffused HE-NCM without Li-Mo-O coating. The powder XRD analyses that were performed on 1 wt% LiOH coated HE-NCM at different calcination temperatures in air revealed that there was no structural difference between the bare HE-NCM and LiOH coated HE-NCM (Figure 3.29). The spinel peaks which were identified during heat treatment above 400 °C for the 30 wt% Li_2MoO_4 coated HE-NCM were not observed for 1 wt% LiOH coated HE-NCM. Thus, the conclusion was made that H_xMoO_{3+y} was reacted with the HE-NCM surface during the sintering process and possibly yielded Li-Mo-O coating on the surface of HE-NCM. Also, the high temperature synthesis of 600 ºC induces Mo surface diffusion.

To determine if the addition of LiOH makes any difference in electrochemical performance, bare HE-NCM coated with 0.1 wt% LiOH using DMSO (the same LiOH amount that was used in the Li-Mo-O coating process) with 600 °C calcination in air was used to make cells to conduct long-term cycling tests (Figure 3.39). Also, bare HE-NCM was added in the DMSO solution and evaporated at 200 °C with a constant stirring rate. The precipitated sample was then retrieved to conduct a 600 °C heat treatment. Coin cells were made from the DMSO washed and heat treated sample and directly compared to the electrochemical cycle performance with the bare HE-NCM.

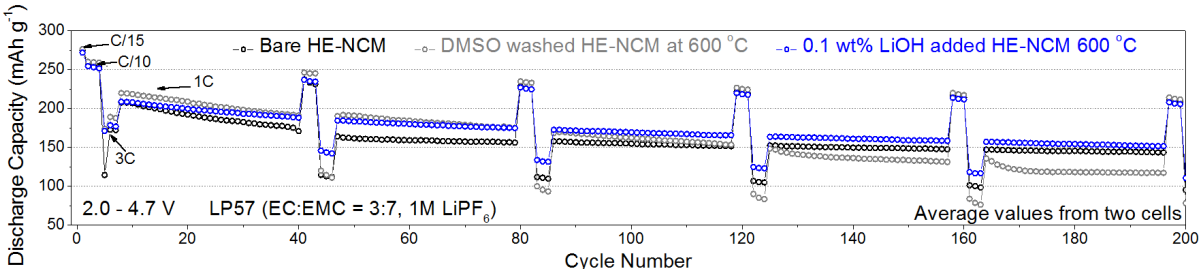

Figure 3.39 Cycle test with bare HE-NCM, 0.1 wt% LiOH added HE-NCM, and DMSO washed bare HE-NCM

The DMSO washed bare HE-NCM showed slightly better cycle performance versus

unwashed bare samples in the beginning of the test. Higher discharge capacities for a low rate (0.1C rate) as well as the high rates (3C and 1C rate) were exhibited for the washed HE-NCM until the 125th cycle. Cycle stability seemed to become less stable than unwashed bare HE-NCM after 125th cycle. After the 125th cycle, washed HE-NCM showed inferior discharge capacity results for every C-rate. The data for 0.1 wt% LiOH added HE-NCM showed somewhat similar cycle results with DMSO washed HE-NCM cells up to 120th cycle and then the cycle trend became a quite similar to the bare HE-NCM after the 120th cycle.

Improved initial discharge capacity performance for the DMSO washed bare HE-NCM seemed to be attributed from the washing effect and subsequent heat treatment in air. DMSO washing and heat treatment at 600 ºC may have removed residual lithium hydroxide and carbonate on the surface of HE-NCM. Due to the reduced residual lithium on the surface of HE-NCM, diminished side reactions between EC and lithium carbonate and hydroxide may have occurred, thereby yielding less deposition of inorganic byproducts such as LiF on the

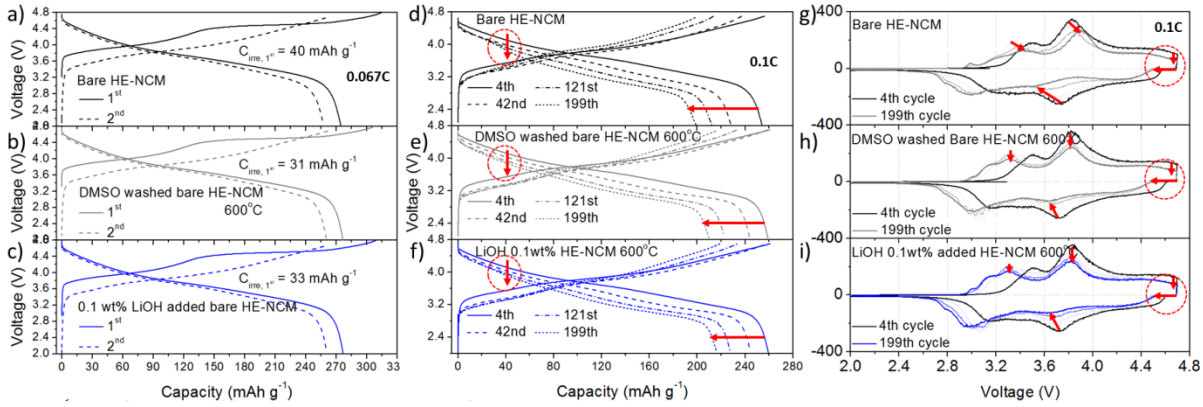

Figure 3.40 Voltage profiles and differential capacity plots from bare HE-NCM, LiOH added HE-NCM, and DMSO washed bare HE-NCM

cathode surface. Figure 3.40 supports this claim by showing increased overpotential from the

199th cycled bare HE-NCM, whereas no such increase in overpotential was observed from the washed HE-NCM. The oxidation peak at 3.8 V is shifted to 3.9 V for the unwashed HE-NCM, but DMSO washed HE-NCM exhibited no such peak shift. However, direct contact between electrolyte and bare the HE-NCM surface still existed, and this may have caused electrolyte oxidation.[17,24] Also, the problem of lattice oxygen release was still unresolved and continuous structural degradation occurred for DMSO washed bare HE-NCM. Recent studies from Cho et al. revealed that the washing process can substantially decrease residual lithium contents.[29,189] However, performing the washing process alone can yield an additional thin lithium amorphous layer with a thickness below 8 nm. This layer is originated from lithium loss from the host surface structure, which then facilitates phase transformation to a rocksalt structure. The structural degradation propagates from the surface to bulk over battery cycles and this may be the reason for the cycle performance difference between bare and DMSO washed bare HE-NCM. The additional thin surface layer induced by washing may have lowered the high C-rate performance. By observing the 199th cycle for LiOH added HE-NCM, unwashed HE-NCM, and DMSO washed bare HE-NCM, oxide ion redox peak intensity was substantially decreased for all samples, indicating that anion redox capability was lost during cycles due to lattice oxygen loss. Over cycles, 0.1 wt% LiOH coated HE-NCM showed comparable discharge capacity degradation compared to washed HE-NCM. By analyzing the differential capacity plot of both washed HE-NCM and 0.1 wt% LiOH coated HE-NCM, the degraded profiles appeared to be very similar to each other. Considering a minimal amount of LiOH addition with respect to the weight of HE-NCM, the 0.1 wt% LiOH coated HE-NCM should be close to DMSO washed HE-NCM.

However, the 3C cycle data from 0.1 wt% LiOH coated HE-NCM exhibited improved

results compared to bare and DMSO washed bare HE-NCM. This could be because of the thin LiOH coating created on HE-NCM after the washing and heat treatment process. A study from Samsung Advanced Institute of Technology revealed that LiOH on the surface of cathodes can melt during high-temperature heat treatment since the melting point of LiOH is around 462 °C.[14] The melted LiOH coats on the cathode surface and may promote the additional formation of thin layers of Li_2CO_3 and LiOH during cooling. The study claimed that the thin coating is a low resistance layer which can promote high rate performance. The calcination temperature used in this experiment was 600 °C, which is certainly high enough to melt LiOH on the HE-NCM surface. Because of the low resistance thin layer created by the addition of LiOH, 0.1 wt% LiOH coated HE-NCM may have revealed improved high C-rate performance compared to bare HE-NCM and DMSO washed HE-NCM. However, continuous capacity degradation was observed for 0.1 wt% LiOH coated HE-NCM. Just as bare and washed bare HE-NCM, continuous capacity degradation from 0.1 wt% LiOH coated HE-NCM can also be attributed to the incapability of retaining lattice oxygen during battery cycles, which eventually leads to structural degradation over the long term battery cycle. The differential capacity plot also supports this claim. The cycled differential capacity profile of 0.1 wt% LiOH coated HE-NCM is very close to DMSO washed HE-NCM. Especially at the oxide ion redox region at above 4.0 V, a significant decrease in the area was identified.

Figure 3.41 revealed the cycle performance from bare HE-NCM, 3 wt% Li-Mo-O coated HE-NCM with 0.1 wt% LiOH addition during the coating process and heat treatment at 600ºC, 3wt% Li-Mo-O coated HE-NCM without 0.1 wt% LiOH addition during the coating process and heat treatment at 600ºC, and water washed 3wt% Li-Mo-O coated HE-NCM. The cycle data from 3 wt% Li-Mo-O coated HE-NCM with and without 0.1 wt% LiOH addition

were very close to each other and both exhibited improved cycle results compared to bare HE-NCM. Water washed 3 wt% Li-Mo-O coated HE-NCM showed slightly lower cycle performances. The lower performance of the water washed 3 wt% Li-Mo-O coated HE-NCM could be attributed to the absence of Li-Mo-O coating, which can facilitate electrolyte oxidation and subsequent thickening of CEI during long-term battery cycling. However, early cycle performance of the water washed sample showed improved cycle performance compared to the bare HE-NCM until about the 80th cycle. This could be due to the effect from the diffused Mo^{6+} at the surface of HE-NCM delaying oxygen release due to the high dissociation energy of Mo – O. The cathodes with the spinel phase formed on the near-surface are the cells except for the bare HE-NCM (Figure 3.41). Based on the 3C rate performance, the cathode with spinel phase formed at the near-surface appeared to be beneficial towards high rate discharge performance due to the 3D Li^+ diffusion pathways.

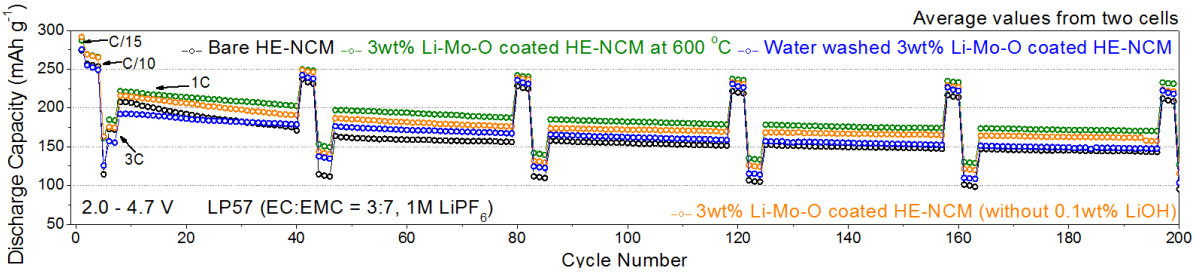

Figure 3.41 Cycle test with bare HE-NCM, 3 wt% Li-Mo-O coated HE-NCM, and water washed 3 wt% Li-Mo-O coated HE-NCM

The first cycle irreversible capacity of bare HE-NCM and 3 wt% Li-Mo-O coated HE-NCM with 0.1 wt% LiOH addition and heat treatment at 600 ºC were compared to each other in Figure 3.42. The bare HE-NCM displayed its first cycle irreversible capacity to be 40 mAh g^{-1}, whereas the coated HE-NCM showed its irreversible capacity to be 29 mAh g^{-1}. The difference in irreversible capacities for bare and coated HE-NCM seemed to be attributed to

the decomposition of residual lithium compounds during the first charge. Considering the

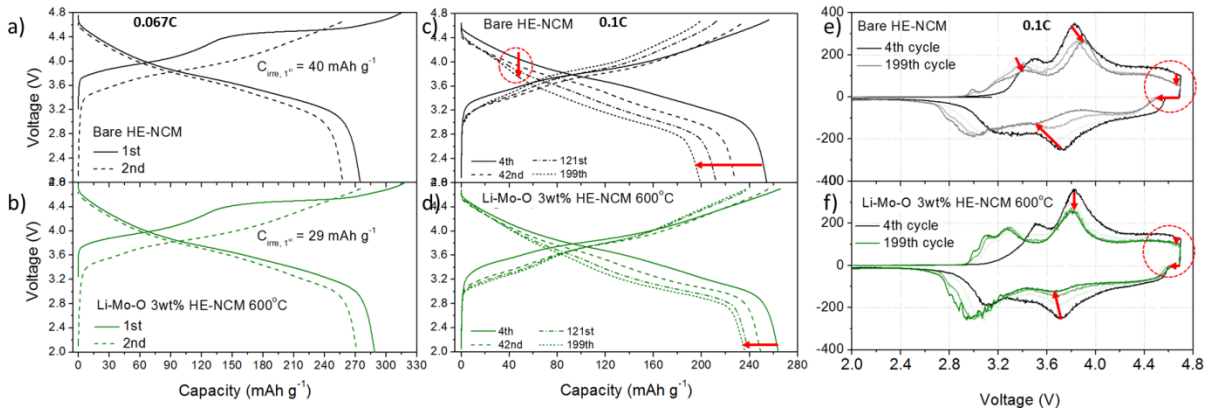

Figure 3.42 Voltage profiles and differential capacity plots from bare HE-NCM and 3 wt% Li-Mo-O coated HE-NCM with 0.1 wt% LiOH addition and heat treatment at 600 °C

first cycle irreversible capacity for DMSO washed bare HE-NCM is 31 mAh g^{-1}, the Li-Mo-O 3 wt% coated HE-NCM displayed comparable first cycle irreversible capacity (29 mAh g^{-1}) with the DMSO washed bare HE-NCM. This result showed that simple removal of the residual Li compounds on the HE-NCM surface can improve the first cycle irreversible capacity.

The voltage profiles at each 0.1C cycle for bare and coated cells were compared in figure 3.42 c and d. The voltage degradation trends for two samples were similar up to the 121st cycle. However, the phase transformation for the coated cells started to stabilize starting from the 121st cycle and a very similar voltage profile with small degradation was displayed. One other notable feature is the sudden voltage drop at approximately 4.0 V for the 199th cycle for bare HE-NCM (Figure 3.42 c red circled area). Such a drop did not occur for the coated HE-NCM and this can be an indication that Li-Mo-O coating is effective especially in maintaining the capacity above 4.0 V. The phase transformation trend was better identified from differential capacity plots in Figure 3.42 e and f. Bare HE-NCM displayed severely

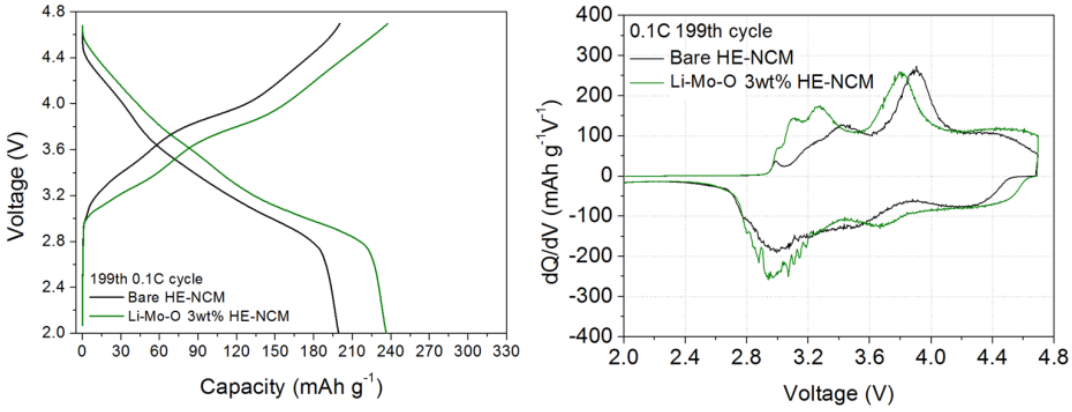

Figure 3.43 Voltage profiles and differential capacity plots from bare HE-NCM and 3 wt% Li-Mo-O coated HE-NCM with 0.1 wt% LiOH addition and heat treatment at 600 °C at 199th cycle with 0.1C rate

reduced area above 4.0 V over cycles which correspond to the redox region of oxide ions. The area was preserved for the Li-Mo-O coated HE-NCM which can be an indication that the 600 °C heat treated Li-Mo-O coated HE-NCM is effective towards reserving lattice oxygen during cycles. The phase transition below 4.0 V did occur for both the bare and coated HE-NCM. However, the degree of phase transition for 600 °C heat treated Li-Mo-O coated HE-NCM was less than bare HE-NCM. The difference between the bare and coated HE-NCM can be clearly recognized by comparing the 199th cycle voltage profiles and their differential capacity plots. Figure 3.43 clearly shows where the capacity differences mainly occur for the two samples: the redox region above 4.0 V and the spinel-like Mn and oxygen redox region at around 3.0 V.

The cycle data from 600 °C heat treated 3 wt% Li-Mo-O coated HE-NCM was also directly compared to the DMSO washed HE-NCM heat treated at 600 °C to observe the synergetic effect from the Li-Mo-O coating and Mo^{6+} surface diffusion on HE-NCM (Figure 3.44). At first, the cycle performances were similar to each other up to approximately the 40th cycle. However, the cycle performance of the DMSO washed bare HE-NCM and the coated

HE-NCM started to deviate from the 40th cycle onward.

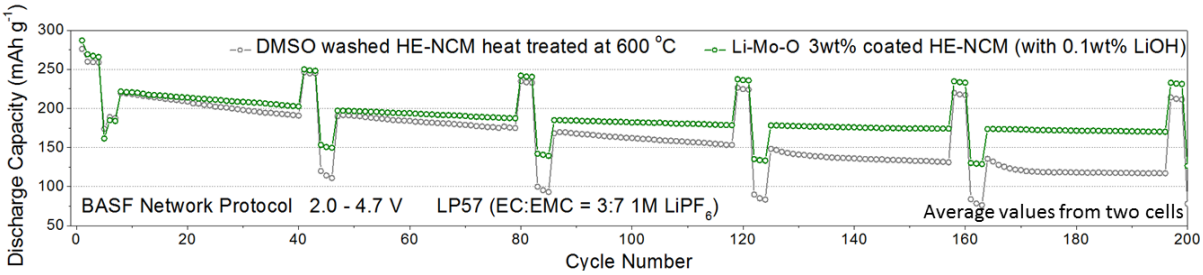

Figure 3.44 Cycle test with DMSO washed bare HE-NCM and 3 wt% Li-Mo-O coated HE-NCM with 0.1 wt% LiOH addition and heat treatment at 600 °C

To better analyze the cycle performance of the DMSO washed and the coated HE-NCM, voltage profiles and their differential capacity plots were compared (Figure 3.45). The first and second cycle data were comparable to each other. However, a noticeable difference was observed starting from the 121st 0.1C cycle. A small phase transformation from the coated HE-NCM was observed at the 199th 0.1C cycle, whereas continuous phase transformation occurred for DMSO washed HE-NCM which led to capacity degradation. The differential capacity plots in Figure 3.45 also show a degradation trend for the DMSO washed

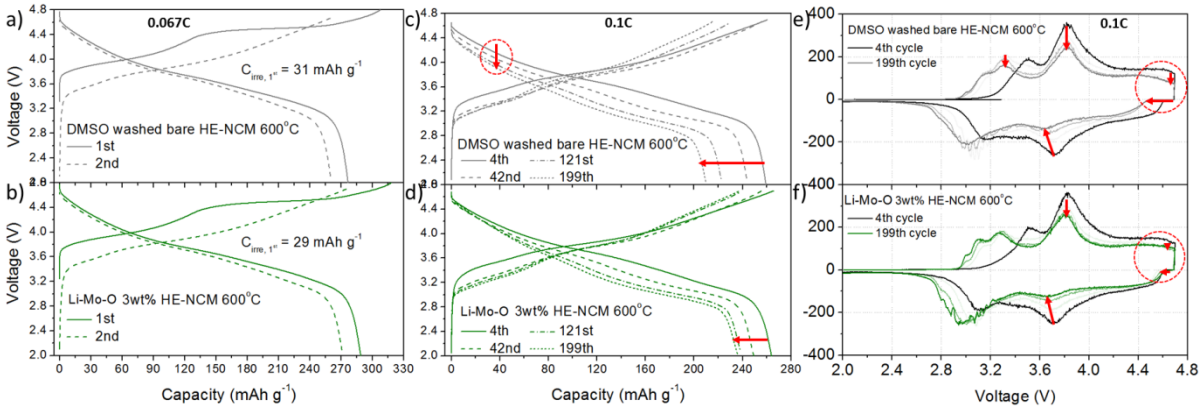

Figure 3.45 Voltage profiles and differential capacity plots from DMSO washed bare HE-NCM and 3 wt% Li-Mo-O coated HE-NCM with 0.1 wt% LiOH addition and heat treatment at 600 °C

bare and coated HE-NCM. The DMSO washed bare HE-NCM shows a similar degradation trend from unwashed bare HE-NCM. The coated HE-NCM shows improved redox peak retention especially at above 4.0 V.

The phase transformation mitigated by surface modification of HE-NCM can be better seen from the comparison data of the 0.1C 199th cycle voltage profiles and their dQ/dV plots (Figure 3.46). The data clearly shows where the performance difference occurs. From the data, a majority of the performance difference was attributed to the redox performance above 4.0 V. There was a small difference in the redox peak area at 3.0 V, which is designated to spinel-like Mn redox and a small portion of oxide ion redox. A conclusion from this data can be made that the synergetic effect from the Li-Mo-O coating as well as Mo^{6+} diffusion at the near-surface region of HE-NCM can provide better cycle stability. The Li-Mo-O coating may effectively prevent EC oxidation during high voltage operation. The Mo^{6+} surface diffusion on HE-NCM near-surface region can provide the benefit of retaining lattice oxygen during battery cycling due to the high dissociation energy of Mo – O relative to other TM (Ni, Co and Mn) – O.

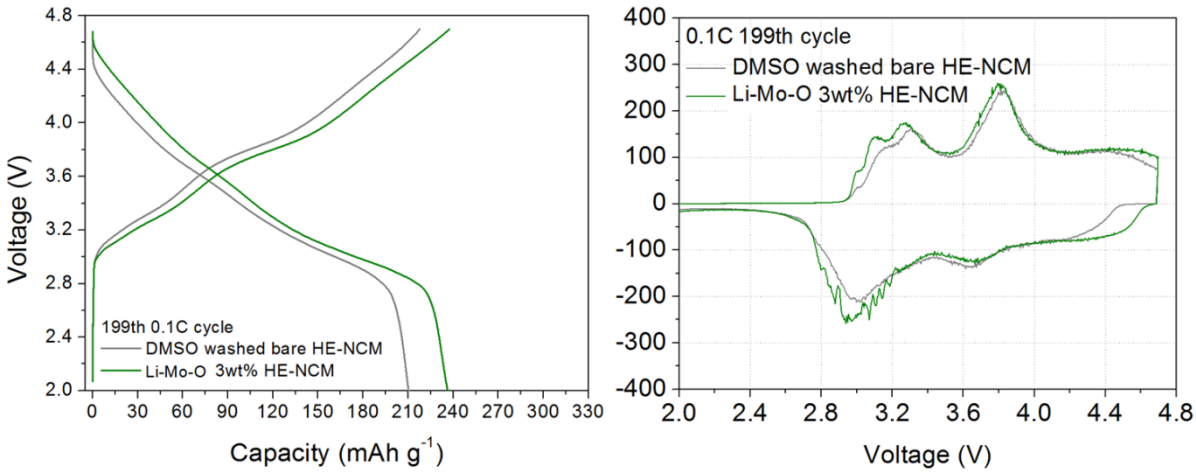

Figure 3.46 Voltage profiles and differential capacity plots from DMSO washed bare HE-NCM and 3 wt% Li-Mo-O coated HE-NCM with 0.1 wt% LiOH addition and heat treatment at 600 °C at 199th cycle with 0.1C rate

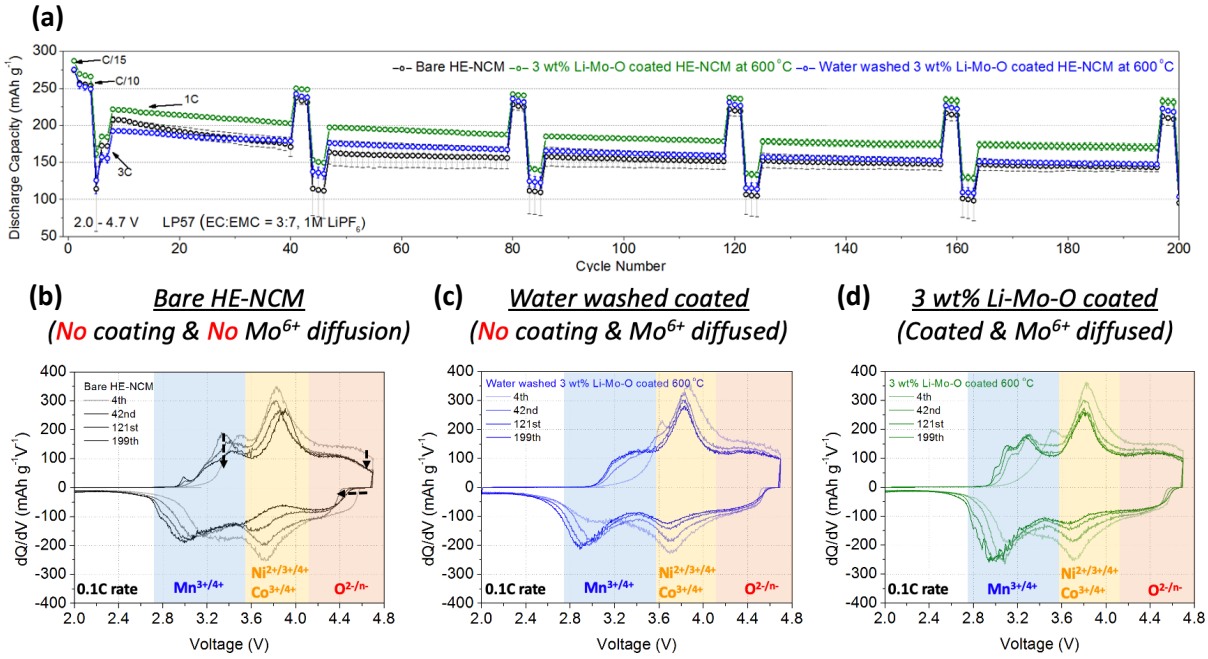

Figure 3.47 Cycle test and differential capacity analysis from bare HE-NCM, water washed 3 wt% coated HE-NCM and 3 wt% Li-Mo-O coated HE-NCM

Cycle test results and differential capacity profiles from Bare HE-NCM, water washed 3 wt% Li-Mo-O coated HE-NCM heat treated at 600 °C and 3 wt% Li-Mo-O coated HE-NCM heat treated at 600 °C were directly compared to each other (Figure 3.47). Compared to bare HE-NCM, water washed coated HE-NCM showed stabilized overall redox peaks including oxide ion redox region. However, reduced Mn oxidation peak was observed at around 3.0 – 3.2 V. This is possibly due to the water washing effect which can induce surface degradation according to Cho et al.[29] However, 3 wt% Li-Mo-O coated HE-NCM at 600 °C showed stabilized overall redox peaks including oxide ion region over long-term battery cycles.

The impedance study was performed on the bare and 3 wt% Li-Mo-O coated HE-NCM with 0.1 wt% LiOH addition and heat treatment at 600 °C (Figure 3.48). The impedance data was first collected at the mean discharge voltage (3.65 V) after the first cycle and then collected

after the end of BASF network cycle protocol (313rd cycle). The impedance data after the first cycle showed slightly higher interfacial resistance for the coated cell. This is believed to be due to the presence of Li-Mo-O coating. A slightly higher charge transfer resistance in the medium frequency region was also displayed from the coated cell. This could be attributed to the effect from the insulating property of Li-Mo-O compound coating. The impedance data for the cycled cells showed a noticeable difference between the bare and coated cell. The reduced interfacial resistance and charge transfer resistance may be attributed to the effect from reduced lattice oxygen loss. The reduced oxygen evolution can decrease a possibility of undesirable reaction between singlet oxygen and electrolyte which can ultimately reduce excess CEI formation. The evolution of singlet oxygen can occur in the process of lattice oxygen loss at high voltage operation. Although the cause of the singlet oxygen evolution is currently under investigation

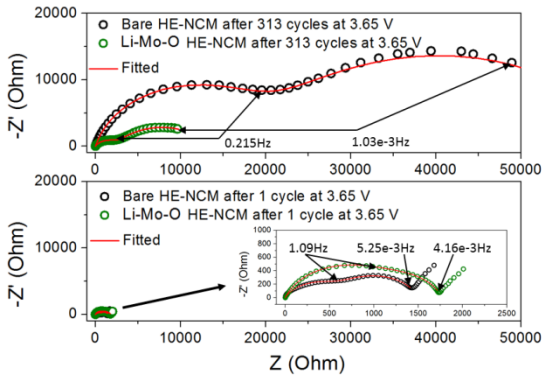

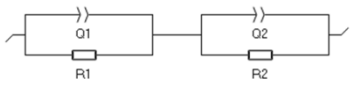

R1	Interfacial resistance
R2	Charge transfer resistance
Q	Capacitance

	Sample	R1 (kohm)	Q1 (uF)	R2 (kohm)	Q2 (uF)
After 1 cycle	Bare	0.613	1.29e+3	0.898	1.43e+3
	Coated	1.15	0.710e+2	0.615	8.88e+2
After 313 cycles	Bare	18.6	0.112e+2	45.1	1.52e+2
	Coated	2.41	0.817e+2	10.9	1.08e+3

Frequency Range	High Frequency (1000-10 Hz)	Medium Frequency (10-0.1 Hz)	Low Frequency (< 0.1 Hz)
Corresponding Resistance	Film resistance	Charge transfer resistance	Solid state diffusion resistance

Figure 3.48 Electrochemical impedance spectroscopy (EIS) data from bare and Li-Mo-O 3 wt% coated HE-NCM with 0.1 wt% LiOH addition and heat treatment at 600 °C before and after cycling

by many other researchers, lattice oxygen release can induce more singlet oxygen, which further reacts with EC in the electrolyte to form H_2O_2 and VC, according to Gasteiger et al.[17]

The formed H_2O_2 can be oxidized and lead to H_2O, which can further react with $LiPF_6$ to form LiF and HF according to Figure 1.12. Since LiF is a well-known electrical insulator, the increased formation of LiF on the cathode surface may increase the impedance of the cell. This may be the reason for the impedance increase in bare HE-NCM after cycling.

3.6 Conclusion

The enhanced electrochemical performance from the 3 wt% Li-Mo-O coated HE-NCM can be summarized into three main reasons. First, the Li^+ conductive and insulating Li-Mo-O compound coating can reduce side reactions at the cathode and electrolyte interface. By comparing the long-term cycle results from the 3 wt% Li-Mo-O coated HE-NCM heat treated at 600 ^oC and the water washed coated HE-NCM, the coated and Mo^{6+} surface diffused HE-NCM (3 wt% Li-Mo-O coated HE-NCM) shows higher degree of cycle stability compared to the samples with the Mo^{6+} surface diffused alone (water washed coated HE-NCM). The impedance studies with bare HE-NCM and the 3 wt% Li-Mo-O coated HE-NCM before and after cycling also show the evidence of the reduced side reaction on the coated HE-NCM surface by showing significantly less impedance growth over a continuous battery cycling. The second reason for the enhanced battery cycle performance is due to the presence of a spinel phase for the 3 wt% Li-Mo-O coated HE-NCM. LNMO and possibly Mo^{6+} contained LNMO was formed after coating and 600 ^oC heat treatment in air. Since LNMO has a 3-dimensional lithium ion diffusion pathway, having LNMO may lead to more facile lithium ion diffusion during battery cycling and this can lead to an improved high C-rate capability. The cycle data show higher 3C-rate discharge capacity for the 3 wt% Li-Mo-O coated HE-NCM compared to bare HE-NCM. Although water washed coated HE-NCM also has LNMO and possibly Mo^{6+} contained LNMO, the water washing may have deformed the surface from its original layered

structure to rocksalt structure which can give adverse effects towards rate capability. The third reason for the improved electrochemical performance from the Li-Mo-O coating on HE-NCM is due to the enhanced structural stability from Mo^{6+} surface diffusion into HE-NCM upon 600 ^{o}C calcination. The bond dissociation energy between Mo and O is 502 kJ mol^{-1} which is about 34% higher than the average bond dissociation energy value from Ni, Co, Mn and O. The differential capacity plot from the 3 wt% Li-Mo-O coated HE-NCM displays higher anion redox peak retention and this can be an indication of the result from the reduced lattice oxygen loss providing sustainable anion redox capability.

References

1. J.-M. Tarascon and M. Armand, *Nature*, 2001, **414**, 359-367.
2. B. L. Ellis, K. T. Lee and L. F. Nazar, *Chem. Mater.*, 2010, **22**, 691-714.
3. V. Etacheri, R. Marom, R. Elazari, G. Salitra and D. Aurbach, *Energy Environ. Sci.*, 2011, **4**, 3243.
4. L. de Biasi, B. Schwarz, T. Brezesinski, P. Hartmann, J. Janek and H. Ehrenberg, *Adv. Mater*, 2019, **31**, e1900985.
5. J.-K. Park, *Principles and Applications of Lithium Secondary Batteries*, Wiley, 2012.
6. J. B. Goodenough and Y. Kim, *Chem. Mater.*, 2010, **22**, 587-603.
7. K. Mizushima, P. J. Wiseman, J. B. Goodenough, *Mater. Res. Bull.*, 1980, **25**, 783-789.
8. L. Alexander ,C. Kozen, A. J. Pearse, M. A. Schroeder, X. Han, L. Hu, S.-B. Lee, G. W. Rubloff, M. Noked, *ACS Nano*, 2015, **9**, 5884 - 5892.
9. P. Bai, J. Li, F. R. Brushett and M. Z. Bazant, *Energy Environ. Sci.*, 2016, **9**, 3221-3229.
10. J. Wang, J. Purewal, P. Liu, J. Hicks-Garner, S. Soukazian, E. Sherman, A. Sorenson, L. Vu, H. Tataria and M. W. Verbrugge, *J.Power Sources*, 2014, **269**, 937-948.
11. J. B. Goodenough and K. S. Park, *J. Am. Chem. Soc.*, 2013, **135**, 1167-1176.
12. Z. Lu, J. R. Dahn, *Electrochem. Solid-State Lett.* , 2001, **4**, A200-A203.
13. J. Li, L. Ma, W. Qiu, J. R. Dahn, *J. Electrochem. Soc.*, 2015, **162**, A1401-A1408.
14. J.-H. Park, B. Choi, Y.-S. Kang, S. Y. Park, D. J. Yun, I. Park, J. H. Shim, J.-H. Park, H. N. Han and K. Park, *Energy Technol.*, 2018, **6**, 1361-1369.
15. T. Sasaki, H.i Oka, C. Okuda, Y. Itou, Y. Kondo, Y. Takeuchi, Y. Ukyo, K. Tatsumi and S. Muto, *J. Electrochem. Soc.*, 2009, **156**, A289-A293.
16. H. S. Liu, Z. L. Gong, and Y. Yang, *Electrochem. Solid-State Lett.*, 2004, **7**, A190-A193.
17. S. Freiberg, M. K. Roos, J. Wandt, R. de Vivie-Riedle and H. A. Gasteiger, *J. Phys. Chem. A*, 2018, **122**, 8828-8839.
18. J. Li, R. Shunmugasundaram, R. Doig and J. R. Dahn, *Chem. Mater.*, 2015, **28**, 162-171.
19. R. Robert and P. Novák, *Chem. Mater.*, 2018, **30**, 1907-1911.
20. F. Schipper, P. Nayak, E. Erickson, S. Amalraj, O. Srur-Lavi, T. Penki, M. Talianker, J. Grinblat, H. Sclar, O. Breuer, C. Julien, N. Munichandraiah, D. Kovacheva, M. Dixit,

D. Major, B. Markovsky and D. Aurbach, *Inorganics*, 2017, **5**, 32.

21. R. Petibon, L. Madec, D. W. Abarbanel and J. R. Dahn, *J. Power Sources*, 2015, **300**, 419-429.
22. D. Ren, Y. Shen, Y. Yang, L. Shen, B. D. A. Levin, Y. Yu, D. A. Muller and H. D. Abruna, *ACS Appl Mater Interfaces*, 2017, **9**, 35811-35819.
23. H. Liu, Y. Chen, S. Hy, K. An, S. Venkatachalam, D. Qian, M. Zhang and Y. S. Meng, *Adv. Energy Mater.*, 2016, **6**, 1502143.
24. M. C. M. Moshkovich, H.E. Gottlieb, D. Aurbach, *J. Electroanal. Chem.*, 2001, **497**, 84-96.
25. R. Jung, M. Metzger, F. Maglia, C. Stinner and H. A. Gasteiger, *J. Phys. Chem. Lett.*, 2017, **8**, 4820-4825.
26. Y. S. Jung, A. S. Cavanagh, L. A. Riley, S. H. Kang, A. C. Dillon, M. D. Groner, S. M. George and S. H. Lee, *Adv. Mater.*, 2010, **22**, 2172-2176.
27. J. Kim, K. S. Ryu, M. G. Kim, J. Cho, *Electrochem. Solid-State Lett.*, 2006, **9**, A19-A23.
28. X. Xiong, Z. Wang, P. Yue, H. Guo, F. Wu, J. Wang and X. Li, *J. Power Sources*, 2013, **222**, 318-325.
29. J. Kim, H. Lee, H. Cha, M. Yoon, M. Park and J. Cho, *Adv. Energy Mater.*, 2018, **8**, 1702028.
30. Y. S. Jung, P. Lu, A. S. Cavanagh, C. Ban, G.-H. Kim, S.-H. Lee, S. M. George, S. J. Harris and A. C. Dillon, *Adv. Energy Mater.*, 2013, **3**, 213-219.
31. A. O. Kondrakov, A. Schmidt, J. Xu, H. Geßwein, R. Mönig, P. Hartmann, H. Sommer, T. Brezesinski and J. Janek, *J. Phys. Chem. C*, 2017, **121**, 3286-3294.
32. J. M. Lim, T. Hwang, D. Kim, M. S. Park, K. Cho and M. Cho, *Sci. Rep.*, 2017, **7**, 39669.
33. B. Qiu, M. Zhang, Y. Xia, Z. Liu and Y. S. Meng, *Chem. Mater.*, 2017, **29**, 908-915.
34. M. M. Thackeray, S.-H. Kang, C. S. Johnson, J. T. Vaughey, R. Benedek and S. A. Hackney, *J. Mater. Chem. A*, 2007, **17**, 3112.
35. J. R. Croy, S. H. Kang, M. Balasubramanian and M. M. Thackeray, *Electrochem. Commun.*, 2011, **13**, 1063-1066.
36. H. Yu, Y. G. So, Y. Ren, T. Wu, G. Guo, R. Xiao, J. Lu, H. Li, Y. Yang, H. Zhou, R.

Wang, K. Amine and Y. Ikuhara, *J. Am. Chem. Soc.*, 2018, **140**, 15279-15289.

37. G. Assat, D. Foix, C. Delacourt, A. Iadecola, R. Dedryvere and J. M. Tarascon, *Nat. Commun.*, 2017, **8**, 2219.
38. G. Assat, C. Delacourt, D. A. D. Corte and J.-M. Tarascon, *J. Electrochem. Soc.*, 2016, **163**, A2965-A2976.
39. D. Foix, M. Sathiya, E. McCalla, J.-M. Tarascon and D. Gonbeau, *J. Phys. Chem. C*, 2016, **120**, 862-874.
40. S. Saha, G. Assat, M. T. Sougrati, D. Foix, H. Li, J. Vergnet, S. Turi, Y. Ha, W. Yang, J. Cabana, G. Rousse, A. M. Abakumov and J.-M. Tarascon, *Nat. Energy*, 2019, **4**, 977-987.
41. G. Assat, A. Iadecola, D. Foix, R. Dedryvère and J.-M. Tarascon, *ACS Energy Letters*, 2018, **3**, 2721-2728.
42. M. Sathiya, G. Rousse, K. Ramesha, C. P. Laisa, H. Vezin, M. T. Sougrati, M. L. Doublet, D. Foix, D. Gonbeau, W. Walker, A. S. Prakash, M. Ben Hassine, L. Dupont and J. M. Tarascon, *Nat. Mater.*, 2013, **12**, 827-835.
43. G. Assat and J.-M. Tarascon, *Nat. Energy*, 2018, **3**, 373-386.
44. V. Pimenta, M. Sathiya, D. Batuk, A. M. Abakumov, D. Giaume, S. Cassaignon, D. Larcher and J.-M. Tarascon, *Chem. Mater.*, 2017, **29**, 9923-9936.
45. M. Saubanère, E. McCalla, J. M. Tarascon and M. L. Doublet, *Energy Environ. Sci.*, 2016, **9**, 984-991.
46. E. Salager, V. Sarou-Kanian, M. Sathiya, M. Tang, J.-B. Leriche, P. Melin, Z. Wang, H. Vezin, C. Bessada, M. Deschamps and J.-M. Tarascon, *Chem. Mater.*, 2014, **26**, 7009-7019.
47. Q. Jacquet, A. Iadecola, M. Saubanere, H. Li, E. J. Berg, G. Rousse, J. Cabana, M. L. Doublet and J. M. Tarascon, *J. Am. Chem. Soc.*, 2019, **141**, 11452-11464.
48. M. Ben Yahia, J. Vergnet, M. Saubanere and M. L. Doublet, *Nat. Mater.*, 2019, **18**, 496-502.
49. N. Guerrini, L. Jin, J. G. Lozano, K. Luo, A. Sobkowiak, K. Tsuruta, F. Massel, L.-C. Duda, M. R. Roberts and P. G. Bruce, *Chem. Mater.*, 2020, **32**, 3733-3740.
50. R. A. House, U. Maitra, M. A. Perez-Osorio, J. G. Lozano, L. Jin, J. W. Somerville, L. C. Duda, A. Nag, A. Walters, K. J. Zhou, M. R. Roberts and P. G. Bruce, *Nature*, 2020,

577, 502-508.

51. A. J. Naylor, E. Makkos, J. Maibach, N. Guerrini, A. Sobkowiak, E. Björklund, J. G. Lozano, A. S. Menon, R. Younesi, M. R. Roberts, K. Edström, M. S. Islam and P. G. Bruce, *J. Mater. Chem. A*, 2019, **7**, 25355-25368.
52. R. A. House, U. Maitra, L. Jin, J. G. Lozano, J. W. Somerville, N. H. Rees, A. J. Naylor, L. C. Duda, F. Massel, A. V. Chadwick, S. Ramos, D. M. Pickup, D. E. McNally, X. Lu, T. Schmitt, M. R. Roberts and P. G. Bruce, *Chem. Mater.*, 2019, **31**, 3293-3300.
53. K. Luo, M. R. Roberts, N. Guerrini, N. Tapia-Ruiz, R. Hao, F. Massel, D. M. Pickup, S. Ramos, Y. S. Liu, J. Guo, A. V. Chadwick, L. C. Duda and P. G. Bruce, *J. Am. Chem. Soc.*, 2016, **138**, 11211-11218.
54. U. Maitra, R. A. House, J. W. Somerville, N. Tapia-Ruiz, J. G. Lozano, N. Guerrini, R. Hao, K. Luo, L. Jin, M. A. Perez-Osorio, F. Massel, D. M. Pickup, S. Ramos, X. Lu, D. E. McNally, A. V. Chadwick, F. Giustino, T. Schmitt, L. C. Duda, M. R. Roberts and P. G. Bruce, *Nat. Chem.*, 2018, **10**, 288-295.
55. J. Wandt, A. T. S. Freiberg, A. Ogrodnik and H. A. Gasteiger, *Mater. Today*, 2018, **21**, 825-833.
56. N. Mahne, S. E. Renfrew, B. D. McCloskey and S. A. Freunberger, *Angew. Chem. Int. Ed. Engl.*, 2018, **57**, 5529-5533.
57. S. E. Renfrew and B. D. McCloskey, *J. Am. Chem. Soc.*, 2017, **139**, 17853-17860.
58. S. Chen, T. He, Y. Su, Y. Lu, L. Bao, L. Chen, Q. Zhang, J. Wang, R. Chen and F. Wu, *ACS Appl. Mater. Interfaces*, 2017, **9**, 29732-29743.
59. K. Kleiner, B. Strehle, A. R. Baker, S. J. Day, C. C. Tang, I. Buchberger, F.-F. Chesneau, H. A. Gasteiger and M. Piana, *Chem. Mater.*, 2018, **30**, 3656-3667.
60. B. Strehle, Kleiner, Karin, Jung, Roland, Chesneau, Frederick, Mendez, Manuel, Gasteiger, Hubert A., Piana, Michele, *J. Electrochem. Soc.*, 2017, **164**, A400-A406.
61. M. M. Roland Jung, Filippo Maglia, Christoph Stinner, Hubert A. Gasteiger, *J. Electrochem. Soc.*, 2017, **164**, A1361-A1377.
62. A. R. West, *Solid State Chemistry and its Applications*, John Wiley & Sons, West Sussex, United Kingdom, 2014.
63. S. Schlueter, R. Genieser, D. Richards, H. E. Hoster and M. P. Mercer, *Phys. Chem. Chem. Phys.*, 2018, **20**, 21417-21429.

64. K. N. Wood and G. Teeter, *ACS Appl. Energy Mater.*, 2018, **1**, 4493-4504.
65. G. L. Miessler, *Inorganic chemistry*, Pearson, Upper Saddle River, New Jersey, USA, 2014.
66. H. Nara, D. Mukoyama, R. Shimizu, T. Momma and T. Osaka, *J. Power Sources*, 2019, **409**, 139-147.
67. M. A. Philip, P. T. Sullivan, R. Zhang, G. A. Wooley, S. A. Kohn and A. A. Gewirth, *ACS Appl. Mater. Interfaces*, 2019, **11**, 2014-2021.
68. A. Barai, K. Uddin, W. D. Widanage, A. McGordon and P. Jennings, *Sci. Rep.*, 2018, **8**, 21.
69. J. Gordon, S. Grugeon, H. Takenouti, B. Tribollet, M. Armand, C. Davoisne, A. Débart and S. Laruelle, *Electrochim. Acta*, 2017, **223**, 63-73.
70. M. Steinhauer, S. Risse, N. Wagner and K. A. Friedrich, *Electrochim. Acta*, 2017, **228**, 652-658.
71. P. Kumar Nayak, J. Grinblat, E. Levi, T. R. Penki, M. Levi, Y. K. Sun, B. Markovsky and D. Aurbach, *ACS Appl. Mater. Interfaces*, 2017, **9**, 4309-4319.
72. P. Oh, S. M. Oh, W. Li, S. Myeong, J. Cho and A. Manthiram, *Adv. Sci.*, 2016, **3**, 1600184.
73. J. Yang and Y. Xia, *ACS Appl. Mater. Interfaces*, 2016, **8**, 1297-1308.
74. M. D. Levi, V. Dargel, Y. Shilina, D. Aurbach and I. C. Halalay, *Electrochim. Acta*, 2014, **149**, 126-135.
75. D. Andre, M. Meiler, K. Steiner, C. Wimmer, T. Soczka-Guth and D. U. Sauer, *J. Power Sources*, 2011, **196**, 5334-5341.
76. H. G. Schweiger, O. Obeidi, O. Komesker, A. Raschke, M. Schiemann, C. Zehner, M. Gehnen, M. Keller and P. Birke, *Sensors*, 2010, **10**, 5604-5625.
77. D. P. Abraham, J. R. Heaton, S. H. Kang, D. W. Dees and A. N. Jansen, *J. Electrochem. Soc.*, 2008, **155**, A41.
78. K. Kleiner, B. Strehle, A. R. Baker, S. J. Day, C. C. Tang, I. Buchberger, F.-F. Chesneau, H. A. Gasteiger and M. Piana, *Chem. Mater.*, 2018, **30**, 3656-3667.
79. F. Meng, H. Guo, Z. Wang, J. Wang, G. Yan, X. Wu, X. Li and L. Zhou, *Appl. Surf. Sci.*, 2019, **479**, 1277-1286.
80. L. Zou, J. Li, Z. Liu, G. Wang, A. Manthiram and C. Wang, *Nat. Commun.*, 2019, **10**,

3447.

81. D. S. Hall, R. Gauthier, A. Eldesoky, V. S. Murray and J. R. Dahn, *ACS Appl. Mater. Interfaces*, 2019, **11**, 14095-14100.
82. D. Liu, F. Wang, G. Wang, C. Lv, Z. Wang, X. Duan and X. Li, *Molecules*, 2019, **24**.
83. K. Park, J. Kim, J.-H. Park, Y. Hwang and D. Han, *J. Power Sources*, 2018, **408**, 105-110.
84. N. Dannehl, S. O. Steinmuller, D. V. Szabo, M. Pein, F. Sigel, L. Esmezjan, U. Hasenkox, B. Schwarz, S. Indris and H. Ehrenberg, *ACS Appl. Mater. Interfaces*, 2018, **10**, 43131-43143
85. W. Liu, X. Li, D. Xiong, Y. Hao, J. Li, H. Kou, B. Yan, D. Li, S. Lu, A. Koo, K. Adair and X. Sun, *Nano Energy*, 2018, **44**, 111-120.
86. X. Zhang, R. Yu, Y. Huang, X. Wang, Y. Wang, B. Wu, Z. Liu and J. Chen, *ACS Sustain. Chem. Eng.*, 2018, **6**, 12969-12979.
87. Z. Du, W. Peng, Z. Wang, H. Guo, Q. Hu and X. Li, *Ionics*, 2018, **24**, 3717-3724.
88. B. Xiao and X. Sun, *Adv. Energy Mater.*, 2018, **8**, 1802057.
89. X. D. Zhang, J. L. Shi, J. Y. Liang, Y. X. Yin, J. N. Zhang, X. Q. Yu and Y. G. Guo, *Adv. Mater.*, 2018.
90. C. Wang, F. Zhou, K. Chen, J. Kong, Y. Jiang, G. Yan, J. Li, C. Yu and W.-P. Tang, *Electrochim. Acta*, 2015, **176**, 1171-1181.
91. X. Feng, Z. Yang, D. Tang, Q. Kong, L. Gu, Z. Wang and L. Chen, *Phys. Chem. Chem. Phys.*, 2015, **17**, 1257-1264.
92. S. Sun, N. Wan, Q. Wu, X. Zhang, D. Pan, Y. Bai and X. Lu, *Solid State Ionics*, 2015, **278**, 85-90.
93. J.-Z. Kong, C.-L. Wang, X. Qian, G.-A. Tai, A.-D. Li, D. Wu, H. Li, F. Zhou, C. Yu, Y. Sun, D. Jia and W.-P. Tang, *Electrochim. Acta*, 2015, **174**, 542-550.
94. R. Yu, Y. Lin and Z. Huang, *Electrochim. Acta*, 2015, **173**, 515-522.
95. S. Guo, H. Yu, P. Liu, X. Liu, D. Li, M. Chen, M. Ishida and H. Zhou, *J. Mater. Chem. A*, 2014, **2**, 4422.
96. W. Yuan, H. Z. Zhang, Q. Liu, G. R. Li and X. P. Gao, *Electrochim. Acta*, 2014, **135**, 199-207.
97. I. T. Kim, J. C. Knight, H. Celio and A. Manthiram, *J. Mater. Chem. A*, 2014, **2**, 8696.

98. X. Xiong, Z. Wang, X. Yin, H. Guo and X. Li, *Mater. Letters*, 2013, **110**, 4-9.
99. Y. Wu, J. Ming, L. Zhuo, Y. Yu and F. Zhao, *Electrochim. Acta*, 2013, **113**, 54-62.
100. C. Li, H. P. Zhang, L. J. Fu, H. Liu, Y. P. Wu, E. Rahm, R. Holze and H. Q. Wu, *Electrochim. Acta*, 2006, **51**, 3872-3883.
101. J. Zhang, Q. Lu, J. Fang, J. Wang, J. Yang and Y. NuLi, *ACS Appl. Mater. Interfaces*, 2014, **6**, 17965-17973.
102. C. Wang, F. Zhou, K. Chen, J. Kong and W. P. Tang, *Electrochim. Acta*, 2015, **176**, 1171-1181.
103. F. Wu, J. Tian, Y. Su, Y. Guan, Y. Jin, Z. Wang, T. He, L. Bao and S. Chen, *J. Power Sources*, 2014, **269**, 747-754.
104. S. Tao, H. Zhao, C. Wu, H. Xie, P. Cui, T. Xiang, S. Chen, L. Zhang, Y. Fang, Z. Wang, W. Chu, B. Qian and L. Song, *Mater. Chem. Phys.*, 2017, **199**, 203-208.
105. Y. Gao, P. Xu, F. Chen, C. Ding, L. Chen and D. Li, *RSC Adv.* 2016, **6**, 113275-113282
106. D. Becker, M. Börner, R. Nölle, M. Diehl, S. Klein, U. Rodehorst, R. Schmuch, M. Winter, and T. Placke, *ACS Appl. Mater. Interfaces,* 2019, **11**, 18404–18414
107. B. Luo, B. Jiang, P. Peng, J. Huang, J. Chen, M. Li, L. Chu and Y. Li, *Electrochim. Acta*, 2019, **297**, 398-405.
108. X. Yang, Z. Zuo, H. Wang, Q. Chen, H. Zhang, Z. Huang, B. Wu and H. Zhou, *Electrochim. Acta*, 2015, **180**, 604-609.
109. Y. He, Y. Li, Y. Liu, N. Yao, J. Li and Y. Liu, *Appl. Surf. Sci.*, 2020, **508**, 145259
110. B. Song, W. Li, S. -M. Oh, and A. Manthiram, *ACS Appl. Mater. Interfaces,* 2017, **9**, 9718-9725
111. Z. Chen and J. R. Dahn, *Electrochem. Solid-State Lett.*, 2002, **5**, A213-A216
112. K. Yamamoto, Y. Orikasa, D. Takamatsu, Y. Koyama, S. Mori, T. Masese, T. Mori, T. Minato, H. Tanida, T. Uruga, Z. Ogumi and Y. Uchimoto, *Electrochemistry*, 2014, **82(10)**, 891-896
113. J. Xie, A. D. Sendek, E. D. Cubuk, X. Zhang, Z. Lu, Y. Gong, T. Wu, F. Shi, W. Liu, E. J. Reed and Y. Cui, *ACS Nano*, 2017, **11**, 7019-7027
114. F. Xin , H. Zhou, X. Chen, M. Zuba, N. Chernova, G. Zhou and M. S. Whittingham, *ACS Appl. Mater. Interfaces,* 2019, **11**, 34889-34894
115. J. S. Park, X. Meng, J. W. Elam, S. Hao, C. Wolverton, C. Kim and J. Cabana, *Chem.*

Mater., 2014, **26**, 3128-3134

116. L. Chen, K. S. Chen, X. Chen, G. Ramirez, Z. Huang, N. R. Geise, H. G. Steinruck, B. L. Fisher, R. Shahbazian-Yassar, M. F. Toney, M. C. Hersam and J. W. Elam, *ACS Appl. Mater. Interfaces*, 2018, **10**, 26972-26981.
117. E. Kazyak, K.-H. Chen, A. L. Davis, S. Yu, A. J. Sanchez, J. Lasso, A. R. Bielinski, T. Thompson, J. Sakamoto, D. J. Siegel and N. P. Dasgupta, *J. Mater. Chem. A*, 2018, **6**, 19425-19437.
118. Z. Wei, Z. Hai, M. K. Akbari, D. Qi, K. Xing, Q. Zhao, F. Verpoort, J. Hu, L. Hyde and S. Zhuiykov, *Sens. Actuators B Chem.*, 2018, **262**, 334-344.
119. W. Lu, L. Liang, X. Sun, X. Sun, C. Wu, L. Hou, J. Sun and C. Yuan, *Nanomaterials*, 2017, **7**.
120. M. R. Laskar, D. H. Jackson, S. Xu, R. J. Hamers, D. Morgan and T. F. Kuech, *ACS Appl. Mater. Interfaces*, 2017, **9**, 11231-11239.
121. D. Muñoz-Rojas, V. H. Nguyen, C. Masse de la Huerta, S. Aghazadehchors, C. Jiménez and D. Bellet, *C. R. Phys.*, 2017, **18**, 391-400.
122. A. M. Wise, C. Ban, J. N. Weker, S. Misra, A. S. Cavanagh, Z. Wu, Z. Li, M. S. Whittingham, K. Xu, S. M. George and M. F. Toney, *Chem. Mater.*, 2015, **27**, 6146-6154.
123. N. A. Chernova, M. Roppolo, A. C. Dillon and M. S. Whittingham, *J. Mater. Chem. A*, 2009, **19**, 2526.
124. A. M. Hashem, M. H. Askar, M. Winter, J. H. Albering and J. O. Besenhard, *Ionics*, 2007, **13**, 3-8.
125. A. M. Christian Julien, Ashok Vijh, Karim Zaghib, *Lithium Batteries*, Switzerland, 2016.
126. S.-H. Lee, Y.-H. Kim, R. Deshpande, P. A. Parilla, E. Whitney, D. T. Gillaspie, K. M. Jones, A. H. Mahan, S. Zhang and A. C. Dillon, *Adv. Mater.*, 2008, **20**, 3627-3632.
127. X. Lu, R. Wang, F. Yang, W. Jiao, W. Liu, L. Hao and X. He, *J. Mater. Chem. A*, 2016, **4**, 6720-6726.
128. S. M. Paek, J. H. Kang, H. Jung, S. J. Hwang and J. H. Choy, *Chem. Commun.*, 2009.
129. H. A. T. Mohammed Ibrahim Shukoor, Lela Gorgishvili, Gunnar Glasser, Ute Kolb, Wolfgang Tremel, *Chem. Mater.*, 2006, **18**, 2144-2151.

130. A. Chithambararaj, N. Rajeswari Yogamalar and A. C. Bose, *Cryst. Growth Des.*, 2016, **16**, 1984-1995.
131. T. H. Chiang and H. C. Yeh, *Materials*, 2013, **6**, 4609-4625.
132. S. Tao, H. Zhao, C. Wu, H. Xie, P. Cui, T. Xiang, S. Chen, L. Zhang, Y. Fang, Z. Wang, W. Chu, B. Qian and L. Song, *Mater. Chem. Phys.*, 2017, **199**, 203-208.
133. Y. Li, D. Wang, Q. An, B. Ren, Y. Rong and Y. Yao, *J. Mater. Chem. A*, 2016, **4**, 5402-5405.
134. R. Nadimicherla, W. Chen and X. Guo, *Mater. Res. Bull.*, 2015, **66**, 140-146.
135. P. Wongkrua, T. Thongtem and S. Thongtem, *J. Nanomaterials*, 2013, **2013**, 1-8.
136. Z. Wang, S. M. Richter, B. D. Gates and T. A. Grieme, *Org. Process Res. Dev.*, 2012, **16**, 1994-2000.
137. R. Shunmugasundaram, R. Senthil Arumugam and J. R. Dahn, *Chem. Mater.*, 2015, **27**, 757-767.
138. A. R. C. Jing Li, Hongyang Li, Stephen Glazier,a Deijun Xiong, M. Chatzidakis, Jenn Allen, G. A. Botton, J. R. Dahn, *Journal ofThe Electrochemical Society*, 2017, **164**, A1534-A1544.
139. L. J. K. Andrew van Bommel, J. R. Dahn, *J. Electrochem. Soc.*, 2011, **158**, A731-A735.
140. R. Robert, C. Bünzli, E. J. Berg and P. Novák, *Chem. Mater.*, 2015, **27**, 526-536.
141. R. Shunmugasundaram, R. Senthil Arumugam, K. J. Harris, G. R. Goward and J. R. Dahn, *Chem. Mater.*, 2015, **28**, 55-66.
142. J. Xu, M. Sun, R. Qiao, S. E. Renfrew, L. Ma, T. Wu, S. Hwang, D. Nordlund, D. Su, K. Amine, J. Lu, B. D. McCloskey, W. Yang and W. Tong, *Nat. Commun.*, 2018, **9**, 947.
143. G. Liu, M. Ouyang, L. Lu, J. Li and X. Han, *J. Power Sources*, 2015, **274**, 971-989.
144. I. Bloom, A. N. Jansen, D. P. Abraham, J. Knuth, S. A. Jones, V. S. Battaglia and G. L. Henriksen, *J. Power Sources*, 2005, **139**, 295-303.
145. S. Shen, Y. Hong, F. Zhu, Z. Cao, Y. Li, F. Ke, J. Fan, L. Zhou, L. Wu, P. Dai, M. Cai, L. Huang, Z. Zhou, J. Li, Q. Wu and S. Sun, *ACS Appl. Mater. Interfaces*, 2018, **10**, 12666-12677.
146. F. Sigel, B. Schwarz, K. Kleiner, C. Dräger, L. Esmezjan, M. Yavuz, S. Indris and H. Ehrenberg, *Chem. Mater.*, 2020, **32**, 1210-1223.
147. A. M. S. Choi, *J. Electrochem. Soc.*, 2002, **149**, A1157-A1163.

148. E. M. Erickson, H. Sclar, F. Schipper, J. Liu, R. Tian, C. Ghanty, L. Burstein, N. Leifer, J. Grinblat, M. Talianker, J.-Y. Shin, J. K. Lampert, B. Markovsky, A. I. Frenkel and D. Aurbach, *Adv. Energy Mater.*, 2017, **7**, 1700708.
149. Z. Zhu, D. Yu, Y. Yang, C. Su, Y. Huang, Y. Dong, I. Waluyo, B. Wang, A. Hunt, X. Yao, J. Lee, W. Xue and J. Li, *Nat. Energy*, 2019, **4**, 1049-1058.
150. R. Cheruku, D. S. Bhaskaram, G. Govindaraj and L. Vijayan, *J. Alloys Compds*., 2019, **788**, 779-786.
151. J. Zhang, R. Li, Q. Chen, G. Zhao and J. Jia, *Mater. Letters*, 2018, **233**, 302-305.
152. H. W. Kwak and Y. J. Park, *Thin Solid Films*, 2018, **660**, 625-630.
153. J. Liu, Y. Lin, T. Lu, C. Du, W. Wang, S. Wang, Z. Tang, D. Qu and X. Zhang, *Electrochim. Acta*, 2015, **170**, 202-209.
154. D. Mikhailova, A. Voss, S. Oswald, A. A. Tsirlin, M. Schmidt, A. Senyshyn, J. Eckert and H. Ehrenberg, *Chem. Mater.*, 2015, **27**, 4485-4492.
155. P. Villars and K. Cenzual, Li_2MoO_4 ($Li_2[MoO_4]$ hp) Crystal Structure: Datasheet from "Pauling File Multinaries Edition – 2012" in SpringerMaterials (https://materials. springer.com/isp/crystallographic/docs/sd_1214006).
156. Y. Kawahara, T. Ichihara, N. Kijima, M. Kakihana, *Chem. Mater.*, 2006, **18**, 6303-6307.
157. Q. Li, D. Ning, D. Zhou, K. An, D. Wong, L. Zhang, Z. Chen, G. Schuck, C. Schulz, Z. Xu, G. Schumacher and X. Liu, *J. Mater. Chem. A*, 2020, **8**, 7733-7745.
158. P. K. Nayak, J. Grinblat, M. Levi, E. Levi, S. Kim, J. W. Choi and D. Aurbach, *Adv. Energy Mater.*, 2016, **6**, 1502398.
159. S. Kim, W. Cho, X. Zhang, Y. Oshima and J. W. Choi, *Nat. Commun.*, 2016, **7**, 13598.
160. N.-S. Choi, J.-G. Han, S.-Y. Ha, I. Park and C.-K. Back, *RSC Adv.*, 2015, **5**, 2732-2748.
161. M. Barsoum, *Fundamentals of Ceramics*, CRC Press, 2002.
162. Y. R. Luo, *Handbook of Bond Dissociation Energies in Organic Compounds*, 2002, 9-66
163. N. Amdouni, K. Zaghib, F. Gendron, A. Mauger and C. M. Julien, *Ionics*, 2006, **12**, 117-126.
164. J. Lee, N. Dupre, M. Avdeev and B. Kang, *Sci. Rep.*, 2017, **7**, 6728.
165. N. Leifer, F. Schipper, E. M. Erickson, C. Ghanty, M. Talianker, J. Grinblat, C. M. Julien, B. Markovsky and D. Aurbach, *J. Phys. Chem. C*, 2017, **121**, 9120-9130.

166. R. Thirunakaran, R. Ravikumar, S. Vijayarani, S. Gopukumar and A. Sivashanmugam, *Energy Convers.Manag.*, 2012, **53**, 276-281.
167. Q. Xia, X. Zhao, M. Xu, Z. Ding, J. Liu, L. Chen, D. G. Ivey and W. Wei, *J. Mater. Chem. A*, 2015, **3**, 3995-4003.
168. L. Zhou, Z. Yin, H. Tian, Z. Ding, X. Li, Z. Wang and H. Guo, *Appl. Surf. Sci.*, 2018, **456**, 763-770.
169. R. E. Ruther, A. F. Callender, H. Zhou, S. K. Martha and J. Nanda, *J. Electrochem. Soc.*, 2014, **162**, A98-A102.
170. B. Mihailova, *Raman and IR spectroscopy in materials science. Symmetry analysis of normal phonon modes*, Institute of Mineralogy and Petrology, University of Hamburg, Lekeitio, Spain, 2009.
171. C. V. Ramana, M. Massot and C. M. Julien, *Surf. Interface Anal.*, 2005, **37**, 412-416.
172. Y. Cho, P. Oh, and J. Cho, *Nano lett.* 2013, **13**, 1145-1152
173. M. M. Alsabban, X. Yang, W. Wahyudi, J.-H. Fu, M. N. Hedhili, J. Ming, C.-W. Yang, M. A. Nadeem, H. Idriss, Z. Lai, L.-J. Li, V. Tung and K.-W. Huang, *ACS Appl. Mater. Interfaces*, 2019, **11**, 20752-20761.
174. S. Cottea, B. Pecquenarda, F. L. Cras, R. Grissad, H. Martinezd and L. Bourgeoise, *Electrochim. Acta*, 2015, **180**, 528-534.
175. Z. Ruan, Y. Zhu and X. Teng, *J. Mater. Sci.*, 2016, **51**,1400–1408.
176. L. Dahéron, R. Dedryvère, H. Martinez, M. Ménétrier, C. Denage, C. Delmas and D. Gonbeau, *Chem. Mater.* 2008, **20**, 583–590
177. G. Liang, V. K. Peterson, K. W. See, Z. Guo and W. K. Pang, *J. Mater. Chem. A*, 2020, Advance Article
178. K. Shimoda, M. Oishi, T. Matsunaga, M. Murakami, K. Yamanaka, H. Arai, Y. Ukyo, Y. Uchimoto, T. Ohta, E. Matsubara and Z. Ogumi, *J. Mater. Chem. A*, 2017, **5**, 6695-6707.
179. M. Oishi, K. Yamanaka, I. Watanabe, K. Shimoda, T. Matsunaga, H. Arai, Y. Ukyo, Y. Uchimoto, Z. Ogumi and T. Ohta, *J. Mater. Chem. A*, 2016, **4**, 9293-9302.
180. P. Yan, J. Zheng, Z. K. Tang, A. Devaraj, G. Chen, K. Amine, J. G. Zhang, L. M. Liu and C. Wang, *Nat. Nanotechnol.*, 2019, **14**, 602-608.
181. D. P. Tobias Teufl, Sophie Solchenbach, Hubert A. Gasteiger, Manuel A. Mendez, *J.*

Electrochem. Soc., 2019, **166**, A1275-A1284.

182. D.-H. Cho, W. Cho, Y.-J. Kim, H. Yashiro, Y.-K. Sun, S.-T. Myung, *J. Electrochem. Soc.*, 2014, **161**, A920-A926.
183. F. Xin, H. Zhou, X. Chen, M. Zuba, N. Chernova, G. Zhou and M. S. Whittingham, *ACS Appl. Mater. Interfaces*, 2019, **11**, 34889-34894.
184. W. Tang, Z. Chen, F. Xiong, F. Chen, C. Huang, Q. Gao, T. Wang, Z. Yang and W. Zhang, *J. Power Sources*, 2019, **412**, 246-254.
185. F. Schipper, H. Bouzaglo, M. Dixit, E. M. Erickson, T. Weigel, M. Talianker, J. Grinblat, L. Burstein, M. Schmidt, J. Lampert, C. Erk, B. Markovsky, D. T. Major and D. Aurbach, *Adv. Energy Mater.*, 2018, **8**, 1701682.
186. E. Flores, P. Novák and E. J. Berg, *Front. Energy Res.*, 2018, **6**.
187. C. Villevieille, P. Lanz, C. Bünzli and P. Novák, *J. Mater. Chem. A*, 2014, **2**, 6488.
188. P. Lanz, C. Villevieille and P. Novák, *Electrochim. Acta*, 2014, **130**, 206-212.
189. J. Zheng, S. Myeong, W. Cho, P. Yan, J. Xiao, C. Wang, J. Cho and J.-G. Zhang, *Adv. Energy Mater.*, 2017, **7**, 1601284.